The High-Z All-Sky Spectrum Experiment

by

Olga Navros

Submitted in partial fulfillment of the
requirements for the degree of
Doctor of Philosophy
at
Carnegie Mellon University
Department of Physics
Pittsburgh, Pennsylvania

Advised by Professor Jeffrey Peterson

August 24, 2021

Abstract

The Cosmic Dawn ($z \sim 30$ to $z \sim 10$) is the observationally elusive time period in the history of the universe when the first stars ignited and started filling the universe with their light, thereby changing the intergalactic medium (IGM) around them. The UV light from the first stars left an imprint on the 21-cm cosmological signal, which could be detected observationally as a dip in the global 21-cm temperature brightness spectrum. The death of the first stars also effected the 21-cm signal by heating up the gas in the IGM, leading to a rise in the 21-cm temperature brightness temperature. The exact location and shape of the cosmic signal caused by the dip and rise of the 21-cm temperature brightness during this time period is still uncertain, due to insufficient observational data. Although the EDGES team has reported a potential detection of this cosmological signal, their detection has not be confirmed. Other groups with vastly different observational systems need to measure the signal for the cosmological community to be convinced of the detection.

Our group has developed the High-Z system to measure this cosmological signal from the period of the Cosmic Dawn. The High-Z system measures the global average of the 21-cm temperature brightness spectrum but is very different from the systems used by other 21-cm observational groups. High-Z is the only system to use an unmatched network to measure the 21-cm cosmological signal. In this thesis, I describe the calibration of the High-Z system and the interesting effects that result from the purposeful impedance mismatch of our system. The large impedance mismatch in our system leads to certain effects being magnified, which might not be otherwise noticed in a matched network.

The focus of this thesis is primarily on the absolute calibration of the High-Z system, along with the development and testing of the different methods for experimentally measuring the noise contribution of the first amplifier in our electronic chain. The complete characterization of the noise properties of the first amplifier, which is the largest contributor of noise in our system, is crucial to the correct calibration of the High-Z system. In addition to calibration, I cover the deployments of the High-Z system in the field on three separate occasions and develop a data analysis pipeline for processing the data from the field.

Acknowledgments

I would like to thank my advisor, Jeffrey Peterson, for allowing me to be a part of the High-Z project, for supporting and guiding me through my research, and for being my friend during the strenuous and difficult times of our deployments. Although our deployments involved a lot of hard work and pushed us to the limits of our physical and mental boundaries, they were also an adventure and allowed me to visit remote locations I would never otherwise see.

I would like to express my deep, deep gratitude to my two children, Romie and Nina. They supported me with their love, kindness, and patience for my entire PhD, and I would not have had the strength to make it through this program without them. I would like to thank my father, Igor Mihailovich Navros, for his love and support from across the world during my graduate studies. Although he is far away, he always calls, he always encourages me, and he always makes me smile. I hope I will make him proud to be the first one in our family to receive a Doctorate Degree. One very special person that deserves a lot of thanks is my dad, James Michael Stratton. He has been there for me every step of the way and supported me in more ways than one. He deserves thanks on so many levels and I hope he knows how much I appreciate and love him. Another very special person that deserves a lot of thanks is my bonus dad, Scott Thompson. He has been an incredible support during my graduate program and his encouragement and care for me really helped me to make it through the difficult times of my PhD.

There is one person in my PhD program who really supported me fully and unconditionally in more ways than one. Shashin Pavaskar has been my best friend, my partner, the father to my adopted children, and the most significant person in my life during my graduate program. Without him, I would not have had the opportunity to go on deployments, which were so necessary to my PhD. Without him, I would not have had the strength to carry on when I faced difficulties in my graduate studies. He has been my rock and I will always be thankful to him for everything he has done for me and my children.

I would like to thank Professor Kevin Bandura for inviting me to West Virginia University to discuss methods of calibration for our High-Z system. His advice and ideas helped us to think about the calibration in a new light. I would also like to thank hi for allowing me to use his screening room for my experiments.

I would like to thank two great women in my life, Barbara Soloman and Diane Turnshek. They have motivated and inspired me more than any other person to really love and appreciate physics and astronomy. They have also been some of my biggest supporters not only in physics but in all areas of my life. They taught me how to persevere in my Ph.d. and how to become a stronger person in the face of challenges.

Last but not least I would like to thank our department chair, Scott Dodelson, for being incredibly supportive and for offering valuable advise in my graduate studies.

Contents

List of Tables

List of Figures

Chapter 1

Introduction

1.1 Introduction

In the last several decades, we have greatly improved our understanding of the evolution of the Universe. We have been able to decipher the secrets of the primordial universe, when it was only 380000 years old, as well as the large scale structures that formed a billion years later. Soon after the universe cooled down enough to form neutral hydrogen through the recombination of electrons and protons, microwave photons decoupled from it. We see this radiation today in the form of cosmic microwave background (CMB). This radiation provides us with a snapshot of the early universe, therefore allowing us to study it. With our advancing technology, we have also been able to look directly at the universe when it was a billion years old. Telescopes on the ground as well as in space have provided cosmologists with enormous amounts of data regarding the galaxies and other large scale structures. We now have a clear picture of how the tiny fluctuations in the early universe which are imprinted on the CMB, gave rise to large scale structure formation in the entire universe.

Even with our understanding of these essential periods in the history of the universe, there seems to be a lack of understanding of the timeline spanning between $z \approx 1100$ to $z \approx 6$. This era consists of the Dark Ages, the Cosmic Dawn, and the Era of Reionization (EoR). The Dark Ages ($z \approx 1100$ to $z \approx 30$) began with radiation decoupling from matter and lasted until the period when the first stars started forming. Following the Dark Ages was the era of the Cosmic Dawn ($z \approx 30$ to $z \approx 10$) when the universe was illuminated by the light from the first stars until the Intergalactic Medium (IGM) was fully ionized by this radiation around $z \approx 6$. Although a lot is known theoretically about these periods, they have been marked by lack of direct observational evidence. This constitutes the next era in observational cosmology.

The 21-cm cosmology provides a direct way to understand the Dark Ages and the era of the Cosmic Dawn. The IGM during the Dark Ages and the Cosmic Dawn consisted of up to 75 percent of neutral Hydrogen. In neutral Hydrogen, the interaction of the magnetic moments of the electron and the proton results in hyperfine splitting, which is responsible for the 21-cm photon line. Due to the expansion of the universe this line gets red-shifted to radio frequencies as it reaches us. The deviations in the brightness of the 21-cm line can provide us with clues about the history of the universe during the Dark Ages and the Cosmic Dawn.

A number of radio experiments already exist that try to observe these deviations as a global average of the 21-cm brightness temperature, including EDGES [5] [14], SARAS [19], LEDA [10], and REACH. In 2018, EDGES published a detection of an absorption trough in the global 21-cm brightness temperature that was twice the maximum amplitude predicted by theoretical models [4]. Their results raised a lot of excitement in the cosmological community and could point toward new physics during this elusive time period in our universe [[16], [17], [15], [18], [1], [2], [28], [29], [13]]. However, their detection remains unconfirmed by other experimental groups. Detection of this signal by other experimental groups, with observational systems and methodologies vastly different than EDGES, is absolutely necessary to confirm or deny their findings. Our High-Z system, which measures the evolution of the global 21-cm brightness temperature from the Dark Ages to the end of the Cosmic Dawn, differs significantly from the EDGES team in several key areas. Therefore, our High-Z system can potentially confirm or deny the observations of the EDGES team, which would be invaluable to the cosmological community.

1.2 Physics of the 21-cm Hydrogen Line

Information about the evolution of the Intergalactic Medium (IGM) during the Dark Ages, Cosmic Dawn, and the Era of Re-ionization comes from the redshifted 21-cm line of neutral Hydrogen (HI). The origin of the 21-cm line can be understood by considering the hyperfine splitting of the ground state in the neutral Hydrogen atom. Hyperfine splitting results from the interaction between the magnetic moments of the proton and the electron in the ground state of the Hydrogen atom. The total angular momentum $\vec{F}$ of the Hydrogen atom is the sum of the total angular momentum $\vec{J}$ of the electron and the nuclear spin $\vec{I}$:

$$\vec{F} = \vec{J} + \vec{I} \tag{1.1}$$

In the ground state, the orbital angular momentum of the electron is zero ($l = 0$). Hence, the total angular momentum of the electron is just its spin angular momentum ($\vec{J} = \vec{S}$). Since both the electron and the proton have spin quantum numbers of $s = 1/2$, we can consider the ground state to be a system of two interacting spin-half particles. We can write the eigenstates of the interacting system using it's spin quantum number F and the z-component m. The total spin quantum number F takes values from $s_e - s_p, s_e - s_p + 1, ..., s_e + s_p$, which in this case are 0 and 1. $F = 0$ denotes the singlet state, whereas $F = 1$ is the triplet state. The energy transition between the singlet and the triplet state emits a photon of frequency $\nu = 1420$ Mhz that corresponds to the 21-cm line in cosmology.

Both of the states have $2F + 1$ degenerate energy levels, which correspond to the different z-component of the spin quantum number F. The z-component takes values from $-F$ to F, which in this case are $m = -1, 0, 1$ for the triplet state and $m = 0$ in the singlet state. These states can thus be represented by $|F, m\rangle$. The basis of the interacting eigenstates $|F, m\rangle$ can be written in terms of the z-component of the spins of the proton and the electron - $|m_p, m_e\rangle$, with m_p and m_e both taking values $\pm\frac{1}{2}$. The eigenstates in this basis are given in Fig 1. below. The coefficients can be obtained from the Clebsh-Gordon table, which relate the eigenstates to the basis states.

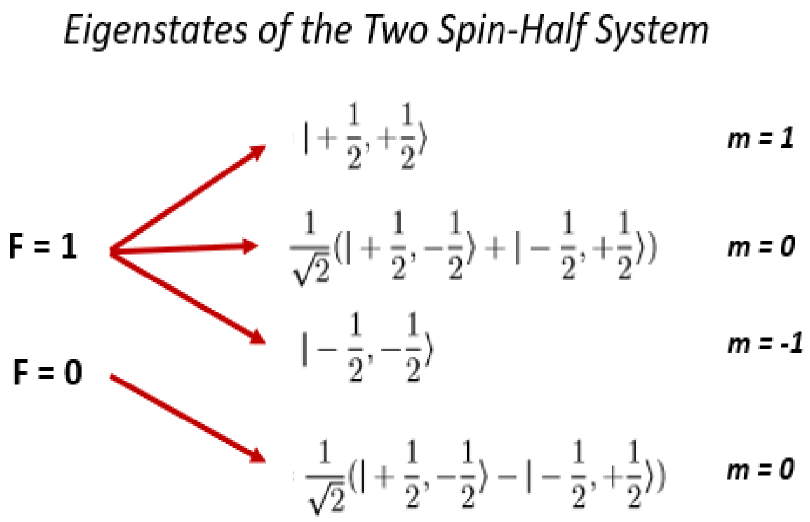

Figure 1.1: Eigenstates of the interacting two spin-half system of the proton and electron in the neutral Hydrogen atom.

1.3 Brightness Temperature

A fundamental quantity of interest is the brightness temperature of the 21 cm HI line. The intensity $I(\nu)$ of the 21 cm line is given by the Planck's black body spectrum. A good approximation for the intensity of the 21 cm line is the Raleigh-Jean's formula which allows us to write the brightness temperature of the 21 cm line as

$$T_b(\nu) \approx \frac{I_\nu c^2}{2k_B\nu^2} \tag{1.2}$$

Due to the expansion of the universe, the brightness temperature is red-shifted as it reaches us. As the 21-cm line travels through the hydrogen cloud there is radiative transfer which changes its intensity and hence its brightness temperature. As a result, the brightness temperature of the 21-cm line that emerges out of the cloud depends on the opacity $\tau(\nu)$ and the spin temperature of the cloud T_S.[9]

$$T_b(\nu) = T_S(1 - e^{-\tau(\nu)}) + T_\gamma(\nu)e^{-\tau(\nu)} \tag{1.3}$$

Here the CMB is assumed to be the background radiation and hence we have T_γ in the equation. The spin temperature is detailed in the next section. An exact calculation of the opacity of the IGM gives us the following expression [9]

$$\tau(\nu) \approx 0.0092(1+\delta_b)(1+z)^{3/2}\frac{x_{HI}}{T_S}\frac{H(z)/(1+z)}{dv_{||}/dr_{||}}K \tag{1.4}$$

where x_{HI} is the neutral fraction of hydrogen, δ_b is the overdensity of baryons, $dv_{||}/dr_{||}$ is the velocity gradient along the line of sight and $H(z)$ is th hubble parameter. The opacity of the IGM is very small and hence equation (1.2) can be linearly expanded in $\tau(\nu)$. The quantity of utmost importance is not the brightness temperature itself but deviation of this temperature from the CMB temperature, δT_b. This is the quantity that is measured by comparing the brightness temperature along the line of sight to the CMB temperature.[9]

$$\begin{aligned} \delta T_b(\nu) &\approx \frac{T_S - T_\gamma(z)}{1+z}\tau(\nu) \\ &\approx 0.0092(1+\delta_b)(1+z)^{1/2}x_{HI}\frac{(T_S - T_\gamma(z))}{T_S}\frac{H(z)/(1+z)}{dv_{||}/dr_{||}}K \end{aligned} \tag{1.5}$$

Hence, to detect the 21-cm signal the spin temperature needs to deviate from the CMB temperature.

1.4 Spin Temperature

To understand the spin temperature of the IGM, we need to understand the distribution of atoms in the singlet and the triplet state of the hydrogen gas in the IGM. The

Boltzmann distribution allows us to calculate the ratio in the occupation numbers of the singlet state n_0 and the triplet state n_1 of the hydrogen cloud at an equilibrium temperature T

$$\frac{n_1}{n_0} = \frac{g_1}{g_0} e^{-\frac{h\nu_{10}}{kT_S}} \tag{1.6}$$

where $g_i = 2F_i + 1$ is the degeneracy of the i_{th} state and T_s is defined as the spin temperature. One can also define the reference temperature $T_* = h\nu_{10}/k$ and hence we have [8]

$$\frac{n_1}{n_0} = 3e^{-\frac{T_*}{T_s}} \tag{1.7}$$

For the 21-cm line, the reference temperature $T_* \sim 0.068K$ was much smaller than the interstellar temperature. So the quantity in (1.7) implies that the triplet state had an occupational probability $\sim 3/4$.

The singlet state has a lower energy than the triplet state and hence one can have a spontaneous emission of a 21-cm photon due to the transition of an electron from the triplet to the singlet state. But the probability of such a spontaneous transition is extremely small $\approx 2.85 \times 10^{-15} sec^{-1}$ and is sub-leading to the processes involving induced emission and absorption. For the IGM, there were three mechanisms which contributed to the absorption and stimulated emission of the 21-cm photon, namely interaction with external 21-cm radiation photons, collisions between free electrons and hydrogen atoms and Wouthuysen-Field mechanism.[8]

External 21-cm radiation photons induced transitions between the two states of the neutral hydrogen atom. Such transitions are characterized by the brightness temperature defined as $T_R = \frac{\lambda^2}{2k}\bar{I}_\nu$ where $\bar{I}_\nu$ is the averaged brightness at 21-cm over the whole sky [8]. Similarly, collisions between electrons and atoms induced emission and absorptions of 21-cm photons. The probabilities for such transitions depend on the kinetic energy of the constituents and hence we can define a kinetic temperature T_K such that the probabilities depend only upon T_K.

Finally, the absorption of optical photons emitted due to radiative transitions between higher energy levels of hydrogen and its ground state also induced 21-cm photon emission in the IGM through the Wouthuysen-Field(WF) mechanism. The most important transition occured through the absorption of the Lyman-α photon. In the WF mechanism, the absorption of a Lyman-α photon induces an electron transition from the triplet/singlet ground state to an excited state of the hydrogen atom. When the electron returns to the ground state, it switches to the other hyperfine level. All such possible processes are shown in figure 1.2 below. The electric dipole selection rule only allows transitions with $\Delta L = \pm 1$ and $\Delta F = 0, \pm 1$ with the exception of $F : 0 \to 0$ being disallowed. Suppose an electron is in the 2S singlet state and absorbs a Lyman-α photon. The selection rules allow a jump to the triplet state $2\ {}_1P_{1/2}$ state. But now it can transition back to the triplet ground state $2\ {}_1S_{1/2}$ by the spontaneous emission of a Lyman-α photon. The transition $2\ {}_1S_{1/2} \to 2\ {}_1P_{3/2} \to 2\ {}_0S_{1/2}$ is also possible as illustrated in the figure. We can associate a temperature T_{WF} to the optical transitions such that the transition probabilities depend upon it.

Denoting the probabilities of $0 \rightarrow 1$ transition by P^i_{01} and that of $1 \rightarrow 0$ by P^i_{10} where i denotes the mechanism responsible for it, the probability ratio is given by [8]

$$\frac{P^i_{01}}{P^i_{10}} \sim 1 - \frac{T_*}{T_i} \tag{1.8}$$

We can assume that the hydrogen cloud is in equilibrium and hence the population of the singlet and the triplet states remains the same over time. This implies that the transitions in the directions $0 \rightarrow 1$ and $1 \rightarrow 0$ are equal.

$$n_1 \sum_i P^i_{10} = n_0 \sum_i P^i_{01} \tag{1.9}$$

From equations (1.7), (1.8), (1.9), and using the fact that $T_* \ll T_S$, one can readily arrive at the expression for the spin temperature T_S [8]

$$T_S = \frac{T_R + y_K T_K + y_{WF} T_{WF}}{1 + y_K + y_{WF}} \qquad y_K = 3\frac{T_R}{T_K}\frac{P^C_{10}}{P^R_{01}} \quad y_{WF} = 3\frac{T_R}{T_{WF}}\frac{P^{WF}_{10}}{P^R_{01}} \tag{1.10}$$

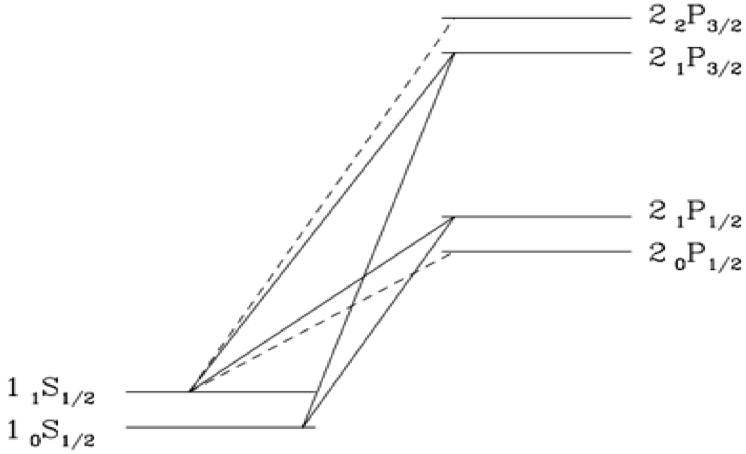

Figure 1.2: Wouthuysen-Field Mechanism

1.5 Thermal history of IGM

The theoretical understanding of the thermal history of the IGM provides us with clues of how the global 21 cm line evolved though different periods of time. During the initial period of the Dark Ages, Compton scattering between the CMB photons and electrons caused them to equilibrate thermally. This resulted in $T_S \sim T_K \sim T_\gamma$[22]. Hence there are no deviations in the brightness temperature $\delta T_b = 0$ and there is no detectable 21-cm signal from this time period.

As the universe expanded, the IGM started to cool adiabatically at a rate $\propto a^{-2}$ whereas the CMB photons cooled at a much slower rate $\propto a^{-1}$. This lead to the kinetic temperature of the gas in the IGM dropping below the CMB temperature, around $z \approx 200$. The density of the IGM was still high enough for the spin temperature to be strongly coupled to the kinetic temperature, and hence the spin temperature dropped below the CMB temperature to follow the kinetic temperature of the IGM ($T_S \sim T_K < T_\gamma$). Most models predict this to have happened around $z \approx 80$. Since $T_S < T_\gamma$, there is an absorption feature in this regime ($\delta T_b < 0$) [22]

As the gas cooled down further, its density decreased such that $y_K \ll 1$ and the spin temperature decoupled from the kinetic temperature. This led to $T_S \sim T_\gamma$ and hence there is no detectable signal in the region $30 < z < 40$.[22] This process of decoupling, initially from the CMB and then from the kinetic temperature of the IGM resulted in a dip during the dark ages which is illustrated in the Figure 1.3.

The first stars began forming around $z \approx 30$. This led to the emission of UV light which consisted of Lyman-α photons. These photons played a significant role in the WF mechanism and increased the temperature of the gas in the IGM. But this increase was not enough for the kinetic temperature to be of the order of the CMB temperature. Since collisions were enhanced, the spin temperature become strongly coupled to the kinetic temperature and this led to the spin temperature dipping below the CMB temperature ($T_S \sim T_K < T_\gamma$). As the redshift decreased, more Lyman-α photons were emitted and this saturated the Lyman-α coupling to the gas with $x_\alpha \gg 1$. In this region, there is an absorption spectrum.[22]

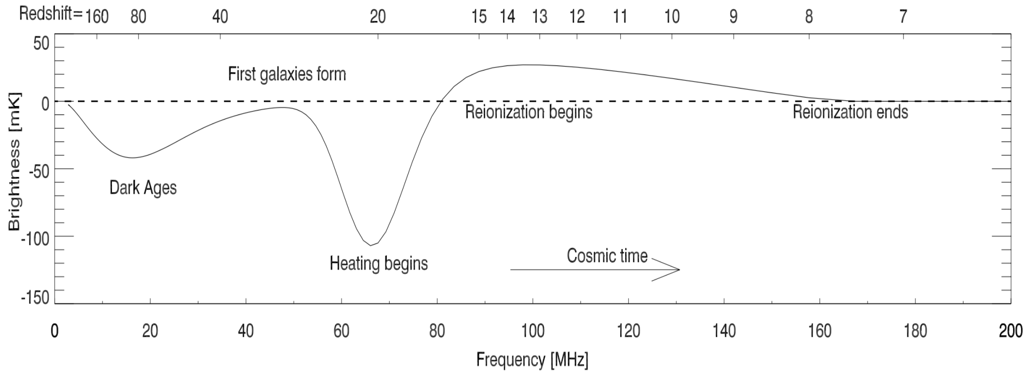

Figure 1.3: The Predicted Cosmological Signal

Once the Lyman-α coupling was saturated around $z \approx 20$, X-ray heating was the main source of fluctuations in the brightness temperature. X-ray photons heated the gas such that the kinetic temperature rose above T_γ, thereby creating an emission spectra ($\delta T_b > 0$)[22]. The main source of X-ray photons during this time period were black holes and AGNs. The Lyman-α and X-ray photons began to ionize the hydrogen gas as they traveled through the IGM.

As one moves to a redshift of $z \approx 17$, the kinetic temperature rises much higher than T_γ and the X-ray coupling saturates. The fluctuations are mainly dominated by the ionization of the hydrogen gas as the redshift further decreases. The intensity of the 21-cm signal reduces as one enters the epoch of re-ionization at $z \approx 13$ where majority of the hydrogen gas starts getting ionized due to the bombardment of energetic X-ray and Lyman-α photons. This period ends at $z \approx 6$ after which all of the hydrogen gas in the IGM has been re-ionized.[22]

The table below summarizes the key processes in the thermal history of the IGM and tracks the behavior of the spin temperature relative to the CMB temperature. Deviations of the spin temperature from the CMB temperature leave features in the 21-cm signal, with $T_s < T_\gamma$ leading to absorption features and $T_s > T_\gamma$ leading to emission features. When $T_s = T_\gamma$, there are no features in the 21-cm brightness temperature.

Coupling	**Spin Temperature**	**Physical Processes**
Collisional Coupling	$T_\gamma = T_s = T_k$ $T_\gamma > T_s = T_k$	Compton Scattering Adiabatic Cooling $T_k \propto a^{-2}$ $T_\gamma \propto a^{-1}$
Radiative Coupling	$T_\gamma = T_s > T_k$	Gas Too Dilute
Lyα Coupling	$T_\gamma > T_s = T_k$	UV Light from First Stars
X-Ray Heating	$T_\gamma < T_s = T_k$	Black Holes and AGNs

Table 1.1: Evolution of the Spin Temperature

1.6 Global All-Sky Average Experiments

Recently, the cosmological community has been very excited about the results published by the Experiment to Detect the Global Epoch of Reionization Signature (EDGES) [4]. The EDGES team found a flat absorption signal in the region $z \approx 20$ to $z \approx 15$ for the sky-averaged 21-cm temperature brightness spectrum. Although the range obtained above is in accordance with the predictions of most theoretical models, if their results indeed correspond to the cosmological signal, they suggest that the decoupling of the spin temperature from the background radiation happened at a much faster rate than models predict. The most surprising result was that the temperature anomaly at the center of the profile implies a ratio of T_R/T_S to be more than twice than what is currently accepted in the cosmological literature. This implies that either the radiation temperature in the early universe was much higher than predicted or that the gas temperature was much lower.

This could point to some exciting new physics in the early universe. Some models suggest that this discrepancy between theory and experiment might lead us to consider the increased interaction cross section between baryons and dark matter in the early universe, resulting in a lower gas temperature [2]. Other models suggest that the discrepancy can originate from the emission of synchrotron radiation from primordial black holes, which can increase T_R [3], or the relativistic electrons that result from the decay of metastable particles [6]. Although these results seem fascinating in their own right, other experiments with vastly different systems, methodologies, and systematics need to confirm this observation. Some of the experiments which have the capability to do this in the near future include LEDA [10], SARAS 2 [25], SCI-HI [27] and PRIZM [20]. Also there has been some criticism regarding the methodology used to model the ionosphere contribution within their experiment [12].

Chapter 2

High Z System Description

The High-Z system has three different versions, which I will discuss in this section. Each version was developed to upgrade the system from the previous version and was guided by significant lab testing, data analysis, and testing in the field. The block diagrams for each version are shown below, along with small notes on the changes made from previous versions. For each version, two block diagrams are shown, one for the Spectrometer Box and the other for the RF Box. We refer to the RF Box as the part of the electronic system that is located right underneath the antenna and includes the first amplifier, mechanical switch, internal calibrations sources, and filters. We refer to the Spectrometer Box as the part of the electronics that contains the data processing system and includes the ADC, SNAP spectrometer, RaspberryPi computer, and amplifiers and filters. Both the RF Box and the Spectrometer Box are constructed to be Faraday Cages to prevent radio frequency noise from the components within from leaking out of their containers. The boxes are connected to each other electronically by means of a long co-axial cable ($\sim 50m$).

2.1 Version 1

In version 1 of the High-Z system, which was deployed in the field at Karoo Site 4 in South Africa in July 2018, the signal from the antenna is sent through a small co-axial cable into one input terminal of the mechanical switch, where the signal then proceeds to go to the first amplifier. The effective cable length from the antenna terminal through the switch to the LNA chip is about five inches. The internal noise sources on the other input terminal of the switch include an ON/OFF noise source and an 50Ω load. The block diagrams that show the full electronics of both the RF Box and the Spectrometer Box are shown below.

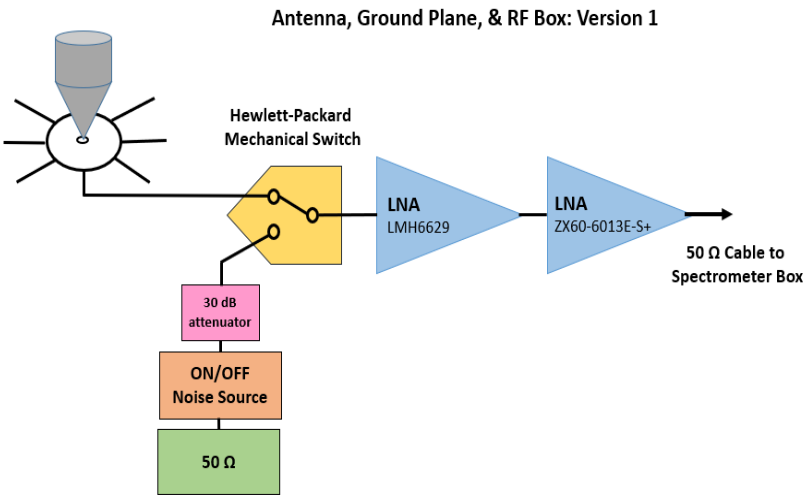

Figure 2.1: RF Box Version 1

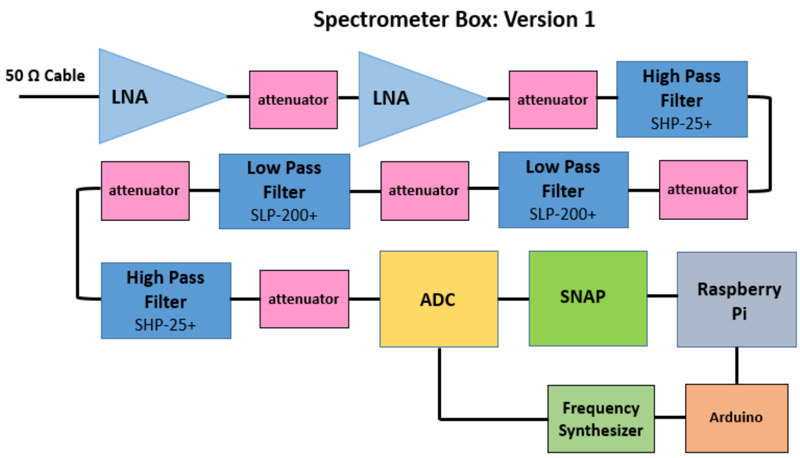

Figure 2.2: Spectrometer Box Version 1

2.2 Version 2

The data obtained from our deployment to South Africa in July 2018 was extremely valuable in guiding us to make further improvements to the experiment for the next deployment. Analyzing the data from 2018, we saw that overloading at low frequencies changed the temperature level across the entire frequency band. Therefore, to limit the overloading caused by strong signals outside of our frequency band, we moved both a High-Pass Filter and a Low-Pass Filter from the Spectrometer box to the RF box. Having both filters earlier in the electronic chain allows the strong signals outside of our frequency band to be attenuated before amplification later in the electronic chain. In addition, the data collected from the 2018 deployment revealed that the amplification in our electronic chain was insufficient. The signal received by the ADC was too low and did not use the full range of the ADC. To increase the signal level, we added an amplifier right before the ADC board in the Spectrometer box.

The most significant change we made to the experiment following the 2018 deployment is changing the position of the 1st amplifier in the electronic chain. Since both our antenna and the 1st amplifier are high impedance and the electrical path connecting them is 50 ohms, there will be large reflections of the signal at both the input of the 1st amplifier and the output of the antenna terminal. In fact, the signal from the antenna will undergo multiple reflections between the input of the 1st amplifier and the output of the antenna terminal, leading to large resonances in the spectrum. The degree of the impedance mismatch will control the amplitude of these resonances in the spectrum, while the length of the electrical path (i.e. the effective cable length) will control the number of resonance peaks in the spectrum. The shorter the electrical path between the antenna terminal and the input of the 1st amplifier, the less resonance peaks develop in our spectral range. If we minimize the electrical path length between the antenna terminal and the 1st amplifier, we can extend the remaining resonance peak out of the range of our spectrum, thereby providing a more smooth and flat spectrum. It is this realization which prompted us to move our 1st amplifier upstream, in front of the mechanical switch, to connect to the antenna terminal through a very short cable. By moving the 1st amplifier upstream, we greatly reduce the electrical path length between the high impedance antenna and the high impedance 1st amplifier, and thereby move any resonance peaks coming from reflections far out of our spectral range.

Our experiments in the lab following the 2018 deployment also revealed some instability in the noise source used in the calibration. When the noise source is turned on by a control signal from the Raspberry Pi, both the power level and the spectral shape of the noise source are initially very unstable. This instability disappears after a few minutes if the noise source remains turned on. Since the noise source in the 2018 deployment was turned on and off every calibration cycle, the instability in the power level and the spectrum of the noise source can present problems in the proper calibration of the sky signal. To address this, we decided to leave the noise source continuously turned on and to add a pin diode switch to alternate between the signal from the noise source and the 50 ohm load for the calibration cycle.

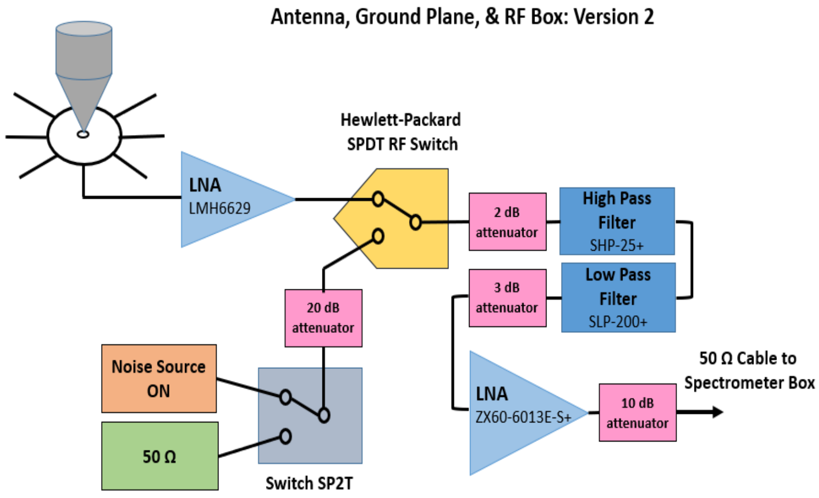

Figure 2.3: RF Box Version 2

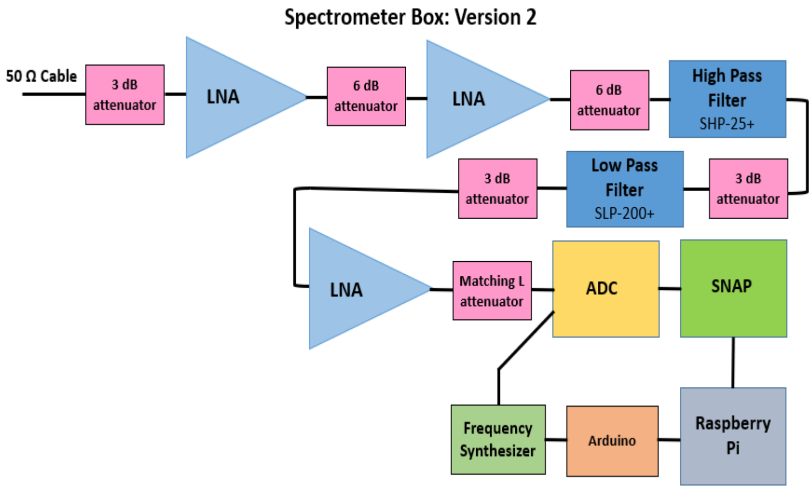

Figure 2.4: Spectrometer Box Version 2

Summary of the Changes Made from 2018 to 2019 Deployment:

- Moved 2 filters from the Spectrometer box to RF box to limit the overloading at low and high frequencies.
- Added an amplifier before the ADC board in the Spectrometer box to increase the signal level.
- Moved the 1st LNA to connect to the antenna and positioned the mechanical switch directly after the 1st LNA on the antenna side.
- Added a pin diode switch on the calibration side of the mechanical switch to alternate between the signal from the noise source and the 50 ohm load. Programmed the noise source to be continuously turned on.
- Reduced the attenuation on the calibration side of the mechanical switch from 30dB to 20dB.
- Switched to solar power
- Added water cooling system

2.3 Version 3

Version 3 of the High-Z system was deployed in the field at the Quarry site in Northern Quebec in October 2020. The upgrades in version 3 included changes only to the RF Box and the solar panels. More specifically, the changes to the RF Box consisted of the installment of a thermocron temperature sensor inside the RF Box, the removal of 13dB of attenuation, and the placement of the RF Box underneath the ground so that the radials would lay flat on the ground.

The decision to bury the RF Box underneath the ground was designed to make two improvements in our system: 1) attenuate the variations in the ambient temperature of the RF Box throughout the day and night 2) eliminate the height between the radials and the ground. The installment of the thermocron temperature sensor to record the variations in the ambient temperature of the RF Box as a function of time will be very useful to our field calibration methods. The changes to the solar panels included radio quiet regulators. An undergraduate student Sebastian Gamboa helped to develop these regulators so with the goal that they would be radio quiet and not leak radio noise into our system.

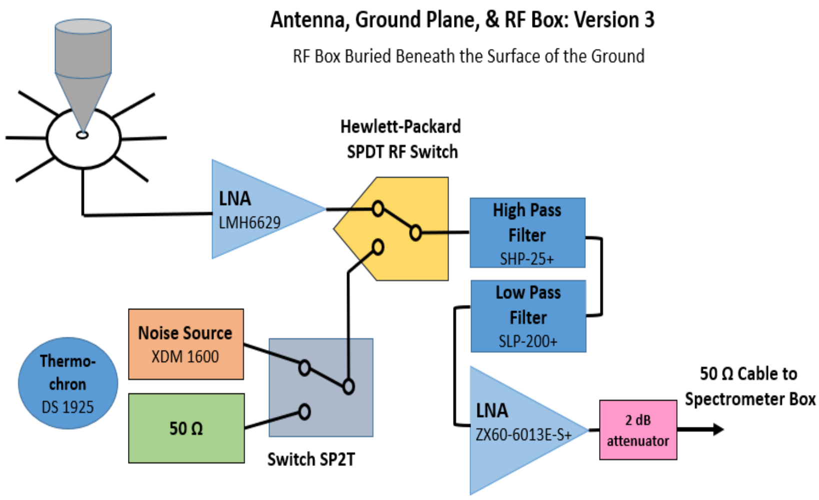

Figure 2.5: RF Box Version 3

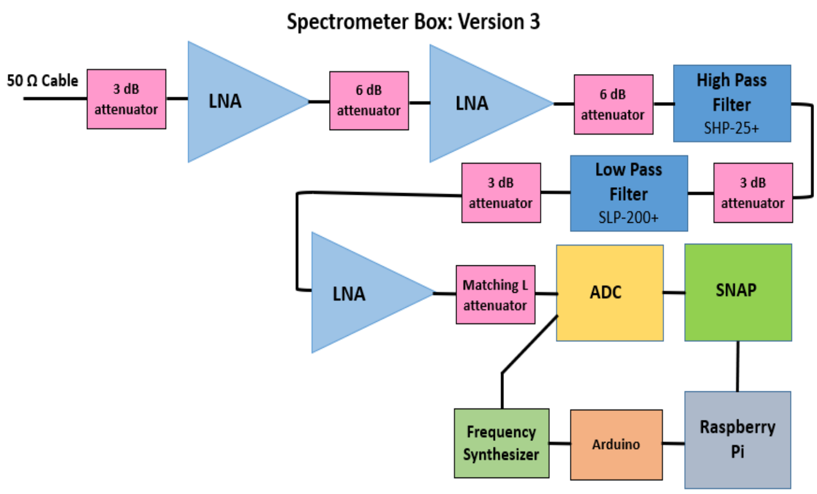

Figure 2.6: Spectrometer Box Version 3

Chapter 3

High Z System Calibration

The signal from the sky is converted from an electric field to a voltage by our active monopole antenna. This conversion factor depends on the antenna geometry and can be calculated numerically by solving the electrostatic boundary value conditions for the antenna. We call this conversion factor the Antenna Factor (AF), and it is a dimensionless factor that is frequency independent in the 0th order approximation. The voltage that is produced by the antenna in response to the incoming electric field from the sky can be described by the following equation:

$$V = AF * E_z * l \tag{3.1}$$

This voltage from the antenna is read directly by our high-impedance LNA. While most other global 21-cm groups use matching networks, where the voltage from the antenna is modified as it is read by the impedance-matched LNA due to the current flow between the antenna and the LNA, our system relies on the very high impedance of the LNA to measure the antenna voltage undisturbed.

Both the impedance of our antenna and LNA are much higher than the 50Ω impedance values in the systems used by other groups. The plots of the parallel resistance for one of our antennas (20cm) and the high-impedance LNA are shown below. In the plots, we see that the parallel resistance of our 20cm antenna is always above 1000Ω for frequencies below 100Mhz. The parallel resistance of the LNA exceeds the parallel resistance of our antenna after approximately 40MHz. The magnitude of the parallel resistance of the LNA then remains much higher than the parallel resistance of the antenna for the remaining frequency range.

One curious feature in the parallel resistance of the LNA, which we see in the plot, is the switch from a very high parallel resistance to a very low *negative* parallel resistance around 65Mhz. This arises from the reflection coefficient Γ_A of the LNA surpassing the maximum value of 1.0 on the Smith Chart. We will discuss this further in the section "Noise of the 1st Amplifier". The effect of the the LNA reflection coefficient being greater than 1 will impact the voltage sensed by the LNA from the antenna at the second order approximation of the antenna factor. Also, even though there seems to be a discontinuity in the impedance of our LNA at 65Mhz, in reality the impedance of the LNA is in fact very smooth, as a series impedance measurement of the LNA shows below.

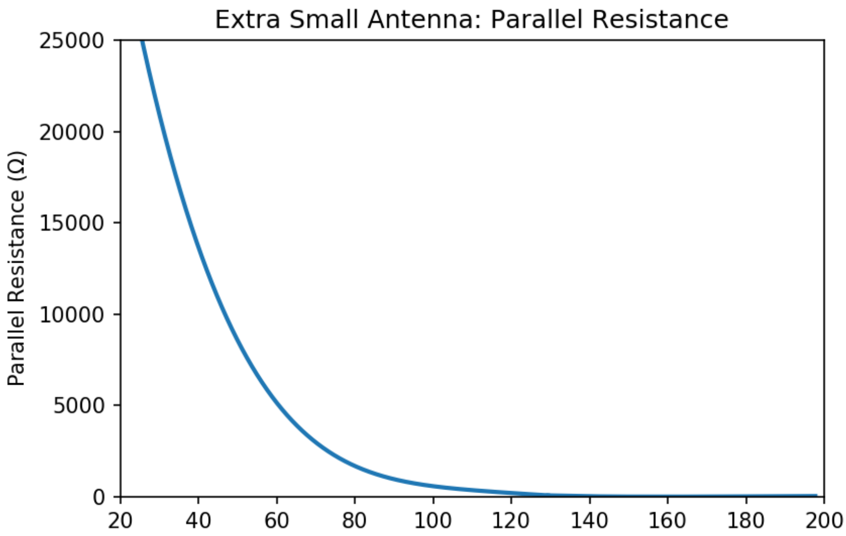

Figure 3.1: Parallel Resistance of Extra Small Antenna

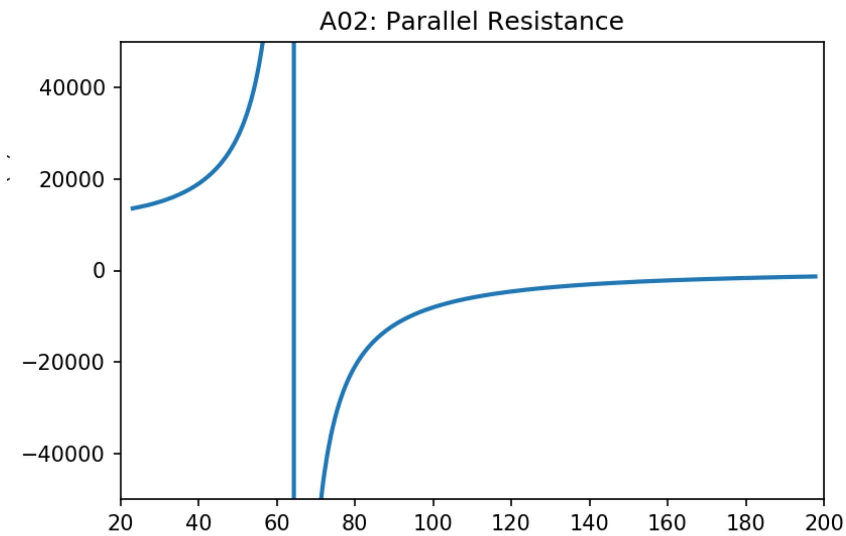

Figure 3.2: Parallel Resistance of First LNA

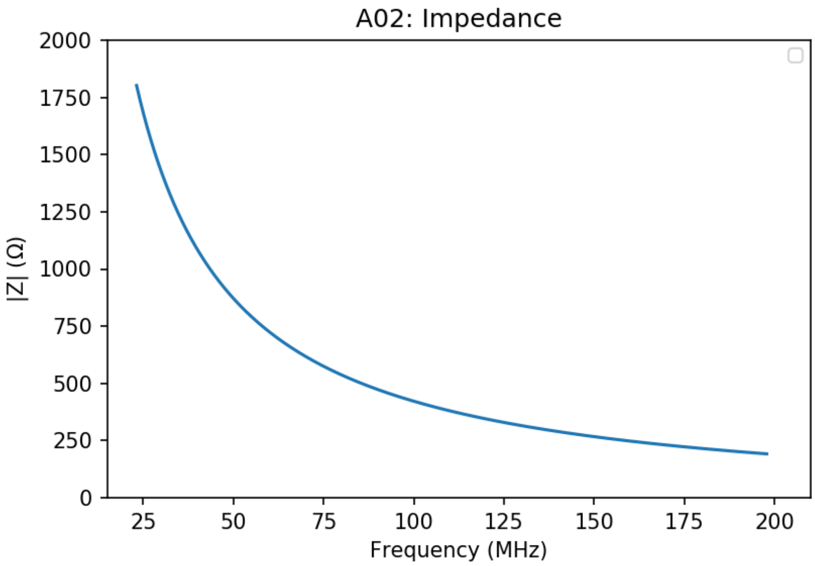

Figure 3.3: Impedance of First LNA

From the plots of the parallel resistance of our antenna and the LNA, we see that the impedance of the antenna and the LNA are not conjugate matches of each other. However, this mismatch is insignificant since the impedance of the LNA is much higher than the impedance of the antenna. The very high-impedance of the LNA prevents current from passing from the antenna to the LNA, thereby eliminating any frequency dependence in the response of the LNA to the voltage in the antenna. Our high-impedance LNA simply mirrors the voltage seen at the antenna terminal. This allows us to have a frequency independent response to the antenna voltage in a ulta-wide frequency band ($25Mhz < f < 200Mhz$). This frequency independent response can be altered if the LNA capacitance loads down the antenna, leading to quarter wave resonances $\lambda/4$ in the antenna factor AF. We see this quarter wave resonance for the medium antenna (54cm) in the frequency range around 125Mhz. However, the quarter wave resonances for the small and the extra small antenna (25cm and 20cm) is well pass our experimental frequency range.

3.1 Main Calibration Equations

The voltage variance that appears at the input of our first stage LNA must travel through the entire electronic chain of the High-Z system, where it is modified by a series of filters, attenuators, and amplifiers before reaching the spectrometer. In addition, as the voltage variance travels along the system's electronic chain, noise from the system components add to the original voltage variance signal. The noise from the first stage LNA, in particular, contributes the biggest portion of the system noise because it is added to the original signal at the earliest amplification stage and is therefore amplified more than any other system component noise. The voltage variance that enters the spectrometer is therefore very different than the original voltage variance at the input of the first LNA. In order to relate the voltage variance at the end of the electronic chain to the voltage variance at the input of the first LNA, a calibration procedure must be performed. Below I discuss the calibration procedure and the associated equations for calibration.

The calibration procedure begins with the measured output of the High-Z spectrometer. The raw spectrum produced by the FFT routine of the High-Z spectrometer is given in computer-generated units that must first be converted to the desired physical units before we can start analysis. This is because the voltage variance signal must go through an Analog-to-Digital-Converter (ADC), where the signal is converted from a voltage variance to a digital signal, before it enters the SNAP board, where the FFT routine is performed. The conversion from computer-generated units to physical units can be determined by doing a lab experiment where known voltage signals are fed to the ADC-Spectrometer system at various frequencies and then comparing the computer-generated spectrum with the known signals. This is exactly the procedure I performed early in the lab testing process using a frequency generator and the ADC-Spectrometer system. The lab-determined conversion factor, which I call "α", allows us to convert the raw spectrum of the High-Z spectrometer from computer-generated units to units of $|V|^2/Hz$. This conversion is summarized by the equation below, with B denoting the bandwidth:

$$\frac{|V_{measured}|^2}{B} = \alpha * \text{Raw Spectrum} \tag{3.2}$$

However, $|V|^2/Hz$ are not the final units of choice for analyzing our spectrum. The physical units we prefer to work with are noise temperature units rather than voltage squared per unit bandwidth units.

Noise temperature is different from physical temperature even though both are measured in units of Kelvin. Noise temperature in the context of our experiment is an effective temperature that compares the noise power (per unit bandwidth) seen in the measured spectrum of the High-Z spectrometer to the Johnson noise power (per unit bandwidth) produced by a 50Ω resistor. The Johnson noise power of a 50Ω load is a standard point of reference in electronics and allows us to convert spectra from units of $|V|^2/Hz$ to noise temperature in a consistent and unambiguous way. The equation that describes this conversion to noise temperature units is just the Johnson-Nyquist noise equation rewritten:

$$T_{measured} = \frac{|V_{measured}|^2}{4k(50\Omega)B} \tag{3.3}$$

Equation (3.3) more precisely defines the noise temperature as the temperature a 50Ω resistor must have to produce the Johnson noise power spectral density equivalent to that seen in our High-Z measured spectrum. One thing to note here is that the noise temperature in most impedance matching systems does not contain a factor of 4 due to the fact that the Johnson voltage drops by a factor of 2 (and hence Johnson noise power by a factor of 4) due to the voltage divider between the 50Ω resistor and the 50Ω receiving device. However, in our case, we keep the factor of 4 because our system is not a matching system. We account for voltage reductions due to impedance mismatches separately in our calibration equations.

After our raw spectrum is converted to noise temperature units using equations (3.2) and (3.3), we can begin to look at how the noise temperature changes as the signal propagates from the input of the 1st LNA down the electronic chain to the spectrometer. First of all, the noise temperature measured by the High-Z spectrometer is greatly amplified from the original noise temperature seen at the input of the 1st LNA. This amplification is performed by a series of amplifiers in both the RF Box and the Spectrometer Box and is necessary because the sky signal detected by the antenna is too weak to be analyzed by the spectrometer directly. Although all efforts are made to keep the amplification stage frequency independent, most amplifiers have gains that are slightly frequency dependent in reality and some amount of frequency dependence is also introduced by a series of low-pass and high-pass filters in the electronic chain. These filters are necessary to block strong signals outside our desired frequency range that can overload the system or cause interference inside our frequency band due to intermodulation. As a result of these effects, the amplification of the noise signal as it travels from the input of the first LNA to the spectrometer could be frequency dependent. We call this amplification the system gain G.

The amplification of the original signal is not the only change introduced by the electronic chain of the High-Z system. Each component in the electronic chain contributes its own Johnson noise to the original signal, thereby increasing the original signal. The noise contribution of the first LNA is especially important because it is introduced at the earliest stage of amplification and therefore dominates the noise contribution from all the electronic components in the system. As a result of the first LNA's dominant role in the noise contribution from the High-Z electronic chain, the total noise temperature added to the original signal is referred to as "amplifier temperature" and denoted by T_{amp}.

The amplification of the original signal and the addition of a noise temperature from the first LNA are the two main effects that need to be accurately and precisely determined by the receiver calibration method. The noise temperature added by the first LNA must be understood and analyzed very carefully not only because it is the largest source of added noise from the system, but also because its noise temperature is comparable to the expected brightness of the sky ($\sim 400K$). Therefore, we must make sure that any features detected in the measured temperature spectrum are not a result of the LNA.

Part of the difficulty of understanding and determining the noise temperature of the 1st LNA is that it varies depending on the impedance of the antenna connected to the LNA, the temperature of the components, and the temperature of the LNA itself. In addition, for the second and third versions of the High-Z system, the noise temperature of the LNA cannot be determined directly from a calibration performed in the field due to its position upstream of the mechanical switch. Therefore, determining the noise temperature of the 1st LNA accurately and precisely in the laboratory is one of the major goals of our calibration.

Once the system gain G and the noise temperature of the 1st amplifier T_{amp} are determined in the lab or in the field, the noise temperature measured by the High-Z spectrometer, denoted by T_m, can be related to the original signal at the input of the 1st LNA through the following calibration equation:

$$T_m = G\left(T_s + T_{amp}\right) \tag{3.4}$$

The quantity T_s represents the noise temperature of the source at the input of the first LNA and will be referred to as the "source temperature". In the field, the source temperature T_s is the sky temperature as seen by the antenna, which modifies the sky signal through the antenna factor as discussed previously. In the lab, the source temperature T_s is the Johnson noise temperature of loads of different impedances as seen through cables of varying lengths. The noise temperature of the 1st amplifier T_{amp} is referenced to the input of the amplifier so that both the signal noise and the amplifier noise experience the same system gain G.

The input-referred noise temperature of the first LNA consists of two terms - a voltage noise and a current noise. The voltage noise of the amplifier, denoted by T_{VN}, corresponds to the Johnson noise of the resistive components inside the amplifier, including the feedback resistors. The current noise of the amplifier, denoted by T_{CN}, corresponds to the voltage generated by the impedance of the source when a bias current from the amplifier flows into the source. The voltage noise and the current noise add to produce the total input-referred noise temperature of the first LNA:

$$T_{amp} = T_{VN} + T_{CN} \tag{3.5}$$

Both the voltage noise T_{VN} and the current noise T_{CN} are given in units of noise temperature relative to the 50Ω load. Recall that noise temperature is just an effective temperature that describes the temperature a 50Ω resistive load would need to have to produce the same amount of noise power (per unit bandwidth) at room temperature as the source of the noise measured. We choose the units of noise temperature relative to the 50Ω load so that all temperatures in our calibration are relative to the same reference point. However, we can rewrite the voltage and current noise terms of the first amplifier in terms of voltage rather than noise temperature to see how the two noise terms differ in their contribution to the total noise temperature of the amplifier:

$$T_{amp} = \frac{|V_{VN}|^2 + |IZ_{source}|^2}{4k(50\Omega)} \tag{3.6}$$

The voltage in the term $|V_{VN}|^2$ is the sum of all the Johnson noise voltages produced by the resistive components in the amplifier, referenced to the input of the amplifier. Since the Johnson noise voltage of any resistor is proportional to the square root of the physical temperature of that resistor, the voltage noise term $\frac{|V_{VN}|^2}{4k(50\Omega)}$ should be directly proportional to the physical temperature of all the resistive components in the amplifier. Therefore, if we determine the voltage noise term of the amplifier at one specific temperature in the lab, we can predict how it will vary with temperature in the field, as long as the physical temperature of the amplifier in the field is recorded.

The current noise term depends on the bias current I of the first LNA as well as the impedance of the source. Although the amplifier chip specifications sheet gives a nominal value and frequency dependence plot for this bias current, that value and plot are generated by computer simulations and not verified by direct measurement. Furthermore, the plot in the specifications sheet showing the frequency dependence of the bias current does not extend into the frequency range for our experiment. Therefore, we must carry out lab experiments to determine the exact value and frequency dependence of the bias current for the frequency range relevant to our experiment.

A significant portion of our lab testing is dedicated to experimentally determining the voltage noise and the bias current of our first LNA for the frequency range in our experiment. In the section "Noise Temperature of the First Low-Noise Amplifier", I will describe three different sets of experiments that were designed and performed in the lab to experimentally measure these quantities. Once the voltage noise and the bias current of the first LNA are determined in the lab, we use those quantities in equation (3.6) to determine the total noise temperature generated by the first LNA when it is connected to the antenna (i.e. when Z_{source} is the impedance of the antenna).

Lab experiments and measurements must also be performed to accurately and precisely measure the system gain G of the electronic chain from the input of the first LNA to the spectrometer. The system gain can be measured directly through a Vector Analyzer Network (VNA) device or it can be determined by measuring the spectra of two known noise sources. In the section "Absolute Calibration", I describe how the system gain is determined in the lab using a 50Ω Johnson load at two different temperatures. In the section "Transfer Calibration", I describe how the system gain is determined in the field from the measured spectra of an artificial noise source and a 50Ω Johnson load at one specific temperature.

3.2 Absolute Calibration

An absolute calibration of the High-Z system describes the careful process of determining the system gain G and amplifier noise temperature T_{amp} using a set of resistances at two different temperatures. The resistances replace the antenna in the system and function as known noise sources in the calibration process. Resistive loads are a source of electronic noise called Johnson noise. Johnson noise, or more formally Johnson-Nyquist noise, is a type of noise that is generated when the random thermal motion of charge carriers in a conductor creates a voltage that depends on the resistance as well as the temperature of the conductor. The equation for the Johnson noise rms voltage of a resistor R at a physical temperature T can be derived through statistical methods and is given by the following equation:

$$V_J = \sqrt{4kTRB} \tag{3.7}$$

Johnson noise voltage has a constant spectral density at low frequencies, which makes it ideal as a known noise source for calibration methods. However, Johnson noise voltage does depend on the bandwidth B of the instrument. We have chosen to divide out the bandwidth for all of our voltage quantities so that we are dealing with the voltage per square root of unit bandwidth (or voltage squared per unit bandwidth). This is a standard practice in electronics and electronic data sheets often report noise parameters in units of voltage per square root of unit bandwidth.

Since Johnson noise voltage depends on both the resistance R and temperature T of the load, varying both quantities allows us to modify the Johnson noise voltage in predictable ways. In our calibration methods, we vary both the resistance and the temperature of the loads we use as known Johnson noise sources. The temperature variation allows us to obtain the system gain G, as well as the total amplifier noise temperature T_{amp} for the specific loads connected to the High-Z system. However, as we shall see in the section "Noise of the First LNA", the total amplifier noise temperature T_{amp} changes with the impedance of the source connected to the LNA. Therefore, to determine the correct total amplifier noise temperature T_{amp} for the range of impedance values presented to the amplifier by the different antennas, we must use a variety of resistances in our calibration method.

Let us first describe how varying the temperature of a Johnson load allows us to determine the system gain G. As we discussed earlier, the known noise temperature of the source T_s and the noise temperature measured by our spectrometer T_m can be related to each other through equation (3.4). However, the system gain G and the total amplifier noise temperature T_{amp} in equation (3.4) are unknowns. To solve for the system gain G and total amplifier noise temperature T_{amp}, we measure the noise temperature spectrum of a 50Ω Johnson load at two different temperatures. We have chosen to measure the spectrum at room ($T = 290K$) and liquid nitrogen ($T = 77K$) temperatures because of the stability of those temperature measurements. We have also tried to measure the spectrum at higher temperatures using a self-made oven with a temperature regulator. However, significant temperature gradients and drifts, along with noise contributions from the temperature regulator itself, made it difficult to reliably use the higher temperature data.

The 50Ω Johnson load connects to the first LNA through a short co-axial cable, which allows us to dip the 50Ω Johnson load into liquid nitrogen without exposing the first LNA to the liquid nitrogen temperature. The cable we use to connect the 50Ω Johnson load to the first LNA is a 13cm LMR-200 co-axial cable with a resistance of 50Ω. The length of the cable was chosen to be short enough to prevent any cable resonances from appearing in our frequency band but long enough to keep the first LNA far enough away from liquid nitrogen to maintain a constant temperature.

The insertion of the 50Ω co-axial cable between the load and the LNA also explains our choice of using the 50Ω Johnson load for the derivation of the system gain G in our calibration. When deriving the system gain G, we want to minimize any standing waves in the cable resulting from impedance mismatches at the cable boundaries. Our high impedance LNA will inevitably cause a reflection of the voltage wave at the cable-LNA boundary due to the large mismatch of impedance between the 50Ω cable and the high impedance LNA. However, if the Johnson load is matched to the cable, as in the case of the 50Ω load and the 50Ω cable, there will be no reflections at the load-cable boundary, thereby eliminating any standing waves in the cable that could affect our system gain G derivation. Of course, our 50Ω Johnson load is not ideal and there will be a small reflection at the load-cable boundary. However, the short length of the cable can move the resonance of any standing waves in the cable outside of our frequency band.

Once we measure the noise temperature spectrum of a 50Ω load at room and liquid nitrogen temperatures, we can use equation (3.4) to write two separate equations, one for each temperature, relating the measured spectra to the known spectra of the 50Ω

Johnson load:

$$T_{m,room} = G\,(T_{s,room} + T_{amp}) \tag{3.8}$$

$$T_{m,cold} = G\,(T_{s,cold} + T_{amp}) \tag{3.9}$$

In equations (3.8) and (3.9), the source temperatures $T_{s,room}$ and $T_{s,cold}$ denote the known Johnson noise temperatures for a load resistance R at physical temperatures $T = 290K$ and $T = 77K$, respectively. For a 50Ω load, the Johnson noise temperatures are just the physical temperatures, since noise temperature was defined relative to the 50Ω Johnson load. However, since our 50Ω load is not perfectly 50Ω across the entire experiment frequency spectrum, the source temperatures for our load will be slightly different than the physical temperatures. For a load with a resistance R, including the resistance of our non-ideal 50Ω load, the source temperatures are given by:

$$T_{s,room} = \frac{290K * R}{50\Omega} \tag{3.10}$$

$$T_{s,cold} = \frac{77K * R}{50\Omega} \tag{3.11}$$

The factors $\frac{290K}{50\Omega}$ and $\frac{77K}{50\Omega}$ in the equations above allow us to write the Johnson noise temperature of the resistance R relative to an ideal 50Ω Johnson load. The resistance R of the non-ideal 50Ω Johnson load we use in our calibration is measured with our portable Vector Network Analyzer (VNA).

We assume that G and T_{amp} remain constant in equations (3.8) and (3.9) because we only change the temperature of the source resistor, not of any other component in the system, when performing the room temperature and liquid nitrogen tests. Solving (3.8) and (3.9) for G and T_{amp}, we get:

$$G = \frac{T_{m,room} - T_{m,cold}}{T_{s,room} - T_{s,cold}} \tag{3.12}$$

$$T_{amp} = \frac{T_m}{G} - T_s \tag{3.13}$$

In equation (3.13), T_m and T_s can be either "room" or "cold". The system gain G and the total amplifier noise temperature T_{amp} in equations (3.12) and (3.13) can be understood graphically as the slope and y-intercept of a line defined by two points on a plot of the measured vs source noise temperature of the 50Ω load (See figure 4). In the plot, the x coordinate axis represents the known Johnson noise temperature of the load and the y coordinate axis represents the noise temperature measured by our spectrometer (SNAP). Both noise temperatures are referenced to the Johnson noise temperature of a 50Ω load. The two points that define the line correspond to the two different noise temperatures of the load - one at room temperature and another at liquid nitrogen temperature. The slope of the line between these two noise temperature points allow us to determine the gain G of the system, as defined in equation (3.12), while the y-intercept of the line allows us to extrapolate the noise temperature of the load to zero in order to isolate the noise contribution of the first LNA to the total measured spectrum.

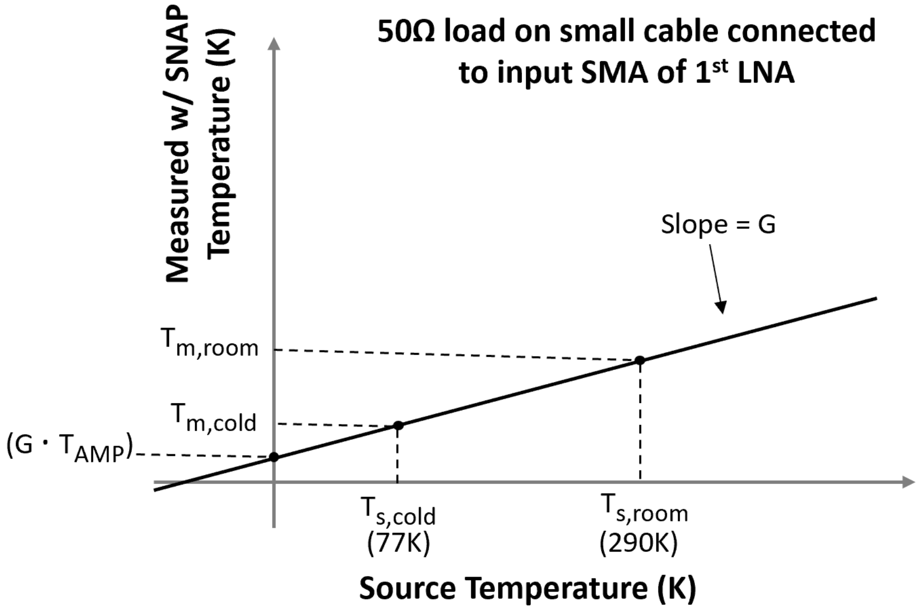

Figure 3.4: Measured vs Source Temp

It is worth noting a few things about the plot in figure X. First of all, the plot shown represents only one frequency, whereas the system gain G and total amplifier noise temperature T_{amp} in equations (3.12) and (3.13) are calculated for all frequencies in our experimental band. Second of all, the total amplifier noise temperature T_{amp} in the plot and in equation (3.13) refers to the total noise temperature of the first LNA only when a 50Ω load is connected to the LNA. The total noise temperature of the LNA changes when the antenna is connected to the LNA. Finally, we are making an assumption of linearity when determining the system gain G. Although we attempted to experimentally verify this assumption of linearity by measuring the noise temperature spectrum of the 50Ω load at higher temperatures, the unreliability of the higher temperature data made it difficult to confirm. Nevertheless, there are other ways of obtaining the system gain G that can increase our confidence in the accuracy of the system gain G obtained by this method.

The system gain G can be measured directly by a Vector Network Analyzer and compared with the system gain G derived from equation (3.12). However, a measurement of the system gain G using a VNA introduces a different set of errors than the derivation of G using the measured spectra of a 50Ω load at two different temperatures. First of all, the output impedance of the VNA ports used for making the S21 measurement that gives the system gain G are not perfectly 50Ω. In fact, for our portable VNA, the output impedance of both ports was measured to be 82Ω. Therefore, some reflections will be introduced into the S21 measurement of the High-Z system and these reflections will create standing waves in the cables used to connect the VNA to the High-Z system. These standing waves will, in turn, add to the error in the system gain G measurement. We can minimize these standing waves by adding matching attenuators on both ports of the VNA that will modify the output impedance of the VNA to more closely match the characteristic impedance of the cables. In all of our measurements with the portable VNA, we use matching attenuators on both ports of the VNA. However, small reflections may still occur, leading to errors in the measurement.

Another problem with making a direct measurement of the system gain G using a VNA is that we must use a very low power output signal on the VNA, as well as considerable amount of attenuation, when making the S21 measurement of the High-Z system to prevent the saturation of the amplifier. Overloading of the amplifier can lead to distortion and ringing in the lower frequencies, which are undesirable in our system gain G measurement. However, the very low power output signal on the VNA and the added attenuation make the system gain G measurement on the VNA very noisy. We can improve the noisiness of this measurement by averaging, which is what we have done.

Below are two plots of the system gain G. The first plot shows the system gain G derived using equation (3.12) from the measurement of the noise temperature of the 50Ω load at room and liquid nitrogen temperatures. The second plot shows the system gain G measured directly with our portable VNA, using matching attenuators on both ports of the VNA, an output power signal of 43dBm on the VNA, and an attenuation of 23dB. The measurement is averaged over 5 sweeps of the VNA.

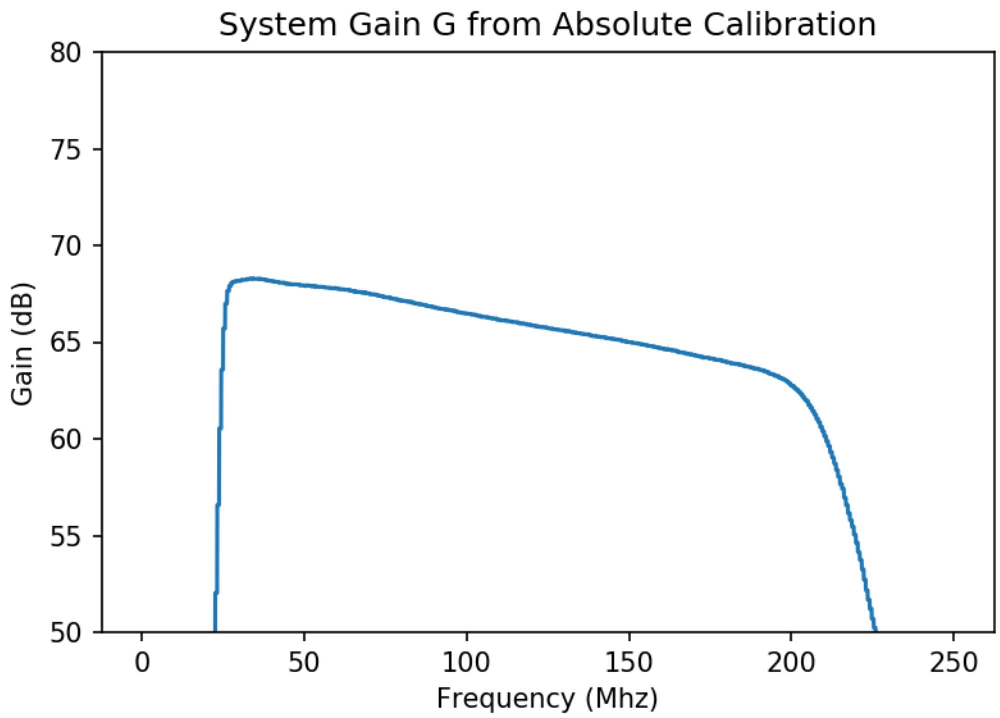

Figure 3.5: System gain G derived using equation (3.12) from the measurement of the noise temperature of the 50Ω load at room and liquid nitrogen temperatures.

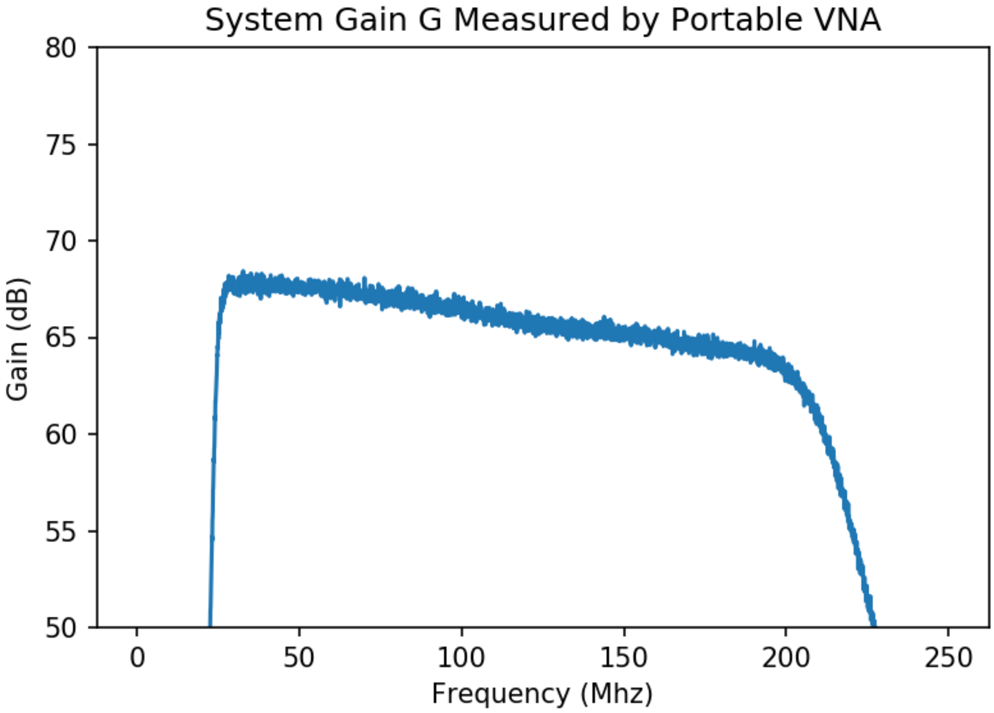

Figure 3.6: System gain G measured directly with our portable VNA. The measurement is performed with matching attenuators on both ports of the VNA, an output power signal of 43dBm on the VNA, and an attenuation of 23dB. In addition, the measurement is averaged over 5 sweeps of the VNA.

Although verifying the system gain G remains the same with temperature changes is difficult for the system as a whole, we can verify that the gain of the first LNA doesn't change with temperature. Indeed, this is crucial due to the fact that the field calibration doesn't include the first LNA in the second and third versions of the experiment. If the gain of the first LNA doesn't change with temperature, and the gain of the rest of the system doesn't change with temperature in the field when derived using the field calibration, then we are correct in assuming that the total system gain G does not change with temperature.

The stability of the gain of the first LNA with temperature changes can be verified by performing a S21 measurement with the portable VNA when the LNA is exposed to freon and then heated by a heat gun. Those measurements of the gain can then be compared to the gain measurement of the LNA at room temperature. Below is a plot with three gain curves corresponding to the LNA at temperatures 238K, 293K, and 373K. From this plot, we see that the gain of the first LNA remains stable with temperature change in the frequency range from 20Mhz to 150Mhz, but decreases slightly toward higher frequencies. The maximum change in gain is approximately 0.2dB at 200Mhz.

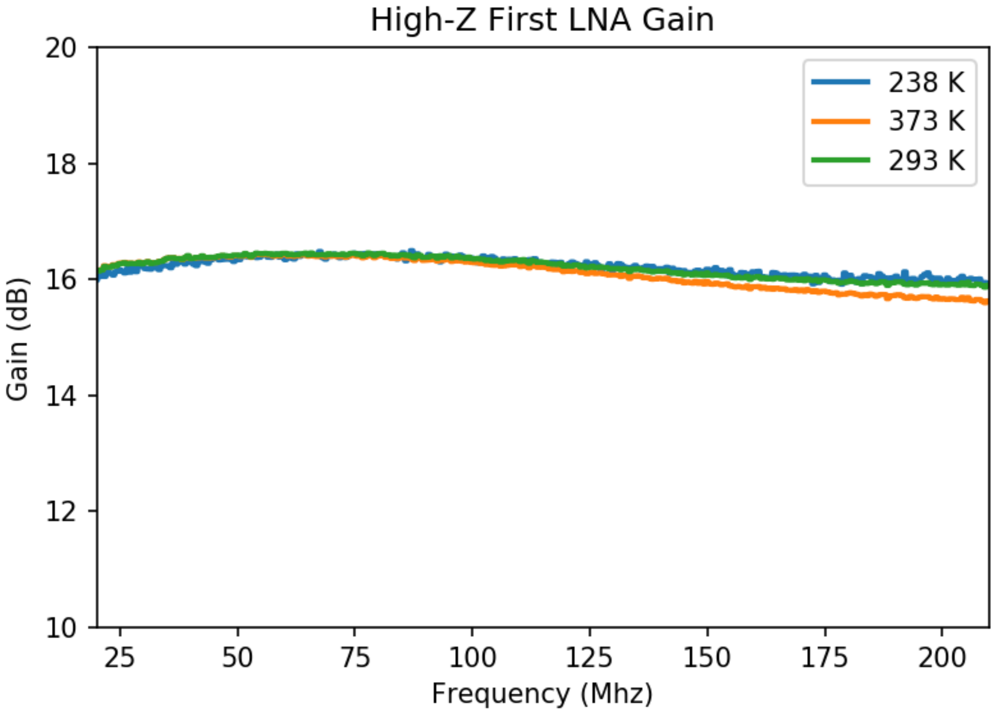

Figure 3.7: First LNA Gain at Different Temperatures. Gain measurements were taken by the portable VNA, with 20dB output power level of the VNA, matching attenuators on both ports, 20dB attenuation in total, and averaging of 5 sweeps.

The S21 measurement that gives us the gain of the first LNA must be performed after calibrating the VNA by connecting port 1 to port 2 of the VNA using a co-axial cable. Matching attenuators must be placed on both ports of the VNA to match the output impedance of the VNA to the co-axial cable, which is 50Ω. In addition, 10dB attenuation on each port must be placed to prevent the overloading of the amplifier, which can skew the correct gain measurement of the amplifier by causing compression, ringing, or distortion. Matching attenuators and the 20dB attenuation is present during the calibration of the VNA with the cable. After calibrating the VNA, the first LNA is inserted between the attenuator and the cable and a S21 measurement is performed. This allows us to obtain the gain measurement of the first LNA. Below is a picture of the first LNA being heated by a heat gun to measure the gain of the LNA at 373K. The temperature of the LNA was recorded by using a type K Thermocouple. The sensors of the thermocouple were pressed against the chip of the first LNA for the temperature measurements.

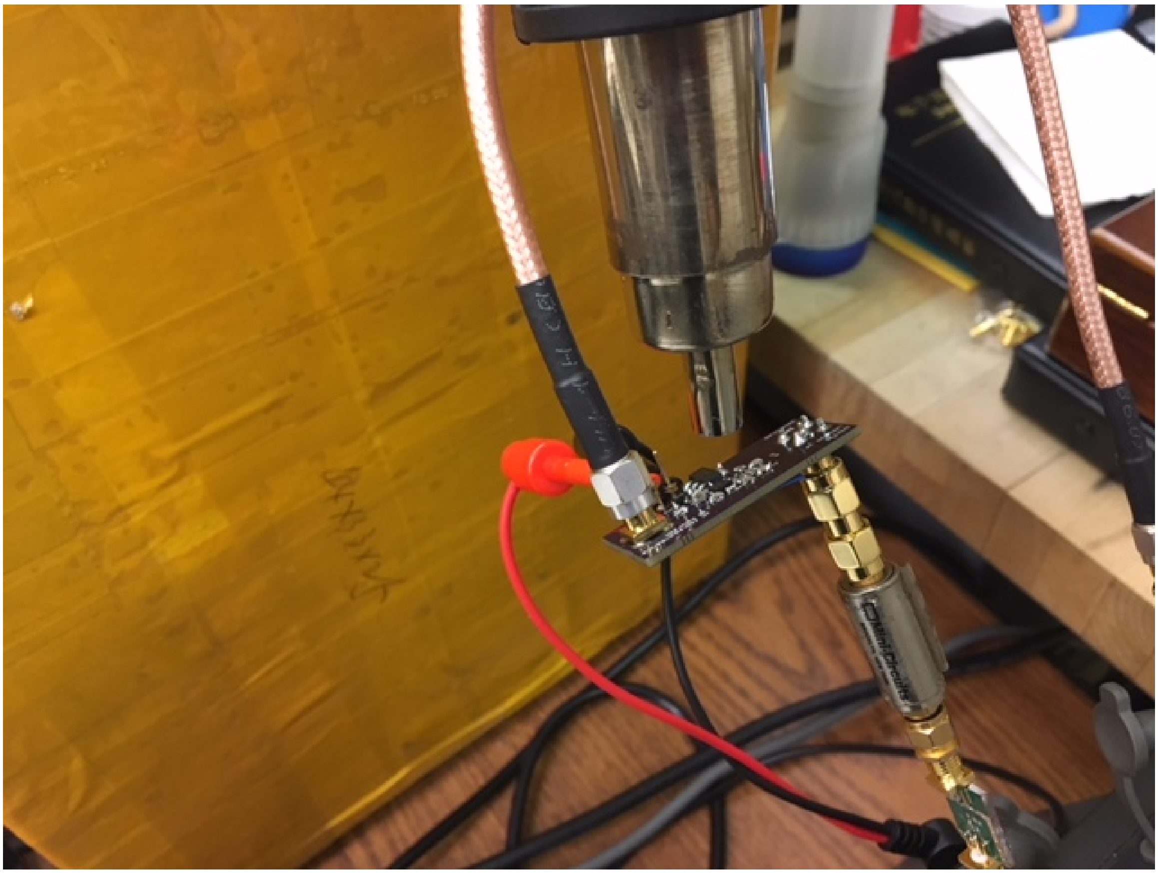

Figure 3.8: Heating the First LNA

Once the value of the system gain G has been determined by measuring the spectra of a 50Ω load on the end of a 13cm co-axial cable at room (290K) and liquid nitrogen (77K) temperatures, we then seek to determine the correct total amplifier noise temperature T_{amp} for the set of antennas we will use in the field. Recall from equation (3.6) that the input-referred total amplifier noise temperature T_{amp} depends on the impedance of the source Z_{source} attached to the amplifier. If the antenna had just one value of impedance for the entire frequency band in our experiment, we could just find the right combination of a resistor, capacitor, or inductor to match the impedance of the antenna and then use this combination as our source for the absolute calibration. We could then determine the correct total amplifier noise T_{amp} for the antenna using equation (3.13) [cite Kevin Bandura for the idea]. However, the impedance of each antenna varies with frequency, which makes it more difficult to use just one combination of a resistor, capacitor, and/or inductor as the source for the absolute calibration. We have attempted to perform an absolute calibration using an idea very similar to this for a set of frequencies in our band, but encountered problems with this method, which I will explain in section [note which section].

Instead of using various combinations of resistors, capacitors, and inductors that match the source impedance of the antenna $Z_{antenna}$ at each frequency, we have chosen to approach the problem of determining the total amplifier noise T_{amp} in another way. Our approach is to investigate the individual noise components of the amplifier and study how they change with the source impedance Z_{source}. If the two noise components of the amplifier - the voltage noise and the current noise - are uncorrelated in the frequency range of our experiment, we can determine the two components separately and then add them to obtain the total amplifier noise T_{amp}. More specifically, if we can obtain the voltage noise $|V_{VN}|^2$ and the bias current I of the amplifier, we can use equation (3.6) and the measured impedance of the antenna $Z_{antenna}$ to calculate the total amplifier noise temperature T_{amp} for the case when the antenna is connected to the input of the LNA.

We have explored several different methods for investigating how the two noise components of the LNA vary with the source impedance Z_{source}. We describe these methods in more detail in section "Noise of the First Amplifier", where we show how these methods allow us to obtain the voltage noise $|V_{VN}|^2$ and the bias current I of the LNA. One of the methods involves replacing the antenna with Johnson loads of different resistances, which are attached at the end of a long co-axial cable to the LNA, and then measuring the cable filtered Johnson noise of those loads with the High-Z system. We developed this method after discovering large resonances in our measured spectra for loads with resistances greater than 50Ω at the end of cables of length 63cm and longer. An example of these resonances is shown in the plot below.

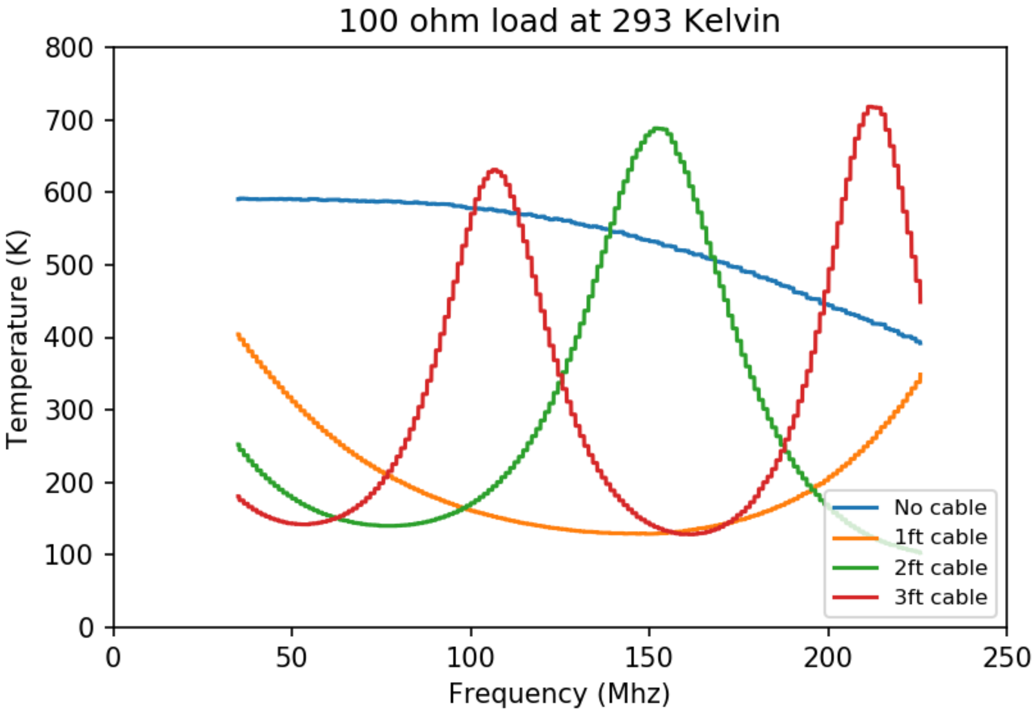

Figure 3.9: Cable Resonances for 100Ω Load at 293K

After obtaining the value of G from absolute calibration and T_{amp} from the methods discussed in section "Noise of the 1st Amplifier", we can proceed to use them in deriving noise temperature of the source:

$$T_s = \frac{T_m}{G} - T_{amp} \tag{3.14}$$

When an antenna is connected to the system rather than a load, equation (3.14) gives the noise temperature from the antenna as measured by input terminal of the LNA. It is very important to remember that T_{amp} will be different for different antennas, so we must use the correct value of T_{amp} for the respective antenna.

3.2.1 Multiple Reflections

The practical implications of measuring the spectra of resistive loads submerged in liquid nitrogen necessitate the use of co-axial cables. These co-axial cables connect the submerged loads to the first amplifier without exposing the amplifier itself to the cold liquid nitrogen temperature. However, the insertion of a co-axial cable in between a resistive load and the first amplifier modifies the Johnson noise voltage coming from the load to the input of the amplifier. In particular, the cable leads to multiple reflections of the Johnson noise voltage waves and changes the original, flat Johnson noise temperature spectrum of the load to one that has frequency-dependent resonances. Knowing precisely how the Johnson noise temperature spectrum of the load changes at the input of the first amplifier when a cable is introduced is vital for developing an accurate absolute calibration method.

Multiple reflections of the Johnson noise voltage that occur in the cable are due to impedance mismatches at the cable-amplifier boundary and the load-cable boundary. These multiple reflections combine to modify the original Johnson noise temperature spectrum of the load. Since the amount of reflection at the cable-amplifier boundary depends on the impedance of the first amplifier, the net Johnson noise voltage wave that enters the input of the amplifier is modified by the amplifier itself. Therefore, breaking the circuit at the cable-amplifier boundary and attempting to directly measure the noise temperature spectrum of the load-cable combination with a Spectrum Analyzer (or indirectly with a Vector Network Analyzer) will not tell us how the Johnson noise temperature spectrum of the load will change due to the presence of the cable in our High-Z system. However, even though we cannot directly measure how the Johnson noise temperature spectrum of the load will be modified by the presence of the cable in our system, we can develop a mathematical model to describe the multiple reflections in the cable and then use that model to predict how the Johnson noise temperature spectrum will change.

The mathematical model that will help us understand how multiple reflections in the cable modify the original Johnson noise voltage of the load is called the Multiple Reflections (MR) model. We develop the mathematics for this model below, borrowing from standard techniques of multiple reflections developed in textbooks in microwave engineering and optics [11] [21]. The basic set up of this model is illustrated in Figure MR-1: we have a load impedance Z_L connected to our amplifier of impedance Z_A through a coaxial cable of length l with propagation constant β and impedance Z_o. We define an x-axis such that the origin is at the location of the amplifier and the load at $x = -l$.

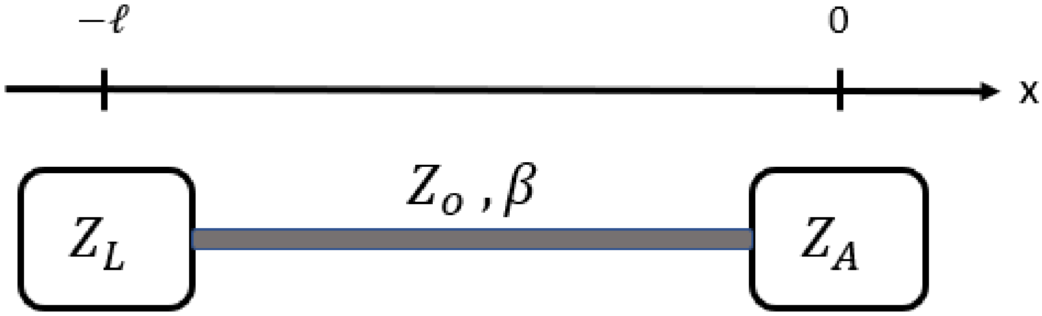

Figure 3.10: MR-1

The initial input voltage, before any reflections, is the Johnson noise of the load, which is given by the equation:

$$V_J = \sqrt{4kTR} \tag{3.15}$$

Where k is the Boltzmann constant, T is the temperature of the load resistor, and R is the resistance of the load.

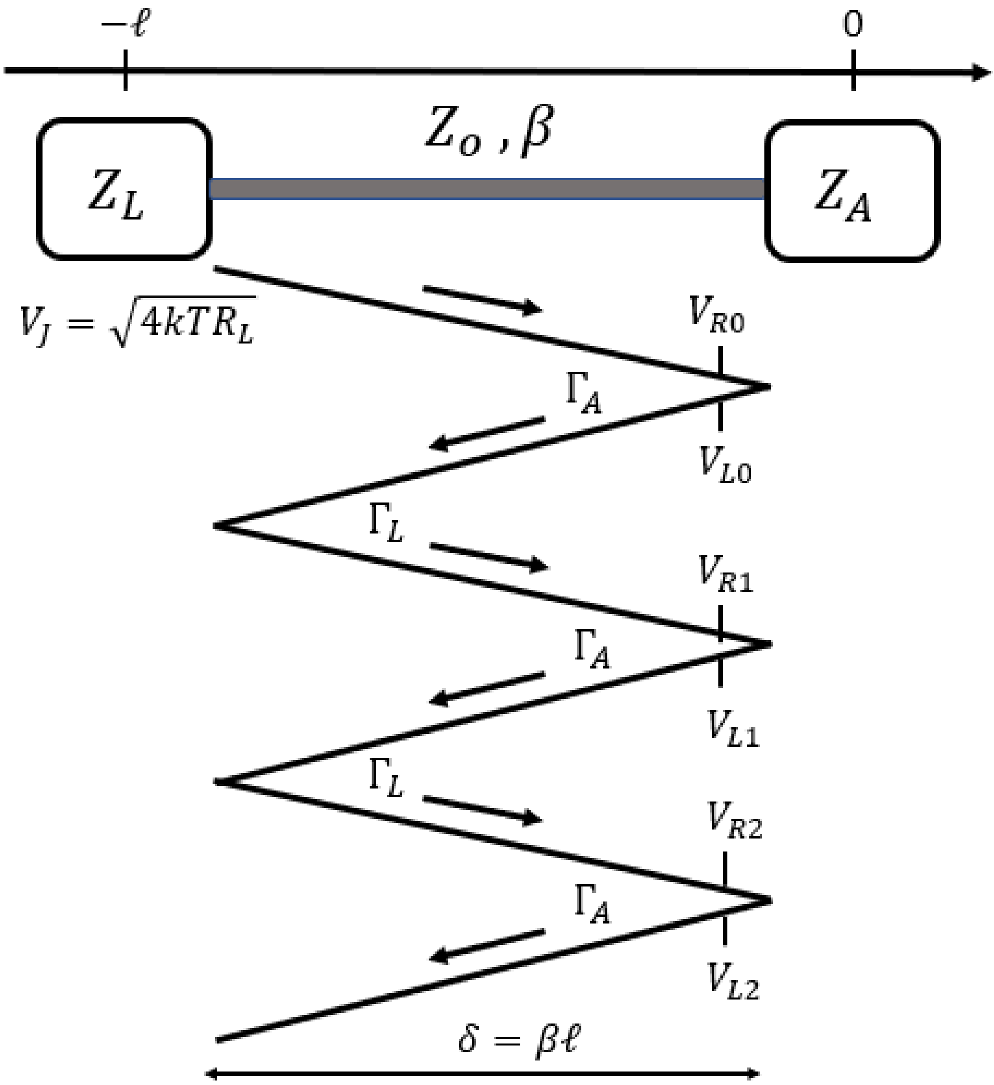

Figure 3.11: MR-2

Figure MR-2 schematically traces how the input voltage goes from Z_L to Z_A and back several times over. Note that while the diagram on Figure MR-2 looks 2D, the voltage signal bounces linearly between Z_L and Z_A. The first voltage (i.e. before any reflections) that arrives at the input of the amplifier is right travelling voltage wave, the amplitude of which is given by the basic voltage divider equation:

$$V_{R0} = \frac{Z_o}{Z_o + Z_L} * V_J \tag{3.16}$$

Part of this right travelling voltage wave reflects back towards the load impedance (Z_L) due to the impedance mismatch between the 50Ω cable and the high-impedance amplifier. We use the reflection coefficient Γ_A to tell us what fraction of the voltage is reflected at the amplifier:

$$V_{L0} = V_{R0} * \Gamma_A \tag{3.17}$$

The reflected voltage (V_{L0}) becomes a left travelling voltage wave that traverses the full length l of the cable until it reaches the load impedance (Z_L). If the impedance of the load differs from the 50Ω impedance of the cable, a part of V_{L0} reflects back toward the amplifier (Z_A) and travels a full length l of the cable back towards the amplifier. If the reflection coefficient of the load is Γ_L, the second right travelling voltage wave that arrives at the amplifier is given by:

$$V_{R1} = V_{R0} * (\Gamma_A \Gamma_L e^{i2\delta}) \tag{3.18}$$

The $e^{i2\delta}$ factor takes into account the change in phase that results from travelling twice the electrical path length of the cable. The electrical path length of the cable (δ) is given by:

$$\delta = \beta * l \tag{3.19}$$

$$\beta = \frac{2\pi f \sqrt{\epsilon_r \mu_r}}{c} \tag{3.20}$$

The n^{th} right travelling voltage wave arriving at the input of the amplifier is given by:

$$V_{Rn} = V_{R0} * (\Gamma_A \Gamma_L e^{i2\delta})^n \tag{3.21}$$

The sum of all the right travelling voltage waves at the input of the amplifier is:

$$V_{RT} = V_{R0} + V_{R0} * (\Gamma_A \Gamma_L e^{i2\delta}) + \cdots + V_{R0} * (\Gamma_A \Gamma_L e^{i2\delta})^n \tag{3.22}$$

The right travelling voltage waves are not the only voltage waves present at the input of the amplifier. The left travelling voltage waves at the input of the amplifier also contribute to the total voltage signal registered by the amplifier. The n^{th} left travelling voltage wave at the input of the amplifier is given by:

$$V_{Ln} = V_{R0}\Gamma_A * (\Gamma_A \Gamma_L e^{i2\delta})^n \tag{3.23}$$

The sum of all the left travelling voltage waves at the input of the amplifier is:

$$V_{LT} = V_{L0} + \cdots + V_{R0}\Gamma_A * (\Gamma_A \Gamma_L e^{i2\delta})^n \tag{3.24}$$

Note that the equations for the total right (V_{RT}) and left (V_{LT}) travelling voltage waves follow the basic format of the geometric series:

$$\sum_{n=0}^{\infty} V_o r^n = \frac{V_o}{1-r} \tag{3.25}$$

In the equations for both V_{RT} and V_{LT}, the common ratio between adjacent terms $r = \Gamma_A \Gamma_L * e^{i2\delta}$. The coefficient V_o for the right travelling wave is V_{R0} and for the left travelling wave is $V_{R0}\Gamma_A$. Therefore, the total right travelling wave and left travelling wave can be reduced to:

$$V_{RT} = \frac{V_{Ro}}{1 - \Gamma_A \Gamma_L e^{i2\delta}} \tag{3.26}$$

$$V_{LT} = \frac{V_{Ro}\Gamma_A}{1 - \Gamma_A \Gamma_L e^{i2\delta}} \tag{3.27}$$

The total voltage at the amplifier's input (V_T) will be the sum of ALL the voltages as $n \to \infty$:

$$\begin{aligned} V_T &= V_{RT} + V_{LT} \\ &= \frac{V_{Ro}}{1 - \Gamma_A \Gamma_L e^{i2\delta}} + \frac{V_{Ro}\Gamma_A}{1 - \Gamma_A \Gamma_L e^{i2\delta}} \\ &= V_{Ro}(1 + \Gamma_A)\left(\frac{1}{1 - \Gamma_A \Gamma_L e^{i2\delta}}\right) \\ &= V_J \left(\frac{Z_o}{Z_o + Z_L}\right)(1 + \Gamma_A)\left(\frac{1}{1 - \Gamma_A \Gamma_L e^{i2\delta}}\right) \end{aligned} \tag{3.28}$$

In our calibration of the High-Z system, we typically work with noise temperature, which is proportional to the magnitude square of the voltage. Therefore, we must take the magnitude square of both sides in equation (3.28). The equation for the magnitude square of the total voltage received at the input of the LNA is thus:

$$|V_T|^2 = |V_J|^2 \left(\left| \frac{Z_o}{Z_o + Z_L} \right|^2 |1 + \Gamma_A|^2 \left| \frac{1}{1 - \Gamma_A \Gamma_L e^{i2\delta}} \right|^2 \right) \tag{3.29}$$

To convert equation (3.29) to noise temperature, we need to divide by the factor $4kT(50\Omega)$. However, notice that dividing the magnitude square of the Johnson voltage $|V_J|^2$ by the factor $4kT(50\Omega)$ just gives us the Johnson noise temperature of the load T. Let us designate this original Johnson noise temperature of the load as T_L and the total amount of Johnson noise temperature received from the load at the input of the LNA as $T_{J,amp}$

$$|T_{J,amp}|^2 = |T_L|^2 \left(\left| \frac{Z_o}{Z_o + Z_L} \right|^2 |1 + \Gamma_A|^2 \left| \frac{1}{1 - \Gamma_A \Gamma_L e^{i2\delta}} \right|^2 \right) \tag{3.30}$$

In equation (3.30), we see that the original Johnson noise temperature of the load is changed by a multiplicative factor as a result of the multiple reflections. This multiplicative factor is generally a function of frequency and depends on the electrical path length δ, the impedance of the load and the cable (Z_L, Z_o) and the reflection coefficients of the load and the first LNA (Γ_L, Γ_A) (relative to 50Ω). Let's call this multiplicative factor G_{MR}, since functionally it is similar to a gain term. Then from equation (3.30), this multiplication factor G_{MR} is given by:

$$G_{MR} = \left(\left| \frac{Z_o}{Z_o + Z_L} \right|^2 |1 + \Gamma_A|^2 \left| \frac{1}{1 - \Gamma_A \Gamma_L e^{i2\delta} e^{-\tau}} \right|^2 \right) \tag{3.31}$$

3.2.2 Radiative Transfer

As the Johnson noise of a resistive load attached to a cable travels through the cable, the amplitude of the Johnson voltage diminishes with increasing frequency and cable length due to radiative transfer. Radiative transfer describes the process of how the intensity of electromagnetic radiation changes as it travels through a medium. The theory of radiative transfer presented here is a summary of the relevant processes relating to our experiment that are presented in a standard textbook in astrophysics by Rybicki and Lightman [24].

The intensity of electromagnetic radiation is reduced as it travels through a medium, such as a cable, due to absorption by the medium. However, the medium itself can spontaneously emit electromagnetic radiation which increases the intensity of the original beam of radiation. The amount of intensity that is added or lost in a beam of radiation as it travels through a medium can be expressed by the following two equations, where I refers to the beam intensity, j is the emission coefficient, α is the absorption coefficient, and ds is an incremental length of the medium:

$$dI = j ds \tag{3.32}$$

$$dI = -\alpha I ds \tag{3.33}$$

Notice that the amount of intensity lost from the beam due to absorption in equation (3.33) is proportional to the intensity of the beam. However, the amount of intensity added is independent of the beam intensity. This is because the emission coefficient j describes only spontaneous emission of the material in the medium. Stimulated emission, which does depend on the intensity of the beam, is actually part of the absorption coefficient α, which takes either positive or negative values depending on whether absorption or stimulated emission dominate in the medium.

The total differential change in the intensity of the beam is the sum of the differential gain and the differential loss in the intensity of the beam. The equation that expresses this is called the Radiative Transfer Equation:

$$\frac{dI}{ds} = j - \alpha I \tag{3.34}$$

Let us perform two changes of variables that will allow us to re-write the Radiative Transfer equation and interpret it in more physically relevant terms. Those two changes of variables are: 1) using the optical depth τ rather than the physical length s of the medium, and 2) using the Source Function S rather than the emission and absorption coefficients j and α.

$$d\tau \equiv \alpha ds \tag{3.35}$$

$$S \equiv \frac{j}{\alpha} \tag{3.36}$$

Optical depth τ is a dimensionless variable that describes how optically transparent or opaque the medium is to the photons passing through the medium in the beam. If the photons in the beam mostly pass through the medium, the medium is said to be "transparent" or "thin", and $\tau < 1$ in this scenario. If a large fraction of the photons in the beam are absorbed by the medium, the medium is said to be "opaque" or "thick", and $\tau > 1$. The Source Function S is the quantity the intensity I of the beam approaches in the limit of optically thick medium (as $\tau \to \infty$). The Source Function S has the same units as the intensity of the beam I.

By changing variables to optical depth τ and the Source Function S using equations (3.35) and (3.36), the Radiative Transfer Equation (3.34) can be written as:

$$\frac{dI}{d\tau} = -I + S \tag{3.37}$$

In equation (3.37), both I and S are functions of the optical depth τ. Equation (3.37) is a differential equation that can be solved by the integrating factor method, leading to the following solution to the Radiative Transfer Equation:

$$I(\tau) = I(0)e^{-\tau} + \int_0^{\tau} e^{-(\tau-\tau')} S(\tau')d\tau' \tag{3.38}$$

The first term in (3.38) describes the initial intensity $I(0)$ diminished by absorption in the medium. The second term in (3.38) describes the medium as an integrated source that is diminished by absorption. Let me explain the second term in more detail.

Consider the medium to be a long cylinder of length l and an optical depth $\tau' = 0$ at the beginning of the cylinder that extends to optical depth $\tau' = \tau = \alpha * l$ at the end of the cylinder, as depicted in figure X below. A differential element of this medium at optical depth τ' emits spontaneously at this location, but this spontaneous emission at τ' is diminished by absorption during the remaining optical depth $(\tau - \tau')$. The further this differential element is located from the end of the cylinder (that is, the further τ' is from the end), the more absorption the signal from the differential element experiences as it propagates through the remaining medium.

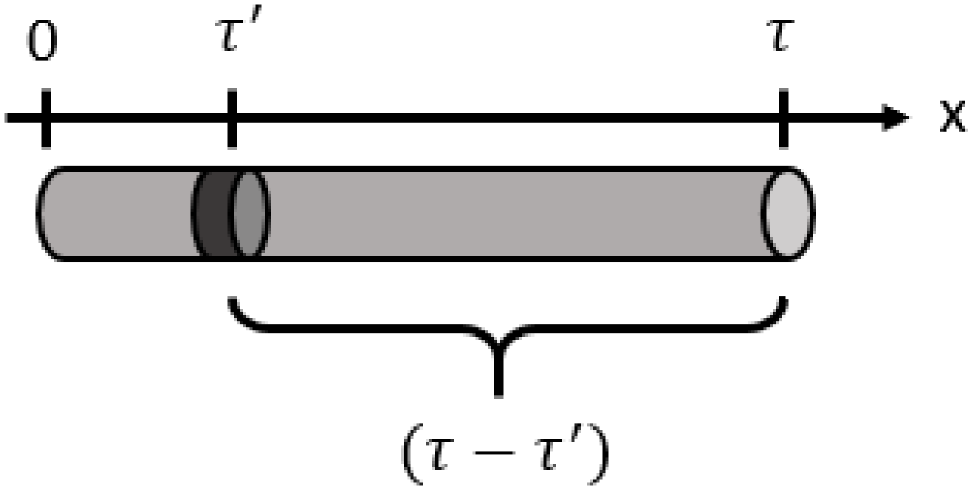

Figure 3.12: RT-1

If the Source Function S of the medium is constant, the solution to the Radiative Transfer Equation for the intensity of the beam simplifies to:

$$I(\tau) = I(0)e^{-\tau} + S(1 - e^{-\tau}) \tag{3.39}$$

From equation (3.39), it becomes clear that the beam intensity I approaches the Source Function S in the limit $\tau \to \infty$. Physically, this makes sense because the more optically dense the medium, or the longer the length of the medium, the more the beam intensity I will be dominated by the radiation from the medium.

Now let us consider what happens when the beam intensity I originates from matter in thermal equilibrium. In the case of thermal equilibrium, the intensity I is equal to the Planck function $B(T)$:

$$I = B(T) = \frac{2h\nu^3/c^2}{e^{h\nu/kT} - 1} \tag{3.40}$$

In the Rayleigh-Jeans limit ($h\nu << kT$), the exponential term in (3.40) can be Taylor expanded and the Planck function $B(T)$ simplified by keeping only the first order term in the expansion, yielding an equation for the beam intensity I:

$$I = B(T) = \frac{2\nu^2 k}{c^2}T \tag{3.41}$$

To connect this general discussion of Radiative Transfer for thermal sources to our specific discussion of resistive loads attached to cables and used as sources in our absolute calibration, we start by assuming that both the resistive loads and the cable are separately in thermal equilibrium. A resistive load acts as an external thermal source of intensity I, while the cable provides the optically thick medium through which that beam intensity travels. Since the resistive load is at thermal equilibrium and the temperature of the load is always much greater than $h\nu/k$ for all frequencies in our experiment, it's intensity I_{load} will be given by the Rayleigh-Jeans limit of the Planck function from equation (3.41):

$$I_{load} = \frac{2\nu^2 k}{c^2}T_{load} \tag{3.42}$$

The 50Ω co-axial cable, which acts as the optically thick medium, is also at thermal equilibrium and has a temperature that is always much greater than $h\nu/k$ for all frequencies in our experiment. The co-axial cable adds and subtracts to the intensity of the load's beam through it's own emission and absorption, and therefore the co-axial cable contributes to the Radiative Transfer through the source function S. For the co-axial cable, the Rayleigh-Jeans limit also applies, so the source function is given by equation (3.41):

$$S = \frac{2\nu^2 k}{c^2}T_{cable} \tag{3.43}$$

Using equations (3.42) and (3.43) for the intensity I and source function S in the Radiative Transfer Equation (3.37), we can write the Radiative Transfer Equation in terms of the load and cable temperatures:

$$\frac{dT_{load}}{d\tau} = -T_{load} + T_{cable} \tag{3.44}$$

Since the co-axial cable is homogeneous across it's length and maintains the same temperature at all points, the source function S is constant and we can use the solution of the Radiative Transfer Equation given by equation (3.39):

$$T_{load}(\tau) = T_{load}(0)e^{-\tau} + T_{cable}(1 - e^{-\tau}) \tag{3.45}$$

In equation (3.45), the temperature $T_{load}(\tau)$ corresponds to the cable-filtered Johnson noise temperature of the load, while $T_{load}(0)$ and T_{cable} correspond to the Johnson noise temperatures of the load and cable, respectively. Equation (3.45) describes how the Johnson noise temperature sensed at the input of the first LNA is modified from the original Johnson noise temperature of the load due to loss in the cable connecting the load to the LNA, as well as due to the cable's own Johnson noise emission and absorption. In the next section, I will discuss more about this loss and how to experimentally measure it in the lab using a VNA. One thing to note about equation (3.45) is it does not take into account the resonances that develop in the cable due to impedance mismatch. In section "MRRT Model", we will combine the model of Radiative Transfer for our load and cable, given by equation (3.45), with the Multiple Reflections model we developed earlier and given by equation (3.30).

3.2.3 Loss in the Cables

We will start the discussion about loss in the cables by first considering the ideal situation of a lossless cable. In the case of a terminated, lossless transmission line, the voltage signal on the line can be written as the sum of a forward-propagating wave and a reflected wave.

$$V(z) = V_o^+ e^{-i\beta z} + V_o^- e^{i\beta z} \tag{3.46}$$

In equation (3.46), the amplitudes of the forward-propagating wave and the reflected wave are given by V_o^+ and V_o^-, respectively. The propagation factor for each wave is given by the exponential term, with the negative exponential corresponding to the forward-propagating wave and the positive exponential for the reflected wave. The wavenumber, which will also be referred to as the propagation constant, is given by β for both the forward and reflected traveling waves. Since the wavenumber β is always real, the exponents in the propagation factors are always purely imaginary in lossless cables.

In practice, most cables do involve loss, even the low-loss cables we use in our absolute calibration. For shorter cables in our calibration, like the 13cm LMR-200, the loss is usually negligible. However, for longer cables, like the 244cm and the 487cm LMR-200, the loss is not negligible and can be easily seen in the Smith chart as an inward spiralling curve during a S21 measurement.

Loss in the cable can be incorporated into our model of a voltage wave travelling on a transmission line by replacing the real propagation constant β with a complex propagation constant γ. The real part of the complex propagation constant, called the attenuation constant α, will now describe the loss in the cable, while the imaginary part of the propagation constant will still describe the wavenumber. The equation for the complex propagation constant is given below. Note that he complex propagation constant can vary as a function of frequency.

$$\gamma = \alpha + i\beta \tag{3.47}$$

The voltage wave travelling on a transmission line can now be written for the case of a lossy cable:

$$\begin{aligned} V(z) &= V_o^+ e^{-\gamma z} + V_o^- e^{\gamma z} \\ V(z) &= \underbrace{V_o^+ e^{-\alpha z}}_{\text{amplitude}} * \underbrace{e^{-i\beta z}}_{\text{phase}} + \underbrace{V_o^- e^{-\alpha z}}_{\text{amplitude}} * \underbrace{e^{i\beta z}}_{\text{phase}} \end{aligned} \tag{3.48}$$

The voltage wave travelling on a lossy line has an amplitude that decays with distance z along the cable. This decay in amplitude is described by the factor $e^{-\alpha z}$. The phase of the forward and reflected voltage wave is still described by the factors $e^{-i\beta z}$ and $e^{i\beta z}$, the same as for the lossless case.

In the lab, it is possible to measure the attenuation factor $e^{-\alpha z}$ for any cable by performing an S21 measurement with a Vector Network Analyzer (VNA). After properly calibrating the VNA, and using matching attenuators on both ports of the VNA to minimize reflections, the cable is connected from port 1 to port 2 and a S21 measurement is performed. As an example, a plot of the S21 measurement for the 487cm LMR-200 co-axial cable is shown below on a Smith chart. We can see that the curve starts around the 0° point with a magnitude of 1.0, corresponding to full transmission of the signal without any attenuation. However, as we go clockwise around the circle, which corresponds to going down the length of the cable or, alternatively, seeing the attenuation of the transmission as a function of increasing frequency, the curve spirals inward from radius 1.0 to radii below 1.0. This can be interpreted as the attenuation of the transmission in voltage due to cable loss. From the plot it's clear that attenuation increases for longer cables and higher frequencies.

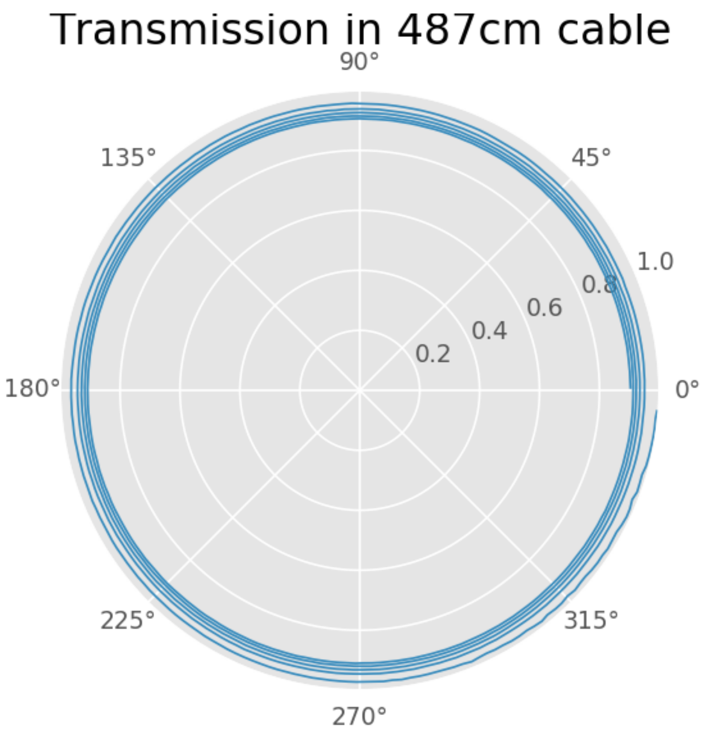

Figure 3.13: S21 Measurement for 487cm LMR-200 Co-axial Cable with the Vector Network Analyzer

Mathematically, the S21 measurement on the VNA gives us the normalized, complex voltage transmission of the signal:

$$T = e^{-\alpha z} e^{-i\beta z} \tag{3.49}$$

The attenuation of the signal due to cable loss is the magnitude of the complex voltage transmission:

$$|T| = e^{-\alpha z} \tag{3.50}$$

The attenuation of the signal in terms of power is given by the square of the magnitude of the complex voltage transmission:

$$\frac{P_z}{P_0} = |T|^2 = e^{-2\alpha z} \tag{3.51}$$

Therefore, in the absence of reflections, the transmitted power from a load to the LNA through a cable of length l is:

$$\frac{P_l}{P_0} = |T|^2 = e^{-2\alpha l} \tag{3.52}$$

We can connect the transmitted power to the optical depth discussed in the Radiative Transfer section. The term $e^{-\tau}$ in equation (3.45), which described how much the original intensity was diminished by absorption in the medium, can be used here to describe the attenuation of the power transmitted in the cable:

$$e^{-\tau} = \frac{P_l}{P_0} \tag{3.53}$$

Noting that $|T|^2$ represents the magnitude square of the transmitted voltage signal measured by the VNA, we can now specify how to experimentally measure the term $e^{-\tau}$ in equation (3.45):

$$e^{-\tau} = |T|^2 \tag{3.54}$$

3.2.4 MRRT Model

In section "Radiative Transfer", we derived equation (3.45), which describes the change in the Johnson noise temperature of the load as it travels through the medium of the cable. Recall that in equation (3.45), we considered how the change in the noise temperature results from loss in the cable, which is given by the term $e^{-\tau}$, and from the cable's own Johnson noise emission and absorption, given by the term $T_{cable}(1-e^{-\tau})$. One thing we did not consider, however, is how the multiple reflections in the cable, which we covered in the section "Multiple Reflections", would affect the radiative transfer solution equation (3.45). In this section we will combine the theory of multiple reflections that lead to cable resonances with the theory of radiative transfer inside the cable.

When a load is connected to the LNA through a co-axial cable of length l, multiple reflections in the cable modify the Johnson noise temperature that is sensed at the input of the LNA, creating resonances in the original Johnson noise temperature spectrum (see figure X). In equation (3.30), we saw that the original Johnson noise temperature of the load was changed by a multiplicative factor G_{MR}. Therefore, in the solution of the radiative transfer equation (3.45), when we consider how the Johnson noise temperature changes from the initial value at the load $T_{load}(0)$ to the final value at the end of the cable $T_{load}(\tau)$, we know that in addition to the loss of signal in the cable $e^{-\tau}$, the final value of the Johnson noise temperature will be different from the initial value by a factor of G_{MR}:.

$$T_{load}(\tau) = T_{load}(0)e^{-\tau}G_{MR} + T_{cable}(1 - e^{-\tau}) \tag{3.55}$$

In equation (3.55), the original signal $T_{load}(0)$ diminishes by a factor of $e^{-\tau}$ due to absorption by the cable. However, this assumes the signal travels through the cable only once. We know the signal actually bounces back and forth multiple times in the cable, so we need to take into account the loss in the multiple reflections. If we go back to the diagram in figure (3.11) and incorporate the loss due to cable absorption every time the signal bounces from one end of the cable to the other, we will end up with a slight modification of the multiplicative factor G_{MR}. The new multiplicative factor G_{MRRT}, which takes into account the cable losses for multiple reflections of the signal, is given by:

$$G_{MR} = \left(\left| \frac{Z_o}{Z_o + Z_L} \right|^2 |1 + \Gamma_A|^2 \left| \frac{1}{1 - \Gamma_A \Gamma_L e^{i2\delta} e^{-\tau}} \right|^2 \right) \tag{3.56}$$

Therefore, the equation that combines both the effects of the multiple reflections and the radiative transfer in the cable is given by:

$$T_{load}(\tau) = T_{load}(0)e^{-\tau} \left(\left| \frac{Z_o}{Z_o + Z_L} \right|^2 |1 + \Gamma_A|^2 \left| \frac{1}{1 - \Gamma_A \Gamma_L e^{i2\delta} e^{-\tau}} \right|^2 \right) + T_{cable}(1 - e^{-\tau}) \tag{3.57}$$

In equation (3.57), the original Johnson noise temperature of the load $T_{load}(0)$ can be determined for any load of impedance Z_L through the equation:

$$T_{load}(0) = \left(\frac{293}{50} \right) \mathrm{Re}(Z_L) \tag{3.58}$$

Equation (3.58) converts the impedance Z_L to the Johnson noise temperature referenced to the 50Ω load.

When taking spectra of loads connected to the LNA with co-axial cables, we will use equation (3.57) to model the source noise temperature T_s of the load-cable combination that is seen by the input of the LNA. Recall that the source noise temperature T_s is the input signal in our main calibration equation (3.4), from which we can calculate the noise temperature measured T_m by our spectrometer. Therefore, equation (3.57) is our model for the cable-filtered Johnson noise temperature of a given load, and we will call this model "Multiple Reflections Radiative Transfer" (MRRT) Model.

One may wonder if the MRRT model, given by equation (3.57), is equivalent to measuring the input impedance of the load-cable combination Z_{in} and then using a voltage divider to calculate the Johnson noise temperature at the input terminal of the LNA:

$$T_{load}(\tau) = T_{load}(0) \left(\left| \frac{Z_A}{Z_A + Z_{in}} \right|^2 \right) \tag{3.59}$$

Certainly, one could measure the input impedance of the load-cable combination Z_{in} quite easily with a Vector Network Analyzer, and the measurement would already take into account the effects of the cable, simplifying the whole process we discussed before. However, if we compare the predictions of both methods for one load-cable combination, we will see that they do not match each other. Below is a plot showing the predictions of both methods for the cable-filtered Johnson noise temperature of a 470Ω load and a 487cm cable. We see that using the input impedance with the voltage divider overestimates the predictions of the MRRT model in some places by almost twice as much! We will see later on, in the section "Elimination Method", that there is an independent way to test which method is correct. This independent test shows that the MRRT model is the correct model of the cable-filtered Johnson noise temperature of a given load.

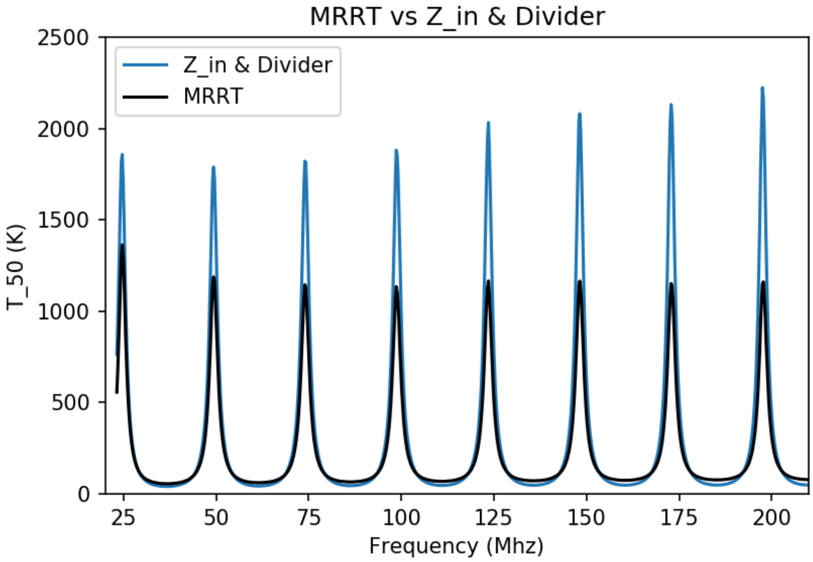

Figure 3.14: MRRT vs Input Impedance and Voltage Divider for 470 Ohm Load terminating a 487cm Cable

3.3 Noise of the 1st Amplifier

Determining the noise temperature of the first LNA for each specific antenna used in the High-Z system is crucial for the correct calibration of the system. The reason the noise temperature of the first LNA is so important to our calibration is due to the fact that it is similar in level to the noise temperature seen from the sky.

Even before deriving the exact noise temperature of the LNA for the case of each antenna, we were able to estimate the noise temperature of the LNA when an antenna was replaced with a 50Ω Johnson load. Using equation (3.13), we could plot the noise temperature spectrum for the first LNA for the case of a 50Ω Johnson load connected to the LNA by a 13cm co-axial cable. The noise temperature spectrum for the LNA in that case increased smoothly and monotonically from $450K \pm 10K$ at 25MHz to $485K \pm 15K$ at 200Mhz. If we compare this to the noise temperature spectra of the sky seen with our antennas at the Karoo site in July 2018, we find that the LNA noise temperature in the case of the 50Ω Johnson load is at a similar level to the noise temperature from the sky. The noise temperature of the sky varied from $300K$ at 25Mhz to $650K$ at 200Mhz for the 25cm antenna. For the 54cm antenna, the noise temperature ranged from $250K$ at 25Mhz to a resonance of $580K$ at 125MHz. For the tallest antenna (84cm), the noise temperature ranged from $520K$ at 25Mhz to a resonance of $970K$ at 85Mhz.

Since the noise temperature of the LNA and the temperature signal of the sky are comparable in level, the calibration of the system must verify that any features that could resemble the cosmological signal are not the result of the LNA but rather originate from the sky. The expected cosmological feature is estimated to be $20Mhz$ wide and $0-600mK$ deep, according to standard cosmological models and the EDGES findings [cite sources]. Therefore, the noise temperature spectrum of the first LNA in our system must either be determined to the precision level of half a Kelvin or confirmed to be smoothly varying without any features resembling the $20Mhz$ wide cosmological signal.

Of course, the noise temperature generated by the first LNA when an antenna is connected to the High-Z system is not the same as the noise temperature generated by the LNA when a 50Ω Johnson load is connected to the system. Therefore, we cannot just solve for T_{amp} in the calibration equations (3.8) and (3.9) for the room/cold temperature experiments with the 50Ω Johnson load at the end of a 13cm co-axial cable.

Experimentally determining the exact noise contribution of the first LNA for the frequency-varying impedance of each antenna used in the High-Z system is not an easy task due to several factors. One difficulty already discussed is the dependence of the LNA's current noise on the source impedance. In the "Absolute Calibration" section, we briefly introduced the two sources of noise for the LNA, their origin, and the equation that describe their magnitude. Recall that the two noise sources are voltage noise and current noise, with the first arising from the Johnson-Nyquist noise of the resistive components inside the amplifier and the latter arising from the amplifier's bias current flowing into the source. In the case of the current noise, the impedance of the source converts the amplifier's bias current into a voltage, which then adds as noise to the original signal coming from the sky at the input of the LNA. Equation (3.6) describes the mathematical form of the voltage and current noise components of the LNA.

Varying the impedance of the source changes the voltage generated due to the LNA's bias current in the source, and thus changes the current noise contribution of the LNA. Therefore, in our calibration of the system, we need to determine the correct current noise of the LNA when the source impedance corresponds to the frequency-varying impedance of each of our antennas, and not just a 50Ω Johnson load at the end of a 13cm co-axial cable.

Another difficulty in determining the exact noise temperature contribution from the first LNA is the potential correlation that might exist between the voltage noise and the current noise in the LNA. Recall that in equation (3.6) for the total noise temperature of the first LNA, we were able to write the total noise temperature as the sum of the voltage noise and current noise components of the LNA. However, this is not generally true. In the general case, the two noise sources are correlated and a complex correlation coefficient needs to be experimentally determined to quantify the correlation between the two noise sources.

Finally, one difficulty that is very specific to our particular LNA is the issue of the unusual reflection coefficient of the LNA. When we perform an S11 measurement of the A02 amplifier with the Vector Network Analyzer (VNA), we notice the magnitude of the amplifier's reflection coefficient Γ_A surpassing the maximum reflection level of 1.0 for frequencies greater than 100Mhz in the Smith Chart. Below is the Smith Chart representation of the reflection coefficient Γ_A for the amplifier A02. The reflection coefficient Γ is, in general, defined as the ratio of the reflected voltage wave V^- to the incoming voltage wave V^+:

$$\Gamma = \frac{V^-}{V^+} \tag{3.60}$$

Both the reflected voltage wave V^- and the incoming voltage wave V^+ are described by complex numbers, with an amplitude and a phase in the complex plane. Therefore, the reflection coefficient is also a complex number, described by both a real and an imaginary component. For all passive electrical components, the magnitude of the reflection coefficient Γ is always less than 1.0, meaning the reflected voltage wave is always smaller in amplitude than the incoming voltage wave. However, some active electrical components like certain amplifiers can have a reflection coefficient magnitude greater than 1.0, meaning the voltage wave that reflects from the input of those amplifiers is greater in amplitude than the original incoming voltage wave. This amplification of the original signal even before the signal passes through the gain stage of the amplifier can contribute to a significant error in interpreting the original signal, if not properly accounted for in the calibration equations of the amplifier.

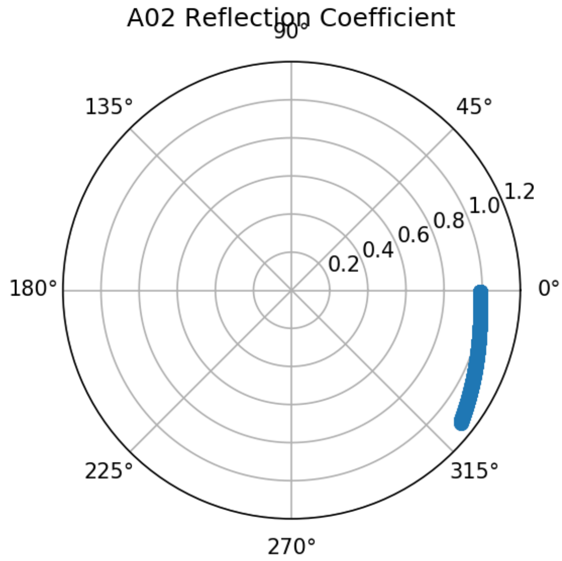

Figure 3.15: A02 Reflection Coefficient Γ_A

To address the difficulties in determining the exact noise characteristics of the first LNA, we have performed extensive testing of the LNA in the lab using a variety of experimental methods. In the sections below, I describe each method in detail and report the results obtained in each case. All the methods presented below focus on experimentally and independently deriving the bias current I of the LNA, flowing from the input of the LNA toward the source, as well as the voltage noise temperature T_{VN} of the LNA.

By focusing on experimentally deriving the bias current I at the input of the LNA rather than deriving the current noise term as a whole, we address the first concern we discussed about the current noise varying with the source impedance. The bias current I flowing from the LNA's input towards the source is independent of the source impedance, so we should obtain the same current experimentally no matter what source impedance we use in the experiment. If we can accurately determine this bias current I experimentally, then we can use the measurement of our antenna's impedance $Z_{antenna}$ to derive the correct current noise of the LNA for the case of our antenna.

One may ask, "Why not use the values of the bias current I and the voltage noise V_{VN} provided in the data sheet specifications of the first LNA?" The data sheet for the first LNA used in the High-Z system, which we termed "A02", does provide values and plots of the LNA's bias current and voltage noise per root bandwidth, but only in the range below 10kHz. The actual bias current and voltage noise of the amplifier (per root bandwidth) could deviate from the reported values in the frequency range of the High-Z system (25Mhz-200Mhz). In addition, the reported values on the data specifications sheet are not directly measured, but rather generated through computer simulations, and are thus not specific to the particular amplifier used but to the amplifier model in general.

In addition to deriving the LNA's bias current I and voltage noise temperature T_{VN} through a variety of independent experiments, we experimentally obtain a measure of the correlation between the two noise terms of the LNA using a technique first suggested by Rothe and Dahlke in their paper "Theory of Noisy Fourpoles" [23]. The technique for experimentally measuring the correlation between the two noise terms, as well as the results of the measurements, will be described in detail in the section "Rothe-Dahlke Method" below. These measurements will assuage our second concern about the potential correlation between the current noise and the voltage noise of the LNA and justify our treatment of the two noise sources as essentially uncorrelated for the purposes of our High-Z experiment.

Some of the experimental methods we employ to derive our LNA's bias current and voltage noise temperature involve replacing the antenna with Johnson loads of various resistance values and connecting them to the LNA by means of long co-axial cables. We have already discussed how Johnson loads of resistance values different from 50Ω will produce resonances in the cable when connected to the first LNA. We developed a theoretical model in the previous chapters, called the Multiple Reflections Radiative Transfer (MRRT) Model, to account for these resonances in the cable-filtered temperature spectrum of the Johnson loads. Since the MRRT Model uses measured values of the complex reflection coefficients of both the load and the LNA, it takes into account the unusual amplification of the original signal that may result from the LNA's reflection coefficient having a magnitude greater than 1.0 for frequencies above 100Mhz. The MRRT model will therefore allow us to compensate for this unusual property of our LNA and correctly interpret the original signal in our experiments. As a result, we will use the MRRT model for all experimental methods described below that involve Johnson loads connected to the LNA through long co-axial cables.

Before we begin discussing each method in detail, it should be noted that all methods presented below were developed and carried out in the lab by our group, with the exception of the Rothe-Dahlke method, which was already known in the literature. Rothe and Dahlke should also be credited with developing the model of the noisy amplifier we use in all our methods. This model was first described in their famous paper "Theory of Noisy Fourpoles" [23], and we dedicate the next section to discussing this model in detail.

3.3.1 Noise Model of the 1st Amplifier

Before we can begin to measure the noise characteristics of our LNA, we need to have a model of the noise in the LNA so that we know which noise characteristics we need to measure. Several models of amplifier noise exist in the literature, including the Thevenin's model [cite], the Bauer-Rothe model [cite], and the Rothe-Dahlke model of the noisy amplifier [23]. The model we choose to describe our LNA is the Rothe-Dahlke model, in part due to its simplicity and in part due to the straightforward physical interpretation of the noise sources involved in the model. We explore and elaborate on this model below.

The Rothe-Dahlke model starts by treating an amplifier as a noisy fourpole. The fourpole is comprised of the amplifier's two pairs of terminals, one pair at the input and one pair at the output, and the internal noise sources of the amplifier located in the middle of the two pairs. Figure 3.16 shows this noisy fourpole, with the numbers 1 and 2 corresponding to the input and output terminals, respectively. Each pair of terminals takes a current I and a voltage U, which can be different at the input and the output terminals. The internal noise sources in the middle are characterized by their own noise currents and noise voltages, which can be different at the input and the output terminals. Therefore, if one wants to determine the noise characteristics of this noisy fourpole, one needs to determine the noise currents at both terminals (i_1 and i_2) and the noise voltages at both terminals (u_1 and u_2).

Rather than determine the noise current and noise voltage at both the input and the output terminals separately, it is more convenient to bring all the internal noise sources of the LNA to the input terminal of the LNA, and to deal with the internal noise sources separately from the LNA. If we separate the internal noise sources from the LNA itself, then the LNA becomes a noise-free fourpole. The internal noise sources then form a noisy fourpole at the input of the actual LNA. Only one current i and one voltage u are needed to describe the internal noise sources in the noisy fourpole preceding the noise-free LNA. This current i and voltage u are depicted in figure 3.17, which shows a noise model of the LNA equivalent to the noisy fourpole in figure 3.16. Although we have reduced the number of internal noise sources by two in going to the equivalent circuit of figure 3.17, we still have the same number of unknowns to determine to understand the noise properties of the LNA. This is because the current i and the voltage u in figure 3.17 are generally correlated to each other, and the correlation coefficient is a complex number, so we need to determine both the real and the imaginary components of the correlation.

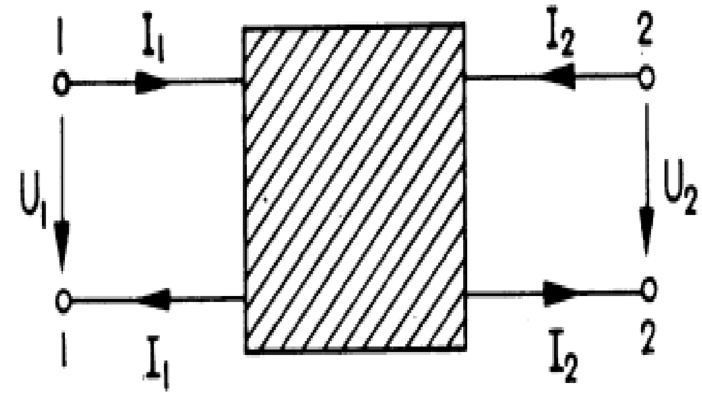

Figure 3.16: Noisy Fourpole

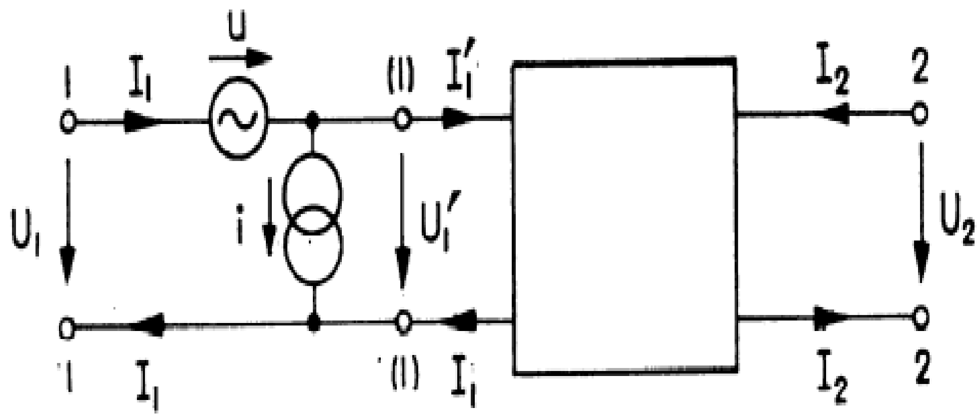

Figure 3.17: Noisy Fourpole Equivalent Circuit

The correlation between the noise current i and the noise voltage u can be analyzed more effectively by decomposing each into a part that is fully correlated to the other and a part that is completely uncorrelated to the other. The part of i and u that is completely uncorrelated to the other will be denoted by i_n and u_n, respectively. The part of i that is fully correlated to u will be proportional to u. The constant of proportionality needs to have units of admittance, so we introduce the correlated admittance Y_cor to represent this proportionality factor. Similarly, the part of u that is fully correlated to i will be proportional to i, with the constant of proportionality having units of impedance. Therefore, we can introduce the correlated impedance Z_cor to represent this constant of proportionality in the equation for u. When both i and u are decomposed into fully correlated and completely uncorrelated components, the equation for both take the form:

$$i = i_n + uY_{cor} \tag{3.61}$$

$$u = u_n + iZ_{cor} \tag{3.62}$$

The correlation between i and u can therefore be fully described by either the correlated admittance Y_{cor} or the correlated impedance Z_{cor}. Since the correlation is fully contained in either the Y_{cor} or Z_{cor} complex constant, the current i and voltage u in equations (3.61) and (3.62) are therefore uncorrelated to each other.

Since we decomposed both the noise current i and the noise voltage u into fully correlated and uncorrelated components, we need to modify our circuit model 3.17 to include the correlation constants Y_{cor} or Z_{cor}, in addition to the noise current i and noise voltage u. Figure 3.18 shows two equivalent circuit models for the noise of the amplifier. The circuit model on the left is more convenient when working with currents and the circuit model on the right is more convenient when working with voltages. However, both circuit models are equivalent to each other. In addition, both circuit models are equivalent to the circuit models in figures 3.17 and 3.16.

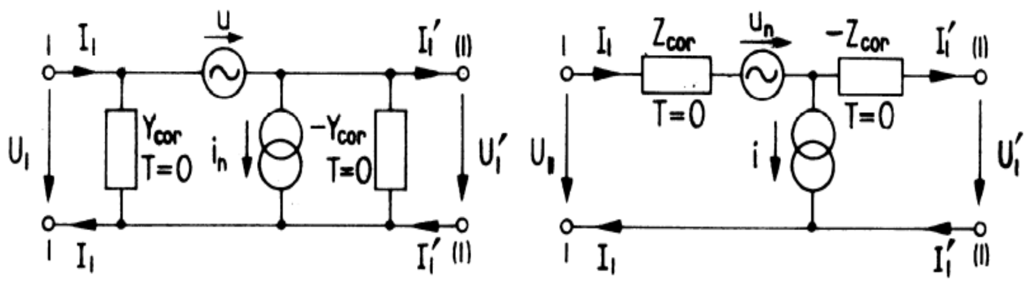

Figure 3.18: Correlation Between Current Noise and Voltage Noise

In both the left and right circuit models in figure 3.18, the correlation constants Y_{cor} and Z_{cor} were introduced symmetrically into their respective circuits. We should note that these correlation constants do not generate any noise on their own, so their intrinsic noise temperature is always zero. We can write equations for the current I_1 and voltage U_1 at the input of the noisy fourpole using Kirchhoff's laws:

$$\begin{aligned} I_1 &= I_1' + i_n + U_1 Y_{cor} - U_1' Y_{cor} \\ U_1 &= U_1' + u \end{aligned} \tag{3.63}$$

$$\begin{aligned} I_1 &= I_1' + i \\ U_1 &= U_1' + u_n + I_1 Z_{cor} - I_1' Z_{cor} \end{aligned} \tag{3.64}$$

Equations (3.63) correspond to the circuit model on the left in figure 3.18 and equations (3.64) correspond to the circuit model on the right in the same figure. The complex correlation constants Y_{cor} and Z_{cor} can be written in terms of their real and imaginary components:

$$Y_{cor} = G_{cor} + iB_{cor} \tag{3.65}$$

$$Z_{cor} = R_{cor} + iX_{cor} \tag{3.66}$$

In equation (3.65), G_{cor} is the correlated conductance and B_{cor} is the correlated susceptance. In equation (3.66), R_{cor} is the correlated resistance and X_{cor} is the correlated reactance.

Although we can choose to work with either of the two circuit models in figure 3.18, we have chosen to conduct our analysis with the circuit model on the right. Therefore, to fully describe the noise properties of any amplifier modelled by the circuit on the right in figure 3.18, we need to experimentally determine four quantities: the noise current i, the noise voltage u_n that is completely uncorrelated to i, the correlated resistance R_{cor}, and the correlated reactance X_{cor}.

Rothe and Dahlke propose a method for deriving these four quantities, which we will describe further in the section "Rothe and Dahlke Method". We have performed the method they describe (with some small variations) in our laboratory, and we report the spectra for the four quantities $(i, u_n, R_{cor}, X_{cor})$ we derived using their method in the same section.

3.3.2 Theoretical Estimates Of Noise

The first LNA of the High-Z system, which we refer to simply as A02, is manufactured by Texas Instrument and is identified by the model number LMH6629. Each manufactured LNA comes with a data specifications sheet that lists the expected values of the current noise and voltage noise of the LNA. Therefore, to get an estimate of the total noise of the LNA, we should first check the data specifications sheet for the LNA model number LMH6629 [26].

The data specifications sheet gives the following values for the LNA noise voltage v_n and noise current i_n:

$$v_n = 0.69nV/\sqrt{Hz} \tag{3.67}$$

$$i_n = 2.6pA/\sqrt{Hz} \tag{3.68}$$

If we convert the stated value of the noise voltage v_n into noise temperature T_{VN} by dividing by our usual conversion factor, we obtain:

$$T_{VN} = \frac{v_n^2}{4k(50\Omega)} = 172.5K \tag{3.69}$$

In addition to providing the expected values of the noise voltage and the noise current, the data specifications sheet for LMH6629 also includes a model for the noise in the LMH6629, which differs from the Rothe-Dahlke model we have discussed, but which is nevertheless useful to consider to get an estimate of the total amplifier noise. The circuit of the noise model, according to the data sheet of LMH6629, is provided below.

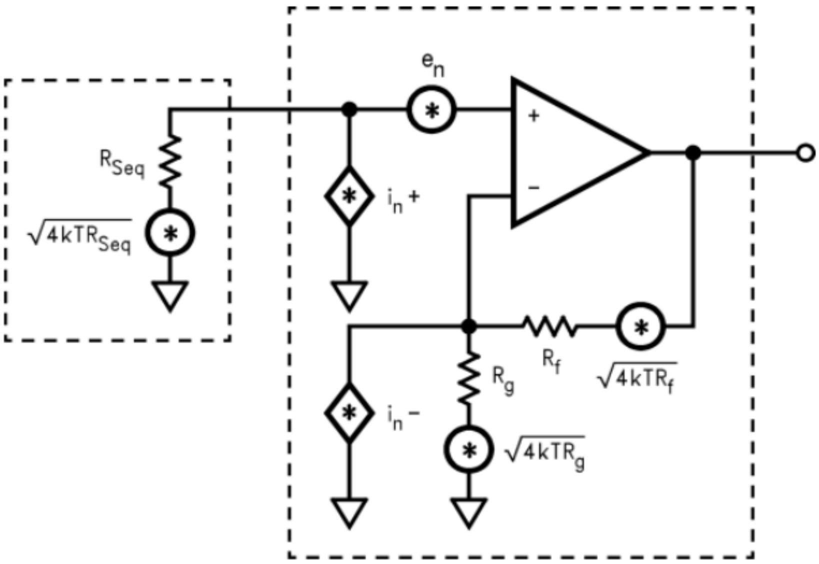

Figure 3.19: A02 Noise Model According to Data Specifications Sheet for LMH6629

In the model, we see the equivalent source resistance, depicted in the dashed box on the left, attached to the LNA, depicted by the dashed box on the right. The source resistance is modeled by a voltage source that generates Johnson noise $\sqrt{4kTR_{Seq}}$ and a series resistance R_{Seq}. The LNA is modeled by a parallel current noise source i_n^+ and a series voltage noise source e_n at the non-inverting input terminal (+), a parallel current noise source i_n^- at the inverting input terminal (-), and the Johnson noise of the feedback resistors $\sqrt{4kTR_g}$ and $\sqrt{4kTR_f}$.

The general equation for the total voltage noise related to an amplifier:

$$|V|^2 = |I_{n+}Z_s|^2 + |V_n|^2 + 4kT(R_f \mid\mid R_g) + (I_{n-}(R_f \mid\mid R_g))^2 \tag{3.70}$$

We will go through each term of the above equation in order:

1. The first term is the current noise due to the interaction of the output current noise of the positive terminal of the op-amp I_{n+} and the impedance of the source Z_s.

2. The second noise is the intrinsic noise of the op-amp V_n, which can be found on the op-amps data sheet.

3. The third term is the Johnson noise due to the feedback resistor network of the op amp. In particular, the effective resistor for the noise is the feedback resister R_f in parallel with the ground resistor R_g ($R4$ and $R3$ on Figure GN-1 respectively).

4. The fourth term is the current noise due to the interaction of the output current noise of the negative terminal of the op-amp I_{n-} and the effective resistance of the op-amp feedback network $R_f \mid\mid R_g$.

We can convert the general noise equation into a general noise equation in noise temperature units (in T_{50} units):

$$T_{amp} = \frac{(I_{n+}Z_s)^2}{4k(50\Omega)} + \frac{V_n^2}{4k(50\Omega)} + \frac{T(R_f \mid\mid R_g)}{(50\Omega)} + \frac{(I_{n-}(R_f \mid\mid R_g))^2}{4k(50\Omega)} \tag{3.71}$$

Where T is the actual temperature of the components (at room temperature $T = 293K$), R_{50} is a resistance of 50Ω, and $R_{eq} = R_f \mid\mid R_g$ is the equivalent resistance of the feedback network of the op-amp.

For our current set up, we have the values:

- The intrinsic noise of the op-amp is $V_n \approx 0.69\frac{nV}{\sqrt{Hz}}$
- The Johnson temperature of the feedback network is $T_{50,J,eq} \approx 240K$
- The input current is of $I_{n-} \approx 2.6pA$ which implies $T_{50,I_{n-}} = 4.1K$

Thus, the lowest estimate (best case scenario) of the temperature of the LNA is $T_{50,LNA} = 417K$.

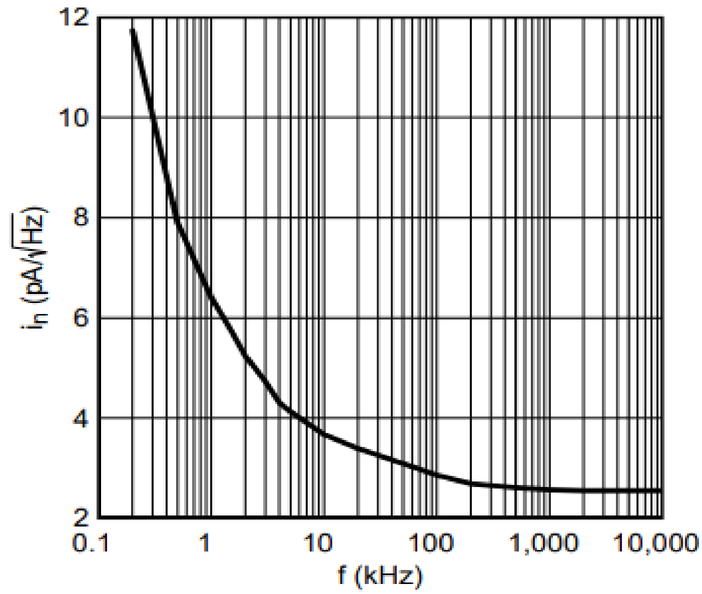

Figure 3.20: Current Spectrum According to A02 Specifications Sheet

3.3.3 Rothe-Dahlke Method

In section "Noise Model of the 1st Amplifier", we discussed how to characterize the noise properties of an amplifier using a model first developed by Rothe and Dahlke in their paper [23]. The authors of the paper presented several different but equivalent circuit models of the noisy amplifier, shown in figures 3.17 and 3.18. In those circuit models, the noisy components of the LNA are separated from the LNA itself and moved to the input of the LNA, so that they can be compared to the same reference plane as the source signal. At the input of the LNA, the noise sources are described by a parallel noise current source and a series voltage source, which are depicted in figure 3.17. This circuit model is later extended in figure 3.18 to include components that capture the correlation between those two noise sources. The correlations between the noise current i and noise voltage u can be described by either a correlated admittance Y_{cor} or a correlated impedance Z_{cor}. The circuit on the left in figure 3.18 corresponds to the admittance approach and the circuit on the right corresponds to the impedance approach. Both circuits are equivalent, and so either approach can fully describe all the noise characteristics of the amplifier.

In their paper, Rothe and Dahlke choose the admittance approach and devise an experimental method to derive the four unknowns in their model, including the noise current i, the noise voltage u, the correlated conductance G_{cor}, and the correlated susceptance B_{cor}. We have chosen rather the impedance approach, as it is more convenient for working with voltages. We use their experimental method to derive the four unknowns for the impedance circuit model shown on the right in figure 3.18. The four unknowns in our case are the noise current i, the noise voltage u, the correlated resistance R_{cor}, and the correlated reactance X_{cor}.

The method Rothe and Dahlke propose for determining the four unknowns that characterize all the noise properties of an amplifier is outlined in the steps below. We have modified the method presented in their paper to correspond to the impedance approach.

1. Attach sources of varying resistance and reactance to the input terminal of the circuit on the right in figure 3.18. The input terminal is between the points 11.

2. Plot the magnitude square of the total voltage measured at the terminal between the points (1)(1) as a function of the source reactance. The relationship should be parabolic.

3. Take the second derivative of the quadratic function in step 2 and divide by two to obtain the magnitude square of the noise current $|i|^2$.

4. Find the minimum of the parabola in step 2. The x-coordinate of the minimum corresponds to the negative of the correlated reactance X_{cor}.

5. Subtract the magnitude square of the source voltage from the minimum of the magnitude square of the total voltage (i.e. the y-coordinate of the minimum in step 4).

6. Plot the difference in step 5) as a function of the source resistance. This relationship should yield another parabolic relationship.

7. Find the minimum of the parabola in step 6. The x-coordinate of the minimum corresponds to the negative of the correlated resistance R_{cor}. The y-coordinate of the minimum corresponds to the magnitude square of the voltage noise $|u|^2$.

Let's first try to understand how the steps of the method outlined above relate to the noise model of the amplifier depicted by the circuit on the right in figure 3.18. If we attach a source of impedance $Z_s = R_s + iX_s$ to the input terminal of the noisy fourpole that represents the noisy part of our LNA, this source impedance will generate a voltage u_s that is uncorrelated to any of the noise components in the noisy fourpole. The open-circuit voltage at the input of the noise-free LNA, which is equal to the open-circuit voltage at the output of the noisy fourpole (between the points (1)(1)), can then be written as:

$$u_{tot} = u_s + u_n + i(Z_s + Z_{cor}) \tag{3.72}$$

In equation (3.72), the term u_n corresponds to the noise voltage of the LNA that is uncorrelated to the noise current i of the LNA. Since the correlation between the LNA's noise current and noise voltage is contained in the correlated impedance Z_{cor}, we will drop the subscript n from u_n and just refer to the uncorrelated noise voltage as the noise voltage of the LNA.

Since our system measures magnitude square voltage, we can take the magnitude square of both sides of equation (3.72). All the terms on the right side of equation (3.72) are uncorrelated, so the magnitude square of their sum is simply the sum of the magnitude square of each term:

$$\begin{aligned} |u_{tot}|^2 &= |u_s|^2 + |u|^2 + |i|^2 |Z_s + Z_{cor}|^2 \\ |u_{tot}|^2 &= |u_s|^2 + |u|^2 + |i|^2 \left[(R_s + R_{cor})^2 + (X_s + X_{cor})^2 \right] \end{aligned} \tag{3.73}$$

In equation (3.73), the magnitude square of the total voltage $|u_{tot}|^2$ is a quadratic function of the source reactance X_{cor}. The second derivative of this function with respect to the source reactance is just twice the magnitude square of the LNA's noise current:

$$\frac{d^2}{dX_s^2} \left(|u_{tot}|^2 \right) = 2|i|^2 \tag{3.74}$$

If we plot the magnitude square of the total voltage $|u_{tot}|^2$ as a function of the source reactance X_{cor}, we obtain a parabola with a minimum at $X_s = -X_{cor}$:

$$\text{vertex} : X_s = -X_{cor} \tag{3.75}$$

At the minimum of the parabola, the reactance part of equation (3.73) disappears and the magnitude square of the total voltage is at a minimum:

$$(|u_{tot}|^2)_{min} = |u_s|^2 + |u|^2 + |i|^2(R_s + R_{cor})^2 \tag{3.76}$$

This minimum of the magnitude square of the total voltage becomes a quadratic function of the source resistance R_s. If we subtract the source voltage term $|u_s|^2$ from the left hand side of equation (3.76), then the resulting quadratic equation can be plotted as a parabola with the y-axis corresponding to the difference $(|u_{tot}|^2)_{min} - |u_s|^2$ and the x-axis corresponding to the source resistance R_s. This parabola, which I will refer to as the "second parabola", has a vertex at $R_s = -R_{cor}$.

$$\text{vertex of second parabola} : R_s = -R_{cor} \tag{3.77}$$

The y-coordinate of this vertex (of the second parabola) is equal to the magnitude square of the LNA's voltage noise $|u|^2$:

$$\left((|u_{tot}|^2)_{min} - |u_s|^2\right)_{min} = |u|^2 \tag{3.78}$$

Note that in equation (3.78), the outer minimum refers to the minimum of the second parabola while the inner minimum refers to the first parabola. Also note in equation (3.77), the source resistance and the correlated resistance are related through a minus sign. Since resistance values are not typically negative, both R_s and R_{cor} should be positive. This means that we can only plot source resistance R_s values that are positive and will need to extrapolate to the vertex of the second parabola, which will be located in the negative range of R_s in order for R_{cor} to be positive. This extrapolation could introduce further errors and make the location of the vertex of the second parabola less reliable than first parabola.

Now that we have understood the theory behind Rothe-Dahlke's method for obtaining the four unknown quantities (i, u, X_{cor}, R_{cor}) corresponding to the circuit on the right in figure 3.18, we will explain how we enacted their method in practice in our laboratory and the results we obtained using their method.

For the sources in Rothe-Dahlke's method, we chose a set of different resistances attached to co-axial cables of varying lengths. When resistive loads are attached to co-axial cables, the output impedance of their combination is a complex impedance, with the resistive and reactive components varying with frequency. Co-axial cables, therefore, allow us to vary the reactance of the source without introducing capacitors or inductors into our small circuit on our terminating load. Co-axial cables also hold an advantage over using individual resistors, capacitors, and inductors due to the fact that they allow us to survey a greater area of the complex space of the source impedance than the individual components by themselves.

The set of loads we use have the following resistance values: 1300Ω, 470Ω, 390Ω, 300Ω, 270Ω, 100Ω, and 50Ω. The set of low-loss, LMR-200 co-axial cables we use include the following lengths: 1024cm, 487cm, 244cm, 124cm, 63cm, and 13cm. For each load-cable combination, the output impedance is measured by the portable Vector Network Analyzer (VNA) and used as the complex source impedance Z_s in our analysis.

We measure the magnitude square of the total voltage with our High-Z spectrometer and then divide by the system gain G to convert it to the magnitude square of the total voltage $|u_{tot}|^2$ at the input of the noise-free LNA:

$$|u_{tot}|^2 = \frac{(|u_{tot}|^2)_{measured}}{G} \tag{3.79}$$

Notice that equation (3.79) is very similar to our main calibration equation (3.4) that converts the measured noise temperature T_m to the source noise temperature T_s at the input of the LNA. However, instead of writing equation (3.4) in terms of the noise temperature, we have written it in terms of the magnitude square voltage. Recall that the noise temperature is proportional to the magnitude square voltage by a constant factor of $4k(50\Omega)$.

Also notice that in equation (3.79), we do not subtract the magnitude square voltage corresponding to the amplifier noise temperature T_{amp}, as is done in equation (3.4) when converting measured values to source values. The reason has to do with the reference plane for the total magnitude square voltage $|u_{tot}|^2$. Now that we have a noise model of the LNA, where the noise components have been separated from the LNA and moved up front to the input of the noise-free LNA, we should be more clear about the reference plane for the source noise temperature T_s in equation (3.4). In our noise model of the LNA, the source noise temperature T_s refers to the input of the noisy fourpole prior to the noise-free LNA. However, the total magnitude square voltage $|u_{tot}|^2$ refers to the input of the noise-free LNA. Therefore, we cannot subtract the magnitude square voltage corresponding to the amplifier noise temperature T_{amp} because doing so would result in our $|u_{tot}|^2$ not being referenced to the correct point in our circuit. In addition, the amplifier noise term is exactly the term we are attempting to explore and analyze with our method, so it makes no sense to subtract it away.

Now that we have explained the type of sources we use in our experiment and how we obtain $|u_{tot}|^2$, we show the results obtained after carrying out the procedure outlined by Rothe-Dahlke's method. Our results are shown in the four plots below. Each plot shows one of the four quantities (i, u, X_{cor}, R_{cor}) characterizing the noise of the LNA as a function of frequency, in the frequency band of our experiment. The first plot shows the noise current i of our first LNA, which we refer to as "A02", as a function of frequency. Contrary to expectation, the plot does not show one constant value of the noise current as a function of frequency. The value of the noise current seems to vary primarily between $2pA/\sqrt{Hz}$ and $10pA/\sqrt{Hz}$, with an average value of approximately $5pA/\sqrt{Hz}$. The variations in the noise current spectrum do not appear random, but seem to contain a periodic structure. This periodic structure manifests as regions of smooth variation of the current approximately every 25Mhz, with discrete spikes of the current between the smooth regions. In addition to the smooth regions of current every 25Mhz, there also seems to be a resonance pattern that appears over regions of 50Mhz (in the 50Mhz-100Mhz region of the spectrum) and over regions of 175Mhz (in the 100Mhz-175Mhz region of the spectrum).

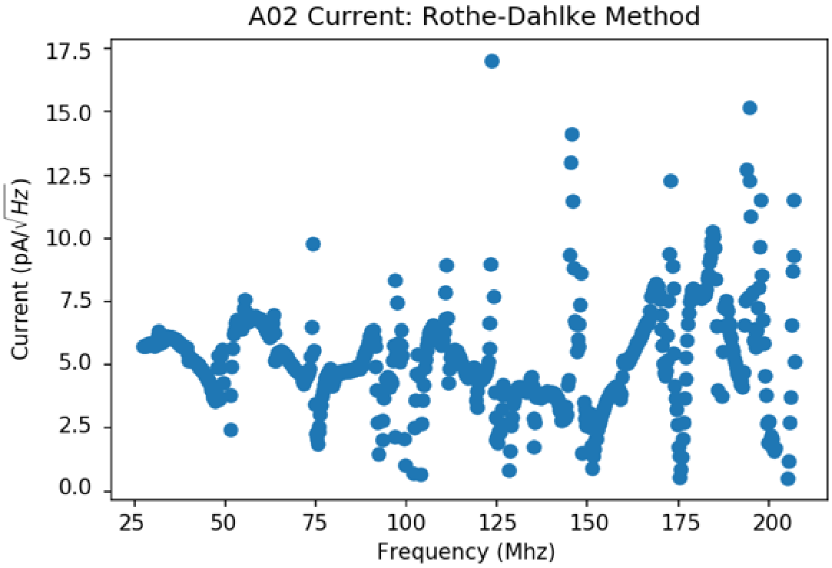

Figure 3.21: A02 Current Spectrum According to Rothe-Dahlke Method

We would be mistaken to assume that this periodic structure that appears in integer multiples of 25Mhz is a result of the actual noise current i varying with frequency. The more likely reason for the periodic structure is the cable resonances we discussed in the previous sections (see "Absolute Calibration", "Multiple Reflections", and "MRRT Model"). Recall from those discussions that when a load is connected to the LNA through a co-axial cable, resonances can form inside the cable from impedance mismatches at both boundaries of the cable. The width of these resonances in frequency space is inversely proportional to the length of the cables. Therefore, if we double the length of the cable, we will see twice as many standing waves in our spectrum. If we look at the lengths of the cables used in this experiment, they all differ by a factor of two (except the 13cm cable, which has a resonance outside our frequency range). Therefore, the number of resonance peaks each cable will create in the spectrum will be an integer multiple of the others.

Indeed, if we look at the noise temperature spectrum for a 100Ω load connected to the LNA by the cables in our list, we see resonance peaks that appear in the spectrum as integer multiples of each other. The plot below shows these resonance peaks for the list of cables in our experiment. Immediately from looking at these resonances, we see the same periodic structure as we saw in the LNA noise current i spectrum. At the locations in frequency where the noise current i spikes, we can see resonance peaks from two or more cables. Resonance peaks from some cables seem to be stronger than other cables. In particular, the resonance peaks that occur every 25Mhz, 50Mhz, and 75Mhz appear stronger than those occurring every 8Mhz. This could explain why the noise current i of our LNA seemed to contain structure that occured every 25Mhz, 50Mhz, and 75Mhz.

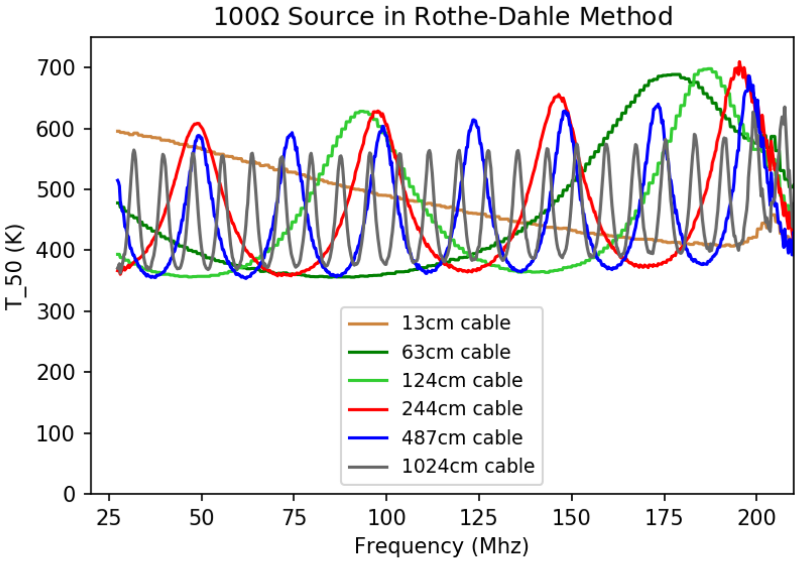

Figure 3.22: 100Ω Source in Rothe-Dahle Method

Since the resonance peaks depend only on the length of the cables and not on the impedance of the source, resonance peaks for the other loads will appear at the same frequencies and will contribute to the same periodic structure in the spectrum as the 100Ω source shown here. Therefore, it is very likely that the periodic structure we are seeing in the noise current i spectrum is a result of the cable resonances.

If we take a look at the plot of the next quantity characterizing the noise of our LNA, we can see the same periodic structure as in the case of the noise current spectrum. The plot of the correlated reactance X_{cor} as a function of frequency is shown below, for the frequency band of our experiment. Just like in the noise current spectrum, this periodic structure in the spectrum of the correlated reactance is an effect of the cable resonances and not the result of the inherent noise properties of the LNA.

Despite the artificial structure coming from the cable resonances, the plot of the correlated reactance shows a very important result. In the regions between the large spikes in the data, which we know correspond to cable resonance peaks, the correlated reactance seems to vary about the $X_{cor} = 0$ axis symmetrically in each 25Mhz smooth region. Of course, the symmetry about the $X_{cor} = 0$ axis is not perfect, and some regions average out slightly higher than $X_{cor} = 0$ and some regions slightly lower. Nevertheless, the correlated reactance seems to be averaging out close to zero across our system's frequency band. In fact, if we remove the spikes in the correlated reactance plot and average out the remaining data over every 25Mhz, we will get a plot of the correlated reactance X_{cor} that is much closer to zero than the original. This plot of the correlated reactance averaged over 25Mhz intervals is shown below.

Are we justified in averaging out the correlated reactance over 25Mhz intervals? Since the correlated reactance varies in a similar fashion periodically, every 25Mhz or integer multiples of 25Mhz, the variations in the smooth regions are most likely the result of the effects of cable resonances, just as in the case of the current noise spectrum. Therefore, the smoothly varying structure in each 25Mhz interval likely does not represent the actual correlated reactance of the amplifier and can be ignored. However, the average value of the variations in each 25Mhz interval can give us an approximate measure of the actual correlated reactance of the amplifier. Therefore, yes, we are justified in averaging out the correlated reactance over 25Mhz intervals.

Looking at this averaged spectrum of the correlated reactance X_{cor}, we see that the correlated reactance is between -10Ω and -10Ω for frequencies below 125Mhz, and between -20Ω and -10Ω for frequencies above 125Mhz. When compared with the impedance of our antenna, the correlated reactance is smaller in magnitude by approximately a factor of 30. Therefore, the contribution the correlated reactance will make toward the noise temperature of the LNA will be smaller by a factor of approximately 900 than the contribution of the antenna impedance to the current noise of the LNA. If we then consider the voltage noise in addition to the current noise of the LNA, the contribution of the correlated reactance to the noise temperature of the LNA is virtually negligible. It is virtually negligible, but not completely negligible.

If we take the averaged spectrum of the correlated reactance X_{cor} and multiply it with an averaged spectrum of the noise current i, then take the magnitude square of the product and divide by $4k(50\Omega)$, we can see the noise temperature contribution of the correlated reactance to our High-Z system. The plot of this noise temperature contribution from the correlated reactance of the LNA is shown below. In this plot, we see that the noise temperature contribution is less than 300mK in frequency range 25-50Mhz and 75-125Mhz. However, the noise temperature contribution is between 1K and 1.5K for frequency range 50-75Mhz and 125-175Mhz. Since the cosmological absorption trough is predicted to be in the range 0-500mK, the correlated reactance X_{cor} of the LNA can be a significant factor in interpreting any detection of an absorption trough in the sky signal. Therefore, future work for this experiment should include devising more sensitive methods to determine the correlation between the noise sources in the LNA.

The variation in the noise temperature spectrum due to the correlated reactance could be a feature propagated from the effects of cable resonances. Recall that in addition to cable resonances over intervals of 25Mhz in our spectrum, there are resonances over intervals of 50Mhz and 75Mhz. These could cause the noise temperature spectrum due to the correlated reactance to swing to higher temperatures over intervals of 50Mhz and 75Mhz (as we can see in the plot in figure X). If this is so, we may be able to ignore those contributions to the spectrum that swing to 1K and higher, dismissing them as features of cable resonance. In this case, the contribution of the correlated reactance to the noise temperature spectrum of the LNA can be ignored if the amplitude of the cosmological feature is approximately 500mK, which is the size detected by the EDGES team. Therefore, we would still have the sensitivity to confirm or deny the observations of the EDGES team even if we neglect the noise temperature contribution due to the correlated reactance in our noise temperature of the LNA.

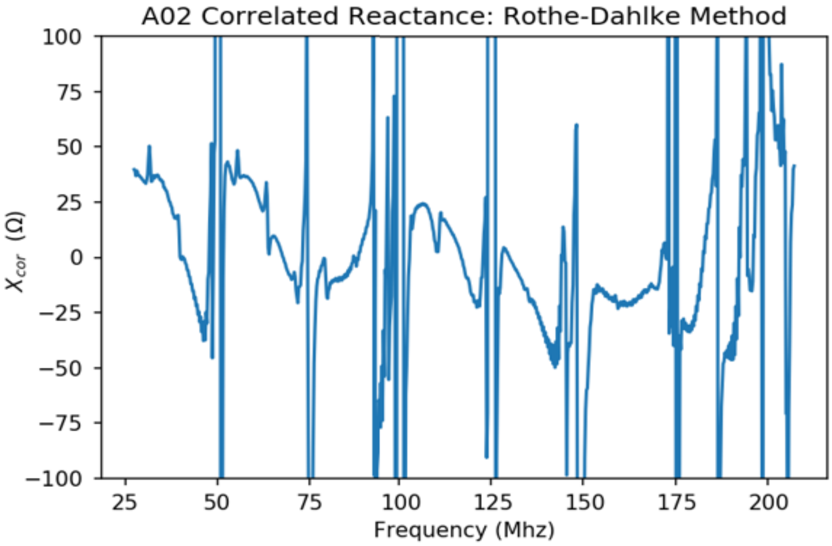

Figure 3.23: A02 Correlated Reactance According to Rothe-Dahlke Method

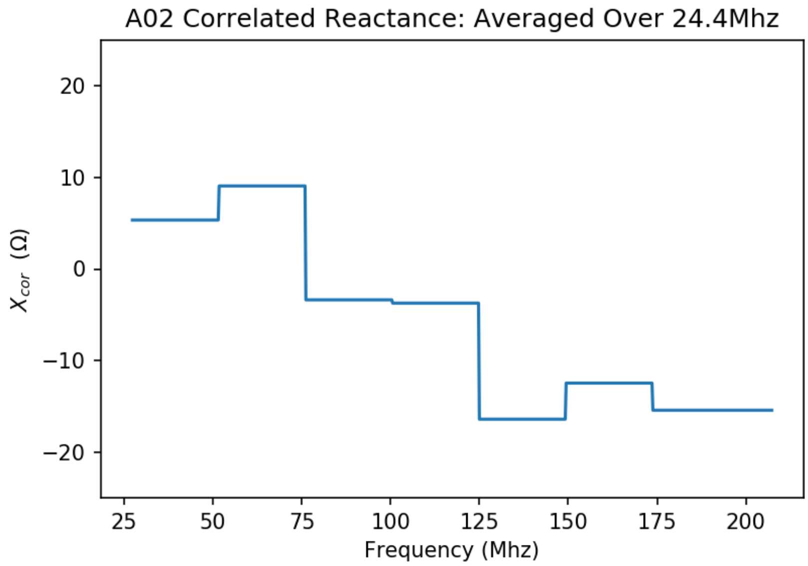

Figure 3.24: A02 Correlated Reactance Averaged Over a Period of 24.4Mhz

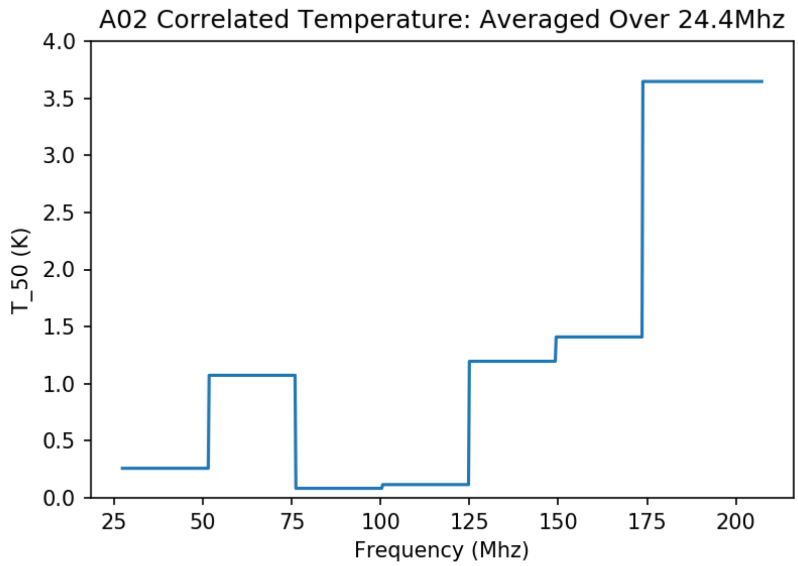

Figure 3.25: A02 Correlated Noise Temperature Averaged Over a Period of 24.4Mhz

Moving onto the next quantity characterizing the noise of our LNA, below we see the plot for the correlated resistance R_{cor} as a function of frequency. This plot contains spikes in the data which are even more frequent than the two previous plots. This is possibly due to the fact that the correlated resistance is obtained through two quadratic fits and is therefore less reliable due to propagation of error from each fit. Recall from the steps outlined for the Rothe-Dahlke method, both the correlated resistance R_{cor} and the magnitude square of the LNA noise voltage $|u|^2$ are derived from the quadratic fit to the plot of $((|u_{tot}|^2)_{min} - |u_s|^2)$ with respect to the source resistance, where $(|u_{tot}|^2)_{min}$ is the minimum of a parabola that is generated from the quadratic fit to the plot of $|u_{tot}|^2$ with respect to the source reactance (see the steps of the Rothe-Dahlke method to clarify, as this can be confusing). Since both the correlated resistance R_{cor} and the magnitude square of the LNA noise voltage $|u|^2$ are derived from two successive quadratic fits, we can expect greater errors in those plots than in the plots for the LNA noise current i and correlated reactance X_{cor}.

Indeed, if we look below at the results of the plot for the magnitude square of the LNA noise voltage $|u|^2$, where we have converted the voltage square units to noise temperature units, the average temperature of the voltage noise of the LNA is approximately 150K. In later experiments, however, we will determine the LNA voltage noise temperature to be $445K \pm 20K$. Estimates of the LNA voltage noise temperature from the later experiments are more accurate and agree with each other to within 10K, whereas the estimate from the Rothe-Dahlke method has an error of 66 percent compared with the later estimates.

One important thing to note about the plot of the correlated resistance R_{cor} is that the average value seems to be very close to zero. It is difficult to give a specific number for the average value as there are so many large spikes in the data, as well as frequent small spikes, that make the averaging process inconsistent and unreliable for this dataset. However, if we zoom in around the $R_{cor} = 0$ axis, a visual inspection confirms that the average level of R_{cor} seems to be approximately 0Ω. Since the average level of the correlated resistance R_{cor} is even smaller in magnitude than the average level of the correlated reactance X_{cor}, and we have argued that the contribution of the correlated reactance can be ignored to confirm or deny the EDGES results, then we can safely assume that the contribution of the correlated resistance can also be ignored.

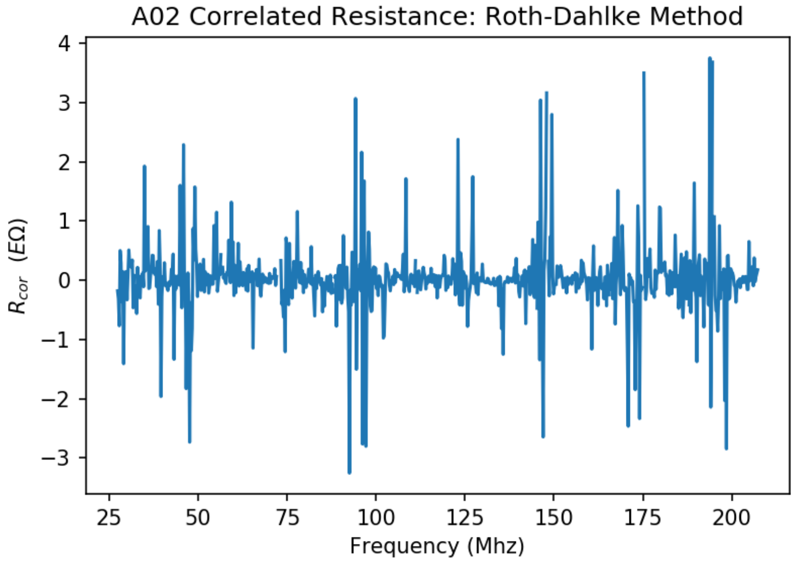

Figure 3.26: A02 Correlated Resistance According to Rothe-Dahlke Method

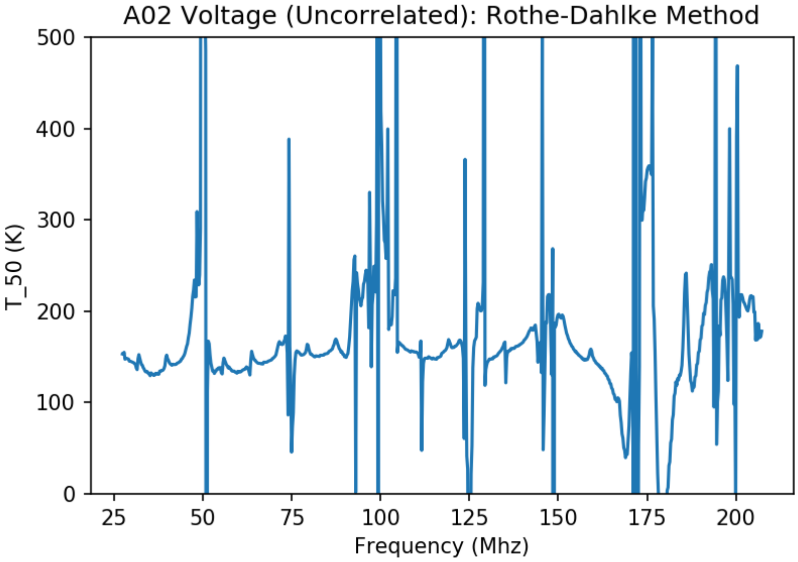

Figure 3.27: A02 Voltage Noise Temperature According to Rothe-Dahlke Method

To summarize the results of the Rothe-Dahlke method, the average noise current of the LNA is approximately $5pA/\sqrt{Hz}$ (with small variations about $5pA/\sqrt{Hz}$ when we average over intervals of 25Mhz), and the contribution to the LNA noise temperature from either the correlated reactance X_{cor} or the correlated resistance R_{cor} is negligible and can thus be ignored in our analysis of the total noise of the LNA. Since the complex correlation Z_{cor} between the noise current i and the noise voltage u is negligible, we are justified in writing the total noise temperature of the LNA as the sum of only the voltage noise term and the current noise term in equation (3.6).

3.3.4 Noise Figure Meter Experiments

Direct measurement of the noise contribution of the first amplifier is possible through the use of the Noise Figure Meter. The Noise Figure Meter is often used in RF engineering to measure the gain and the noise figure of a device such as an amplifier. The noise figure can be related to the noise contribution of the first amplifier through the analysis and calculations below.

The basic quantity describing the noise characteristics of an electrical device is called the noise factor. Noise factor is the measure of the degradation of the signal-to-noise ratio in a device and is defined mathematically as:

$$F = \frac{S_i/N_i}{S_o/N_o} \tag{3.80}$$

The numerator of the noise factor F is the ratio of the input signal to input noise, whereas the denominator is the ratio of the output signal to output noise. The noise factor F expressed in decibel units is the noise figure NF. The two are related mathematically through:

$$NF = 10 * log(F) \tag{3.81}$$

We can write the noise figure NF in terms of the signal-to-noise ratios to aid our analysis further:

$$NF = 10 * log\left(\frac{S_i/N_i}{S_o/N_o}\right) \tag{3.82}$$

A direct measurement of the noise figure NF and gain of our amplifier by the Noise Figure Meter in certain electrical combinations, along with a careful analysis of the input and output signals and noise in those combinations, will allow us to determine the full noise contribution of our amplifier. However, before measuring the noise figure and the gain of the amplifier with the Noise Figure Meter, the Noise Figure Meter must be calibrated. The calibration is accomplished internally within the Noise Figure Meter by connecting an ON/OFF noise source with a 50 ohm resistance directly to the Noise Figure Meter during the calibration stage.

After the calibration of the Noise Figure Meter is achieved, measurements of the noise figure and gain of various combinations can be performed. The first combination for which it is useful to measure the noise figure and gain is when the amplifier is inserted between the noise source and the Noise Figure Meter. See below for the schematic diagram. The noise source supplies the amplifier with an input noise power N_i equal to the Johnson noise of a 50 ohm resistor inside the noise source. Since the noise source produces only noise power, the input signal power to the amplifier is just the input noise power from the noise source.

$$S_i = N_i = 4kT \tag{3.83}$$

As the input noise power N_i travels from the output of the noise source to the amplifier and then through the amplifier, it experiences changes in power levels that may be frequency dependent. We call the total change in power from the output of the noise source to the output of the amplifier the total gain g_T. The output signal power S_o of the amplifier is then the input noise power N_i multiplied by the total gain g_T. The output noise power N_o, on the other hand, consists of two terms: 1) the input noise power N_i multiplied by the total gain g_T, and 2) the additional noise power N_A added to the signal by the amplifier itself. The equations below summarize this information:

$$S_o = g_T N_i \tag{3.84}$$

$$N_o = g_T N_i + N_A \tag{3.85}$$

Substituting equations (3.83),(3.84), and (3.85) into equation (3.82) for the noise figure NF, we get:

$$NF = 10 * log\left(\frac{g_T N_i + N_A}{g_T N_i}\right) \tag{3.86}$$

Solving for the noise power contribution N_A from the amplifier, we get:

$$N_A = g_T\left(10^{NF/10} - 1\right) N_i \tag{3.87}$$

It is important to note that, in the above equations, the noise power contribution N_A from the amplifier is referenced to the output of the amplifier. However, for the High-Z Calibration equations, we need the input-referred noise power contribution from the amplifier. To change the reference of this noise power from the output to the input, we simply divide by the amplifier gain stage g_A.

$$N_{A,in} = \frac{N_A}{g_A} \tag{3.88}$$

We can therefore write the equation for the input-referred noise power contribution from the amplifier by substituting (3.88) into (3.87) to get:

$$N_{A,in} = \frac{g_T}{g_A}\left(10^{NF/10} - 1\right) N_i \tag{3.89}$$

The total gain g_T is the same as the amplifier gain g_A if the noise source is connected directly to the input of the amplifier. However, if another electrical component is inserted between the output of the noise source and the input of the amplifier, the total gain g_T will be different from the amplifier gain g_A.

The noise power contribution of the amplifier stems from two different sources of noise within the amplifier: voltage noise and current noise. In discussing and understanding the voltage noise and the current noise of the amplifier, it is much easier to use voltage rather than power. To make the conversion from power to voltage, we use the equation:

$$P = \frac{|V|^2}{R} \tag{3.90}$$

We can take the R value to be 50 ohms, since that is our reference value. We use (3.90) to convert the noise power terms N_A and N_i in (3.89) to magnitude square voltage:

$$|V_{A,in}|^2 = \frac{g_T}{g_A}\left(10^{NF/10} - 1\right)|V_i|^2 \tag{3.91}$$

The total noise of the amplifier in magnitude square voltage is the magnitude square of the sum of all the noise voltages present in the amplifier. Recall from our discussion of the noise source model of our amplifier, there are two relevant noise sources present inside our amplifier - the voltage noise source and the current noise source. The voltage noise arises from the Johnson noise of all the resistive components in the amplifier, including the feedback resistors, while the current noise arises from the bias current of the amplifier passing through the source impedance. We will denote the voltage due to the voltage noise as V_{VN} and the voltage due to the current noise as V_{CN}. Since V_{CN} is simply the bias current I of the amplifier multiplied by the source impedance Z_{source}, we have the following general equation for the total input referred noise of our amplifier:

$$|V_{A,in}|^2 = |V_{VN} + IZ_{source}|^2 \tag{3.92}$$

We have good reasons to believe that the voltage noise of the amplifier is uncorrelated to the current noise of the amplifier. This allows us to write the magnitude square of the sum of the voltages as the sum of the magnitude square of each voltage:

$$|V_{A,in}|^2 = |V_{VN}|^2 + |IZ_{source}|^2 \tag{3.93}$$

We will refer to the magnitude square voltage of the voltage noise of the amplifier as the 'voltage noise term' and the magnitude square voltage of the current noise as the 'current noise term'. Since the voltage noise of the amplifier depends only on the Johnson noise of the resistors inside the amplifier, the voltage noise term stays the same regardless of what is connected to the amplifier. However, the current noise term does change depending on what is connected to the amplifier. If the source impedance Z_{source} seen at the amplifier is large, the current noise term will be large and potentially dominate the voltage noise term. On the other hand, if Z_{source} is small, the current noise term will also be small and the voltage noise term will probably dominate. Since the current noise term varies depending on what is connected to the amplifier, it is important for us to determine the bias current I of our amplifier experimentally, so that we can predict the correct current noise term for the antenna we plan to use in our experiment.

To determine the bias current of our amplifier experimentally, as well as the voltage noise term of our amplifier, we need to measure the noise figure and gain of at least two different electrical combinations on the Noise Figure Meter. The first combination is inserting the amplifier between the noise source and the Noise Figure Meter. We call this combination the 'amplifier-only' case, and the total gain g_T is the gain of the amplifier g_A. To understand the source impedance Z_{source} in this case, it is helpful to refer to the circuit diagram below, which shows the noise source connected directly to the amplifier input.

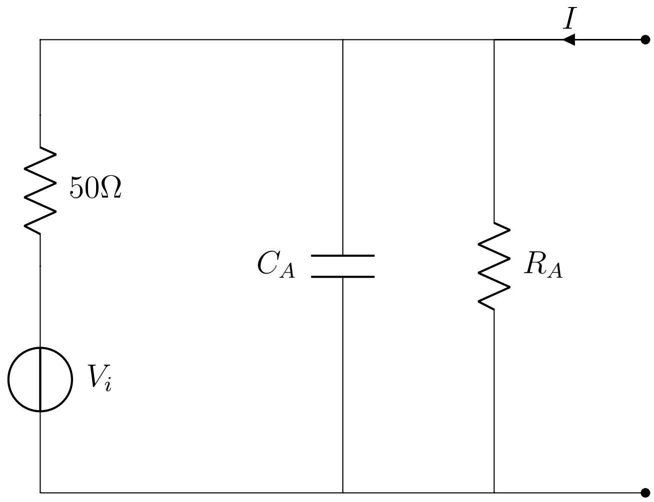

The noise source impedance consists of a resistance approximately equal to 50Ω, and this resistance provides the initial voltage V_i in the form of Johnson noise voltage. The amplifier input impedance Z_A is modelled by a parallel resistance R_A and a parallel capacitance C_A. The amplifier resistance R_A has a purely real impedance Z_{RA}, while the amplifier capacitance C_A has a purely imaginary reactive impedance Z_{CA}. The magnitude of the reactive impedance Z_{CA} is called the reactance X_{CA}. In general, reactance depends inversely on both the frequency and the capacitance.

$$Z_{RA} = R_A \tag{3.94}$$

$$Z_{CA} = iX_{CA} = i\frac{1}{2\pi f C_A} \tag{3.95}$$

Since the amplifier is modelled by a parallel resistance R_A and capacitance C_A, the input impedance of the amplifier Z_A has the following mathematical form:

$$Z_A = \frac{Z_{RA}Z_{CA}}{Z_{RA} + Z_{CA}} = \frac{iR_AX_{CA}}{R_A + iX_{CA}} \tag{3.96}$$

The bias current I coming from the amplifier chip is presented with a source impedance Z_{source} that is the parallel combination $Z_{NS||A}$ of the impedance of the noise source 50Ω and the input impedance of the amplifier Z_A. The amplifier impedance is included in the source impedance because the bias current I from the amplifier chip passes through the resistive and capacitative components of the amplifier input impedance in addition to passing through the impedance of the series capacitor and noise source. Both the noise source 50Ω and the input impedance of the amplifier Z_A are experimentally measured with our Vector Network Analyzer, and their parallel combination $Z_{NS||A}$ is determined computationally from these measurements. A plot of the magnitude of the source impedance in the amplifier-only case is shown below:

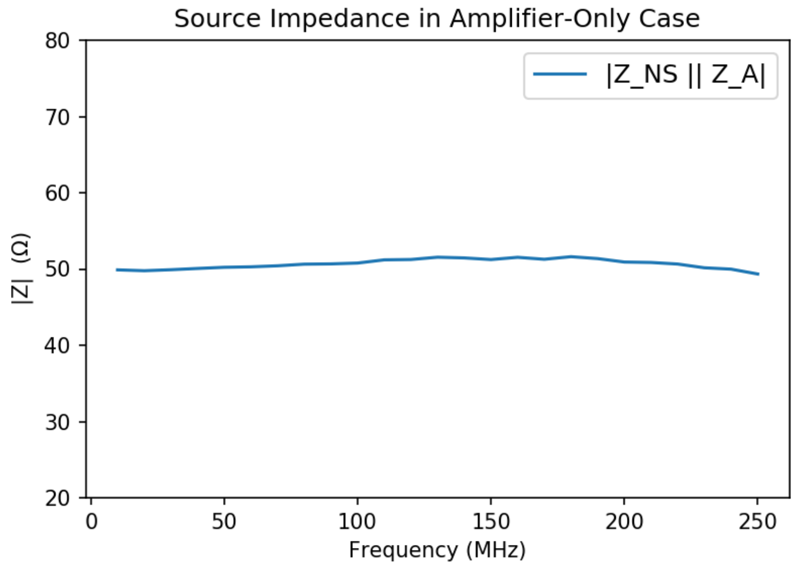

Figure 3.28: Source Impedance in Amplifier-Only Case

Measuring the noise figure NF and gain g_A in this 'amplifier-only' case on the Noise Figure Meter, and using $Z_{NS||A}$ as our source impedance, we can determine the total noise of the amplifier in this first combination using equations (3.91) and (3.93):

$$|V_{VN}|^2 + |IZ_{NS||A}|^2 = (10^{\frac{NF}{10}} - 1)|V_i|^2 \tag{3.97}$$

Since $Z_{NS||A}$ is relatively small, we expect the current noise term $|IZ_{NS||A}|^2$ in this combination to be relatively small and the voltage noise term $|V_{VN}|^2$ to dominate. However, we don't know exactly how much each noise term contributes from equation (3.97), because the first combination only tells us how much total noise (in magnitude squared voltage) the amplifier is contributing. To determine each noise term separately, we need a second equation to help us solve for the voltage noise term $|V_{VN}|^2$ and the bias current I in equation (3.97). This second equation will come from the noise figure and gain measurement of a second electrical combination on the Noise Figure Meter.

For the second electrical combination on the Noise Figure Meter, we want to vary the source impedance Z_{source} without introducing any new noise terms into our equation. The reason we want to vary the source impedance is because it is the only variable we can vary. The voltage noise term $|V_{VN}|^2$ and the bias current I are fixed and do not change in different electrical combinations. However, we must be careful about how we vary the source impedance Z_{source}. If we increase the source impedance Z_{source} by inserting a resistor between the noise source and the amplifier, the resistor would add a new noise term to our equation - Johnson noise due to its own resistance - in addition to increasing the current noise term. This would introduce a third unknown and we would need a third electrical combination to provide us a third equation to solve all the 3 unknown variables. However, if we increase the source impedance Z_{source} by inserting a series capacitor or a series inductor between the noise source and the amplifier, we could increase the current noise term without adding any additional noise terms to our equation. This is because the complex impedance of capacitors and inductors is purely imaginary, and imaginary impedances do not generate any Johnson noise.

The downside of using capacitors or inductors in our source impedance, though, is that the impedance of both capacitors and inductors varies with frequency. For capacitors, the impedance is inversely proportional to frequency, and for inductors, the impedance is directly proportional to frequency. Therefore, capacitors will generate a source impedance large enough to measure the current noise term accurately at lower frequencies, while inductors will measure the current noise term better at higher frequencies. To take advantage of the higher accuracy of the capacitor at lower frequencies and the inductor at higher frequencies, we can take noise figure and gain measurements for the second combination using first a series capacitor between the noise source and the amplifier, then a series inductor in place of the series capacitor, and finally combine the results for the bias current I from each case using an inverse-variance weighted average (IVWA).

I will discuss in detail the case of inserting the series capacitor between the noise source and the amplifier for the second electrical combination measured on the Noise Figure Meter, but the same discussion applies to the case of inserting the series inductor, if the impedance of the capacitor connected to noise source $Z_{C,NS}$ is replaced by the impedance of the inductor connected to noise source $Z_{L,NS}$. The total noise contribution of the amplifier when a series capacitor is inserted between the noise source and the amplifier is given by:

$$|V_{A,in}|^2 = |V_{VN}|^2 + |IZ_{C,NS||A}|^2 \tag{3.98}$$

We call this electrical combination measured on the Noise Figure Meter the 'series-capacitor case'. The voltage noise term $|V_{VN}|^2$ and the bias current I in the 'series-capacitor case' is the same as in the 'amplifier-only' case. However, inserting the capacitor in series between the noise source and the amplifier not only changes the noise contribution of the amplifier through the current noise term, but also the total gain g_T experienced by the input noise power. To see why the total gain will be modified, it is helpful to refer to the circuit diagram describing the main electrical components in the system, including the noise source impedance, capacitor in series, and the amplifier impedance.

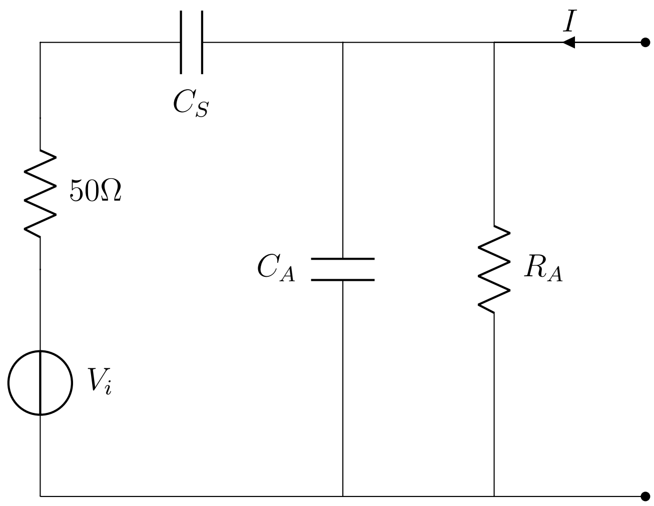

As in the previous case, the noise source is denoted by a resistance of 50Ω and a voltage source, which provides the initial Johnson noise voltage V_i. The noise source connects in series to a capacitor C_S, which connects in series to the amplifier. The amplifier input impedance Z_A is again modelled by a parallel resistance R_A and a parallel capacitance C_A.

As the initial Johnson noise voltage V_i passes through the impedance of the series capacitor, its voltage is reduced. According to the voltage divider equation, the initial voltage V_i drops to $V_{i,A}$ at the amplifier input:

$$V_{i,A} = \frac{Z_A}{Z_A + Z_{C,NS}} V_i \tag{3.99}$$

This translates into a change in *power* g_D even before the Johnson noise enters the amplifier. We will call this power gain g_D the 'voltage-divider gain':

$$g_D = \left| \frac{V_{i,A}}{V_{i,50}} \right|^2 = \left| \frac{Z_A}{Z_A + Z_{C,NS}} \right|^2 \tag{3.100}$$

The total gain g_T, which is the gain between the output of the noise source and the output of the amplifier, is the product of voltage divider gain g_D and the amplifier gain g_A:

$$g_T = g_D g_A \tag{3.101}$$

Therefore, whenever an electrical circuit element is inserted between the noise source and the amplifier, the total gain g_T changes because the voltage divider gain g_D changes. We can see this change when we measure and plot the total gain g_T for both the amplifier-only case and the series-capacitor case on the Noise Figure Meter. The plot below shows the total gain of the amplifier-only case in blue and the series-capacitor case in green and red. The series-capacitor case has two subcases: one for a series capacitor value of 5pF (green curve) and the other for a series capacitor value of 2.5pF (red curve).

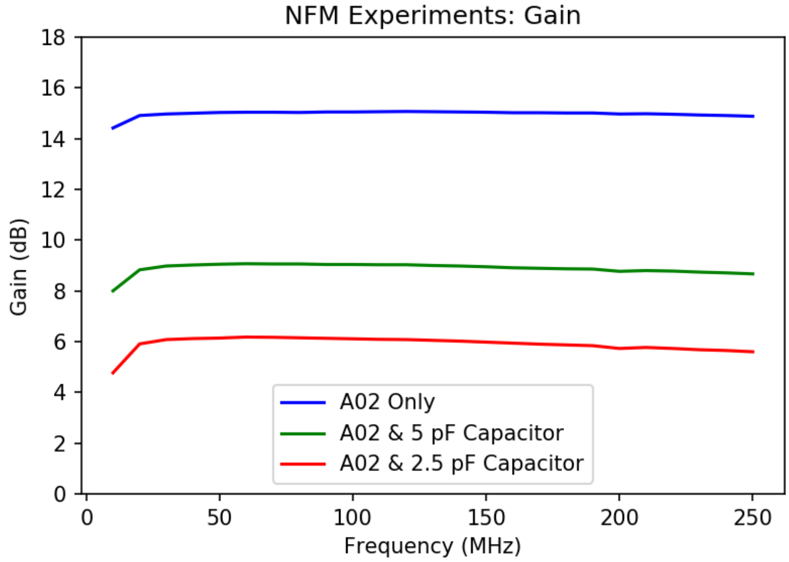

Figure 3.29: Total Gain for NFM Experiments with A02

In the plot, the curves that represent the the total gain for the series-capacitor cases appear at a fraction of the amplifier gain because they are reduced through the voltage divider gain. In our equations, we will denote the total gain g_T for the series-capacitor case by g_C (i.e. $g_T = g_C$ for the series-capacitor case). The total gain g_T for the amplifier-only case is just the amplifier gain g_A (i.e. $g_T = g_A$ for the amplifier-only case). Using equation (3.101), we can write the voltage-divider gain g_D for the series-capacitor case in terms of the two measured gains g_C and g_A on our Noise Figure Meter:

$$g_D = \frac{g_C}{g_A} \tag{3.102}$$

The reduction in gain for the series-capacitor case inevitably leads to an increase in the noise figure. We can understand this by looking at the equation for the noise figure (3.86) encountered earlier. When the gain decreases in equation (3.86), both the input signal and the input noise terms decrease by the same amount, but the noise contribution from the amplifier N_A remains the same. The output total noise therefore increases relative to the output signal, thereby increasing the noise figure. Below is a plot showing the noise figure measurement results for the amplifier-only case and the series-capacitor cases on the Noise Figure Meter.

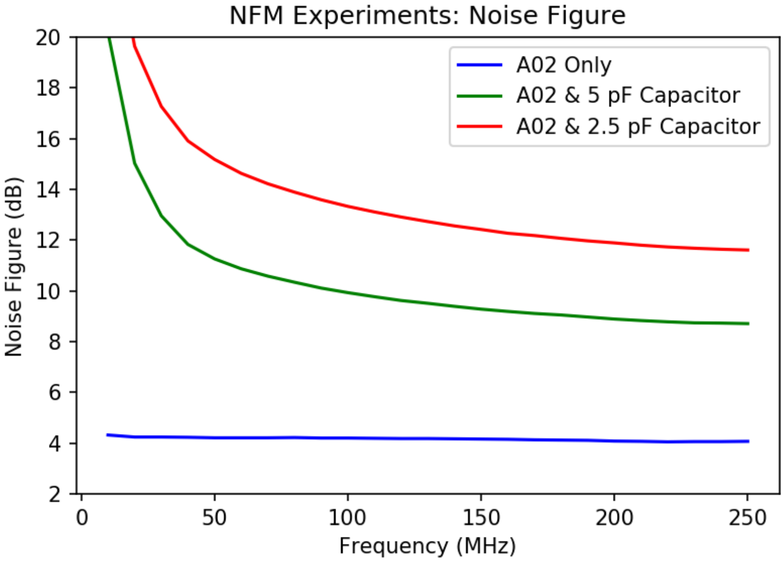

Figure 3.30: Noise Figure for A02

In the plot, we can see that the noise figures for the two series-capacitor cases are higher than the noise figure for the amplifier-only case. Since the $2.5pF$ series-capacitor case experiences the biggest drop in gain due to the voltage divider, it has the highest noise figure curve. In both the $2.5pF$ and $5pF$ series-capacitor cases, the noise figure curves increase more toward lower frequencies. This is because the source impedance Z_{source} increases with decreasing frequency in the series-capacitor case, and the contribution of the current noise to the noise figure therefore also increases with decreasing frequency.

The source impedance Z_{source} in the series-capacitor case is the parallel combination $Z_{C,NS||A}$ of the output impedance of the series capacitor $Z_{C,NS}$ and the input impedance of the amplifier Z_A. Both $Z_{C,NS}$ and Z_A are experimentally measured with our Vector Network Analyzer, and their parallel combination $Z_{C,NS||A}$ is calculated computationally from their individual impedance measurements. Recall that the amplifier impedance is included in the source impedance because the bias current I from the amplifier chip passes through the resistive and capacitative components of the amplifier input impedance in addition to passing through the impedance of the series capacitor and noise source. The source impedance Z_{source} in the series-capacitor case for a $2.5pF$ series capacitor is shown below. From this plot, it is clear that the source impedance is significantly larger in the series-capacitor case than in the amplifier-only case, especially toward the lower frequencies. As a result, the current noise term will be significantly larger in the series-capacitor case and will grow more toward lower frequencies.

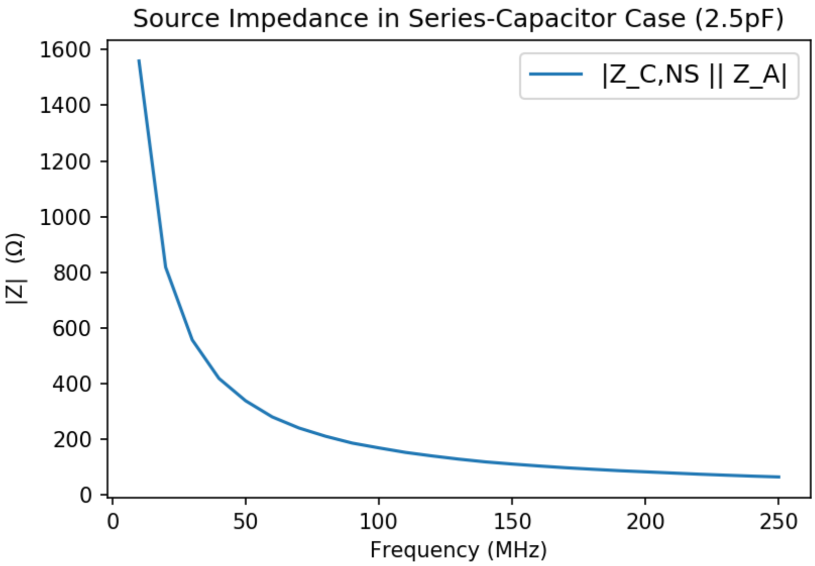

Figure 3.31: Source Impedance in Series-Capacitor case for 2.5pF Series Capacitor

Measuring the noise figure NF_C and gain g_C on the Noise Figure Meter in the 'series-capacitor' case, and substituting equation (3.101) for the total gain g_T, we can determine the total noise of the amplifier in the second combination using equations (3.91) and (3.98):

$$|V_{VN}|^2 + |IZ_{C,NS||A}|^2 = g_D \left(10^{\frac{NF_C}{10}} - 1\right) |V_i|^2 \tag{3.103}$$

The voltage noise term $|V_{VN}|^2$ in the 'series-capacitor' case is the same as in the 'amplifier-only' case because it is generated by the internal resistors (including the feedback resistors) in the amplifier and therefore independent of the source impedance that is connected to the amplifier input. If we subtract the total amplifier noise in the 'amplifier-only' case, given by equation (3.97), from the total amplifier noise in the 'series-capacitor' case, given by equation (3.103), we can eliminate this voltage noise term:

$$|IZ_{C,NS||A}|^2 - |IZ_{NS||A}|^2 = \left(g_D(10^{\frac{NF_C}{10}} - 1) - (10^{\frac{NF}{10}} - 1)\right) |V_i|^2 \tag{3.104}$$

In equation (3.104), the noise figure values for the amplifier-only case are denoted by NF and for the series-capacitor case by NF_C, the voltage divider gain g_D is determined by dividing the measured series-capacitor gain g_C by the amplifier-only gain g_A using equation (3.102), and the source impedances for the amplifier-only case $Z_{NS||A}$ and the series-capacitor case $Z_{C,NS||A}$ are both calculated from individual impedance measurements Z_{NS}, $Z_{C,NS}$, and Z_A on our portable Vector Network Analyzer. By measuring the noise figure, gain, and source impedance for the amplifier-only case, as well as the series-capacitor case, we can therefore experimentally determine the bias current I produced by our amplifier by solving equation (3.104) for I.

The input voltage V_i in equation (3.104) is just the Johnson noise voltage of a 50Ω resistor inside the noise source at room temperature:

$$|V_i|^2 = |V_{J,50}|^2 = 4k(293K)Re(Z_{NS}) \tag{3.105}$$

Solving for the current I in equation (3.104), and plugging in the input voltage from equation (3.105), we obtain the final equation for the experimentally determined bias current of our amplifier:

$$I = \sqrt{\frac{\left(g_D(10^{\frac{NF_C}{10}} - 1) - (10^{\frac{NF}{10}} - 1)\right) 4k(293K)(50\Omega)}{|Z_{C,NS||A}|^2 - |Z_{NS||A}|^2}} \tag{3.106}$$

Below I show the plots for I for the case of the $2.5pF$ Series Capacitor and $500nH$ Series Inductor, as well as the plots for the inverse-variance weighted average of all the series capacitors ad inductors used in the experiment. The final plot shows the errors to within $\pm 1\sigma$. The errors were determined using a Monte Carlo approach.

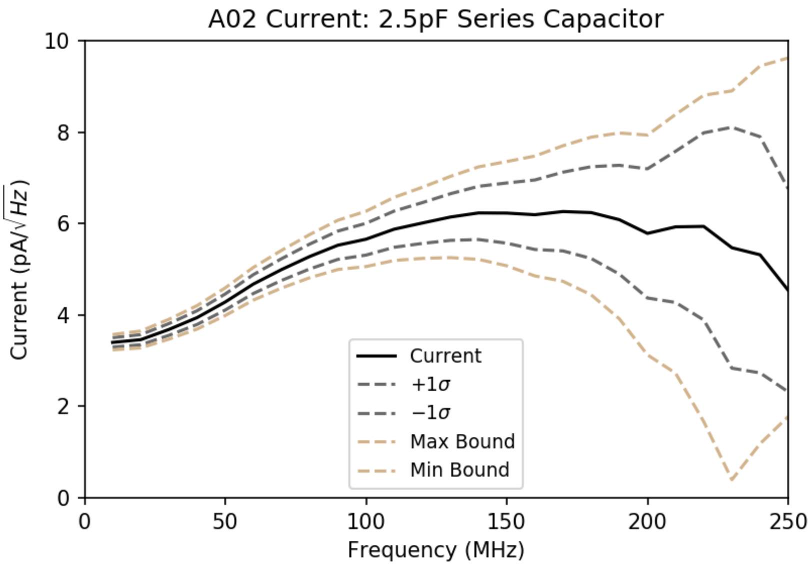

Figure 3.32: A02 Current from Noise Figure Meter Experiments

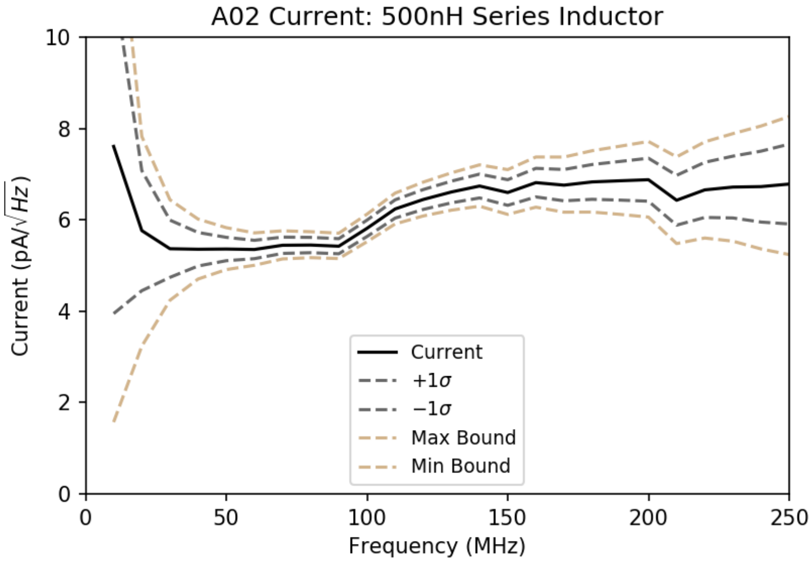

Figure 3.33: A02 Current from Noise Figure Meter Experiments

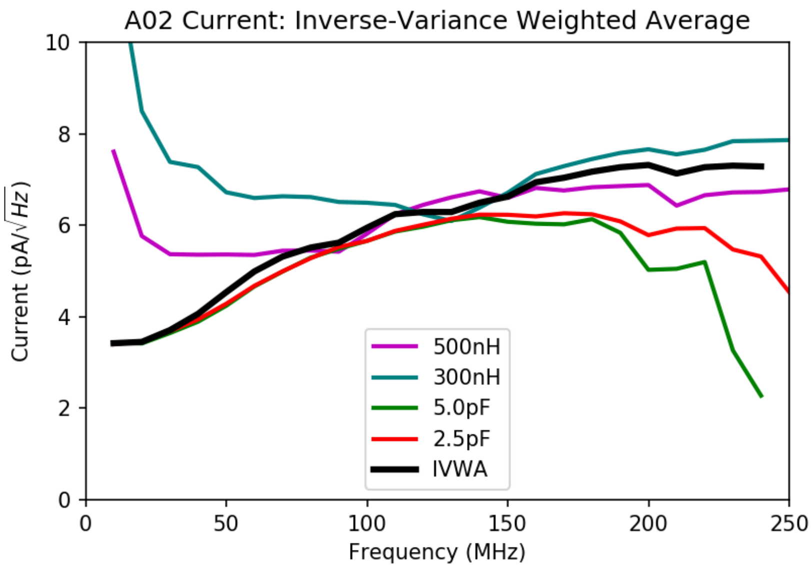

Figure 3.34: A02 Current from Noise Figure Meter Experiments

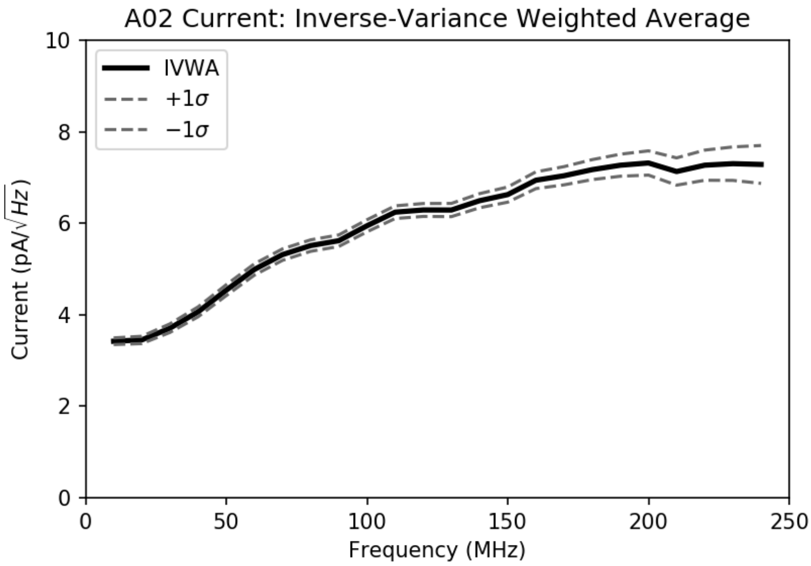

Figure 3.35: A02 Current from Noise Figure Meter Experiments

In the next set of plots, I show the inverse-variance weighted average for the voltage noise temperature of the amplifier T_{VN} for all the series capacitors and inductors used in the experiment. The final plot shows the errors to within $\pm 1\sigma$. As with the noise current I, the errors were determined using a Monte Carlo approach.

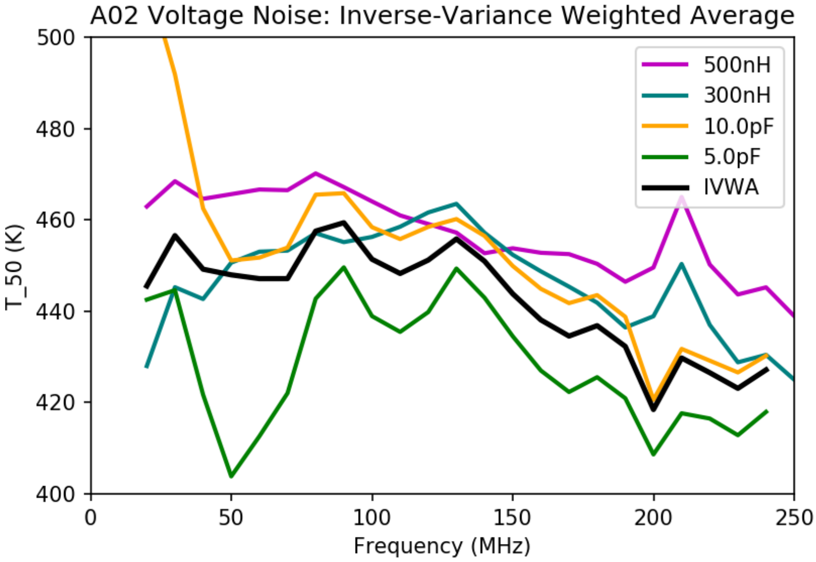

Figure 3.36: A02 Voltage Noise from Noise Figure Meter Experiments

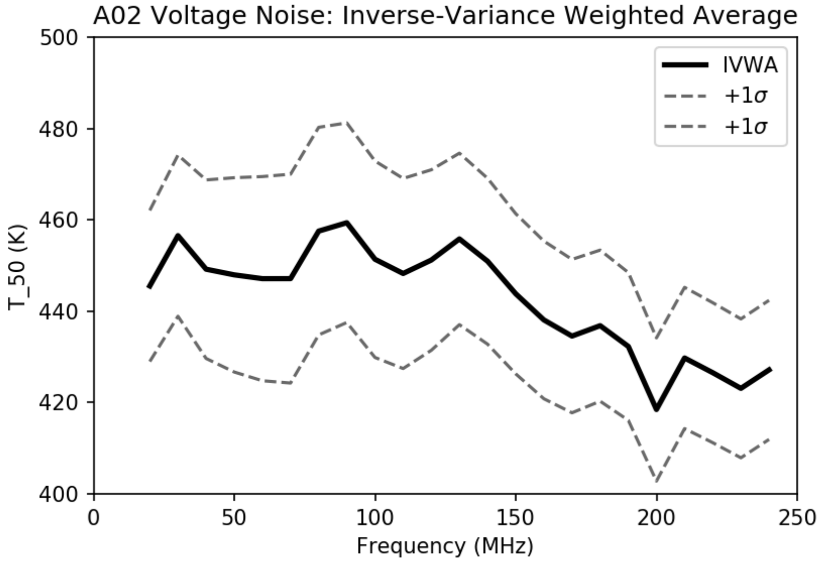

Figure 3.37: A02 Voltage Noise from Noise Figure Meter Experiments

3.3.5 Elimination Method

The voltage noise T_{VN} and the noise current i of the first LNA can be obtained by using the High-Z system to measure the spectrum of a long cable terminating in a load of high resistance. In this method, we first derive the total noise of the LNA by subtracting the noise contribution of the load and cable from the total measured spectrum. We do this by modelling the cable-filtered Johnson noise of the load at the input of the LNA using the MRRT model we developed earlier. Then, through further modelling, we separate the total noise of the first LNA into its voltage and current noise components. More specifically, the current noise component is determined by subtracting a model of the voltage noise from the total noise of the first LNA. Since the current noise is obtained through a series of subtractions of different models from a measured spectrum, this method is called the Elimination Method.

The experimental setup for this method is relatively simple. The antenna in the High-Z experiment is replaced by a long cable of 50Ω terminated by a resistive load with an impedance greater than 50Ω. In this experiment, we used an LMR-200 cable of length 487cm and 3 different loads, including 269Ω, 470Ω, and 1300Ω resistive loads. The experiment was conducted in the Faraday cage environment of the CMU Electrical Engineering Department's Screening room to avoid radio interference from various sources on campus, including radio stations, communication devices, and other electronic devices. Three different spectra were measured by the High-Z spectrometer, one spectrum for each of the loads that terminated the 487cm cable.

Although this method requires only one spectrum for analysis, and hence only one cable and load are necessary, the spectra from the other two loads can be useful for checking the consistency of this method, as well as error analysis. In addition to the spectra taken of the three loads in room temperature conditions, spectra is also taken when each of the loads is dipped into liquid nitrogen. The spectra from the loads in liquid nitrogen can be used to extrapolate the total noise of the LNA, which provides a useful cross-check on the MRRT model in addition to providing an independent way of deriving the total amplifier noise.

Once the spectra are obtained for each load terminating the 487cm cable at both room and liquid nitrogen temperature, the analysis proceeds for one load at a time. The analysis for the 470Ω load terminating the 487cm cable is discussed below, and proceeds exactly the same way for the other two loads.

The measured spectrum T_m of the 470Ω load terminating the 487cm cable must first be related to the total noise temperature spectrum sensed at the input of the LNA, which we will call T_{in}. According to the calibration equation (3.4), the measured spectrum T_m must be divided by the system gain G of the entire High-Z electronic chain to obtain the noise temperature spectrum at the input of the amplifier T_{in}. Notice that T_{in} includes both the input-referred LNA noise temperature T_{amp} and the noise temperature $T_{load}(\tau)$ from the load-cable combination itself:

$$T_{in} = \frac{T_m}{G} = T_{load}(\tau) + T_{amp} \tag{3.107}$$

The noise temperature of the load-cable combination $T_{load}(\tau)$ is just the multiple-reflected Johnson noise temperature of the load, which includes effects of cable loss and the cable's own emission and absorption. Therefore, $T_{load}(\tau)$ can be modelled by the MRRT model we developed earlier. Recall the MRRT equation (3.57) for the cable-filtered Johnson noise temperature of a load:

$$T_{load}(\tau) = T_{load}(0)e^{-\tau}\left(\left|\frac{Z_o}{Z_o + Z_L}\right|^2 |1+\Gamma_A|^2 \left|\frac{1}{1-\Gamma_A\Gamma_L e^{i2\delta}e^{-\tau}}\right|^2\right) + T_{cable}(1-e^{-\tau}) \tag{3.108}$$

$$T_{load}(0) = \left(\frac{293}{50}\right)\mathrm{Re}(Z_L) \tag{3.109}$$

In the MRRT equation, the load impedance Z_L, load reflection coefficient Γ_L, amplifier reflection coefficient Γ_A, and cable transmission $e^{-\tau}$ are all measured on a Vector Analyzer Network. The cable phase delay δ is calculated based on the measured length of the cable and the dielectric constant of the cable.

If we subtract the noise temperature of the load-cable combination, as given by the MRRT model, from the total noise temperature T_{in} in equation (3.107), we would be left with the noise temperature contribution T_{amp} of the LNA. This noise temperature of the LNA includes both the voltage noise T_{VN} component and the current noise T_{CN} component of the LNA. If we can find a way to model just one of these LNA noise components, then we could get the other component through subtracting from the total.

One observation that will help us greatly in separating the voltage noise component of the LNA from the current noise component of the LNA is the fact that the magnitude of the source impedance, which consists of the parallel combination of the load-cable impedance and the impedance of the LNA, varies sinusoidally as a function of frequency, containing both maximums and minimums. The values of the maximums and minimums depend on the value of the load resistance, with greater load resistance yielding higher maximums and lower minimums. For our $470\Omega - 487cm$ combination, the maximum values are approximately 470Ω, while the minimum values are close to 10Ω. The cable length controls the number of maximums and minimums in the frequency range.

We can take advantage of this sinosoidal nature of the magnitude of the source impedance by remembering that the current noise of the LNA depends on the magnitude of the source impedance. Recall the equation for the current noise temperature of the LNA:

$$T_{CN} = \frac{|IZ_{source}|^2}{4k(50\Omega)} \tag{3.110}$$

From the equation above, we see that the current noise of the LNA is maximum for maximum values of $|Z_{source}|$ and minimum for minimum values of $|Z_{source}|$. If we choose the resistance of our loads high enough, such that the sinusoidal variations of $|Z_{source}|$ swing to very low values at the minimum locations, then we can make the current noise of the LNA negligible at those minimums.

After subtracting $T_{load}(\tau)$ from the total noise temperature T_{in}, the remaining total noise of the amplifier T_{amp} will contain resonance peaks in its spectrum. If we compare the sinusoidal variation of $|Z_{source}|$ to the cable resonances present in T_{amp}, the maximums and minimums of both coincide at the same points in frequency. This makes sense, as the total noise of the amplifier contains current noise which oscillates with the varying behavior of $|Z_{source}|$.

If we choose a load-cable combination that has frequent oscillations of $|Z_{source}|$ with minimums close to the value of zero, then we know the minimums of the resonances in T_{amp} will contain a negligible amount of current noise and will consist only of the voltage noise of the LNA. We can therefore fit a curve to those minimums and create a model of the voltage noise of the LNA, assuming that the voltage noise of the LNA varies smoothly across the minimum points.

$$T_{VN} = (T_{amp})_{mins} \tag{3.111}$$

In the first plot below, we show the minimums of T_{amp} for the $470\Omega - 487cm$ combination, as well as the best fit curve to the minimum points. As mentioned earlier, the value of $|Z_{source}|$ varies from 470Ω at the maximums to 10Ω at the minimums. If we assume an estimated noise current of the LNA to be approximately 6pA, then a value of 10Ω for the magnitude of the source impedance will yield a noise current contribution of 1.3K at the minimums. Therefore, the minimums of T_{amp} will correctly model the voltage noise of the LNA to within approximately 1K.

In the second plot below, we show the voltage noise of the LNA as determined by equation (3.111). The error analysis is completed using Monte Carlo methods and the error reported is within $\pm\sigma$.

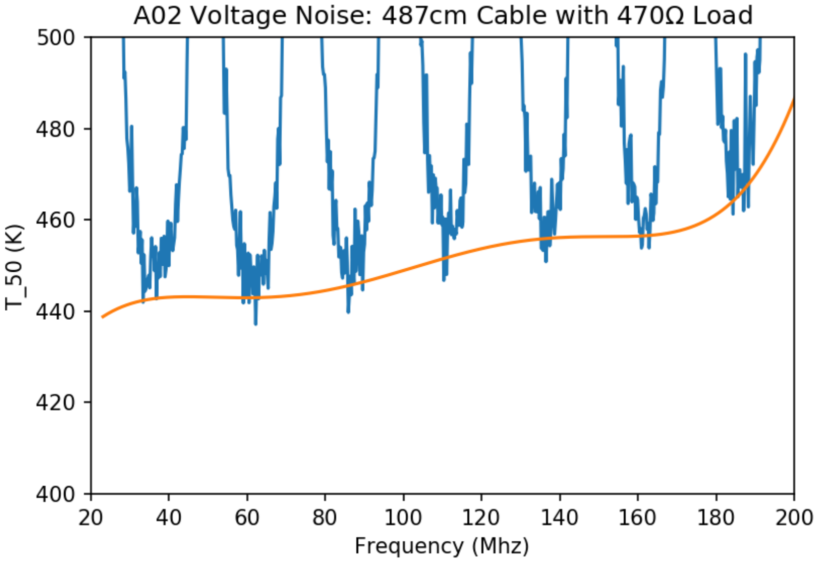

Figure 3.38: A02 Voltage Noise for a 487cm cable terminated by a 470ohm load

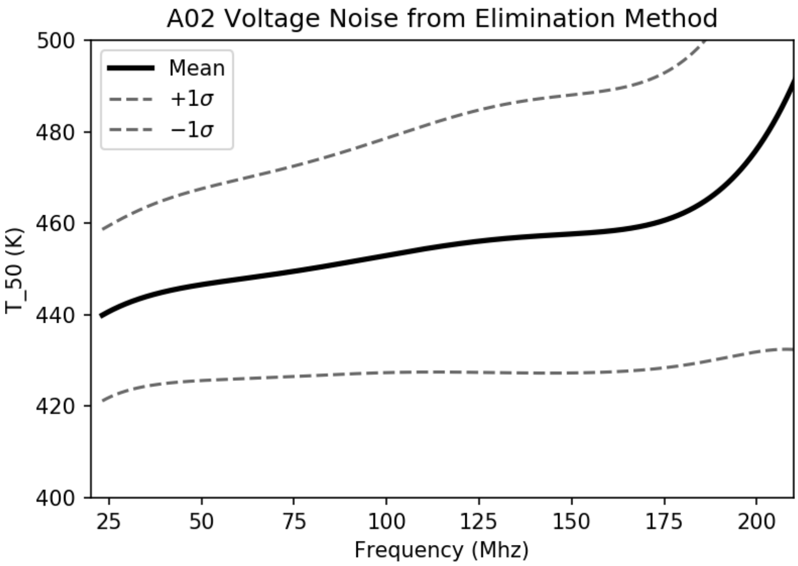

Figure 3.39: A02 Voltage Noise from Elimination Method

Now that we have a model of the voltage noise of the LNA, we can subtract it from the total noise of the LNA to get the current noise.

$$T_{CN} = T_{amp} - T_{VN} \tag{3.112}$$

Remember that it is the noise current I of the LNA which we are finally seeking, so we must use the measured value of $|Z_{source}|$ for the $470\Omega - 487cm$ combination to convert the current noise T_{CN} in equation (3.112) to a noise current I:

$$|I| = \sqrt{\frac{4k(50\Omega)T_{CN}}{|Z_{source}|^2}} \tag{3.113}$$

Below is a plot of the noise current I obtained after following the procedure of this Elimination Method. Notice that there are spikes in the data that correspond to the locations of the minimums in the total noise of the LNA. At these locations, the difference (T_{amp} - T_{VN}), which we used to determine T_{CN}, becomes too small to be reliable and causes spikes in the data as we see below. We can ignore these spikes and the points nearby, and focus on the more reliable points in between the spikes. In the second plot below, I select the points that represent the average values of the current in the sections between the spikes. I then fit a line through those points to generate the plot of the noise current I as a function of frequency for the Elimination Method. In the third plot below, I show the results of this fit, as well as the errors of this method for the noise current I. The error analysis is done with Monte Carlo methods and the error reported is $\pm\sigma$.

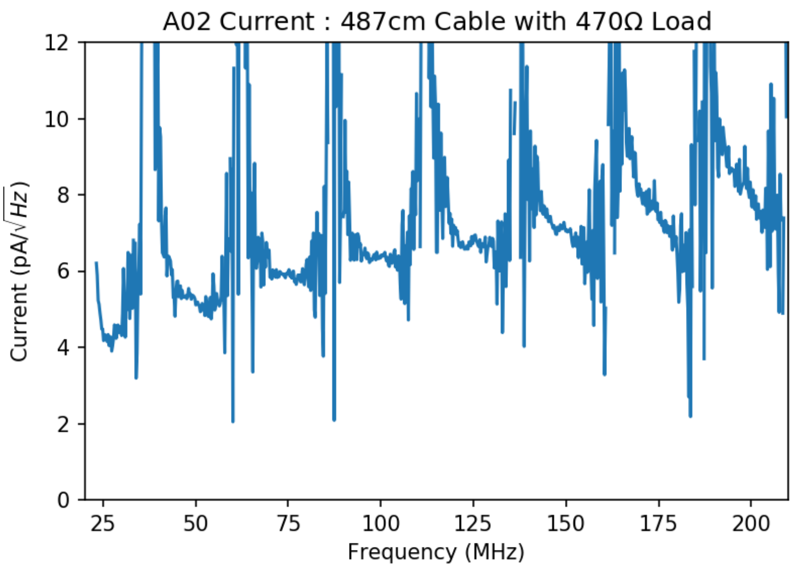

Figure 3.40: A02 Current for a 487cm cable terminated by a 470ohm load

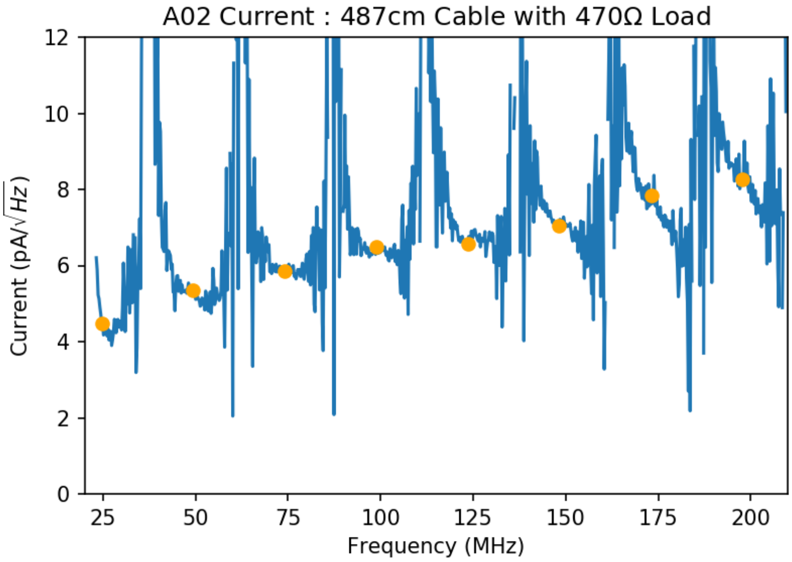

Figure 3.41: A02 Current for a 487cm cable terminated by a 470ohm load

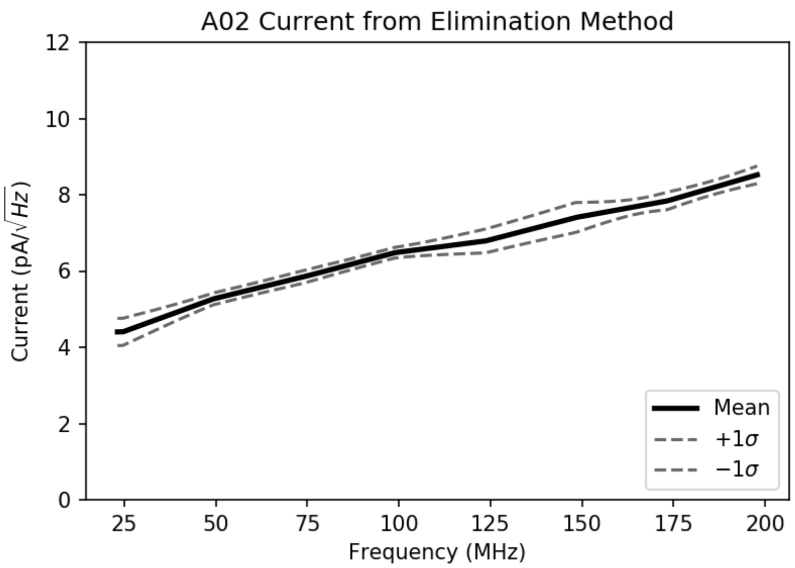

Figure 3.42: A02 Current from Elimination Method

3.3.6 LNA Noise Temperature

If we combine the results from all of our methods for the noise current I and the voltage noise temperature T_{VN} of the first LNA, we can see what those results tell us about the noise properties of the LNA and how they compare to the values reported on the LNA data sheet. Below I show plots for the noise current I and the voltage noise temperature T_{VN} of the first LNA. In each plot, the results from all of the methods have been shown. The errors for each method are calculated using Monte Carlo methods and are indicated in the plot by shaded regions. The errors are shown to within $\pm 3\sigma$.

In the plot of the noise current I of the LNA, we can see that the value of the noise current for all the methods used is well above the value reported on the LNA's data sheet. Recall that the stated value of the noise current for the low-noise amplifier LMH6629, which we refer to as simply "A02", is $2.6pA/\sqrt{Hz}$ on the data sheet[23]. However, all methods show the noise current to be above 3pA in the entire frequency range of our experiment. In addition, the noise current appears to grow with frequency in both the Noise Figure Method and the Elimination Method. Although the noise current from the Rothe-Dahlke method agrees with the Elimination Methods only up to 75Mhz, both the NFM and the Elimination Method agree with each other to within $\pm 3\sigma$ for the entire frequency band.

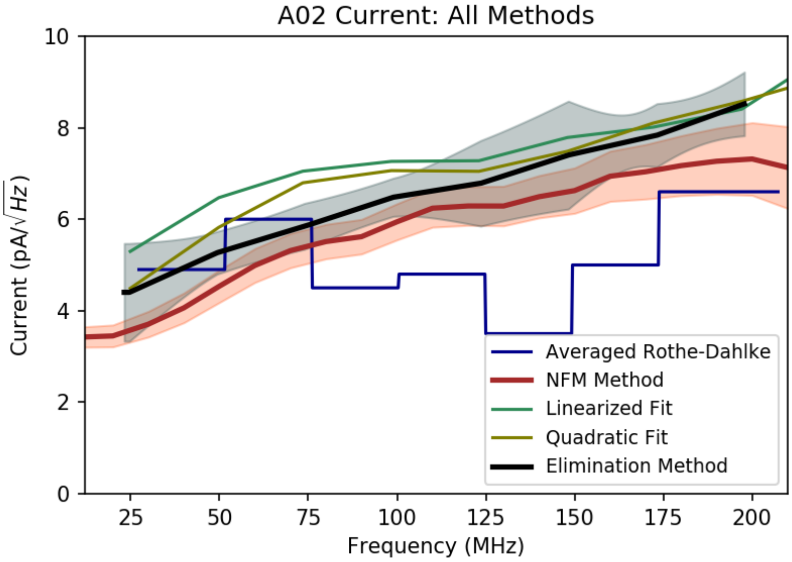

Figure 3.43: A02 Current from All Methods with 3σ Errors

In the plot of the voltage noise temperature T_{VN} of the LNA, we see that the value obtained by our methods is also well above the reported value on the data sheet of the LNA. Recall that the data sheet lists the value of the noise voltage of the amplifier LMH6629 as $0.69nV/\sqrt{Hz}$, which corresponds to 172K in noise temperature units. This noise voltage does not include the Johnson noise contribution of the feedback network. However, we took into account the noise contribution of the feedback network in our theoretical calculations in section "Theoretical Estimates of Noise". There we found that the voltage noise temperature, including the Johnson noise of the feedback resistors, should be approximately 417K. Both the Noise Figure Meter method and the Elimination method are slightly more than 20K above that level. Although the NFM and the Elimination method do not match with the theoretical predictions we made, they do however agree very well with each other, especially in the range 25Mhz-125Mhz. One thing to note about the voltage noise temperature is that the errors shown in the plot are within $\pm 1\sigma$, unlike in the plot of the noise current.

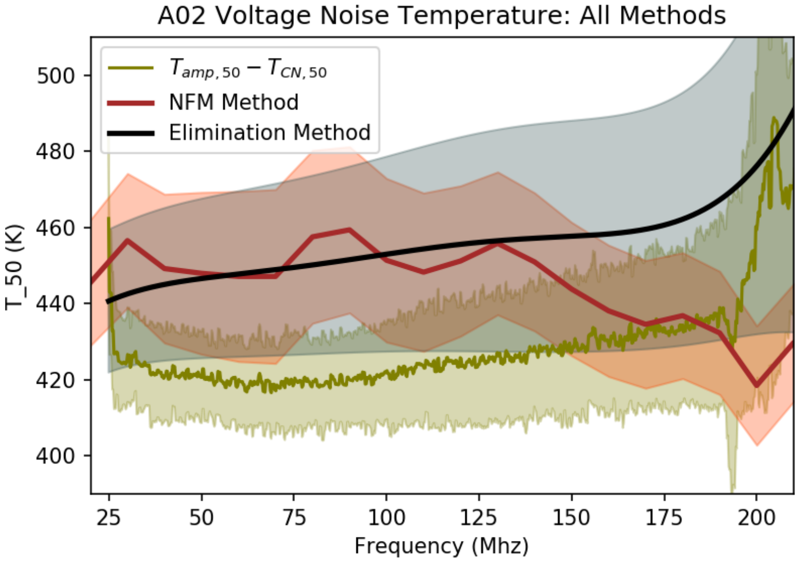

Figure 3.44: A02 Voltage Noise Temperature from All Methods with 1σ Errors

We can now use the results obtained for the noise current I to predict the current noise temperature T_{CN} of the LNA when one of our antennas is connected to the system. We have decided to use the results for the noise current I derived from the Elimination Method. In order to predict the current noise temperature T_{CN}, we must measure the impedance of each antenna $Z_{antenna}$ and derive the source impedance Z_{source} corresponding to the respective antenna. The source impedance is the parallel combination of the impedance of the antenna with the impedance of the LNA Z_A, and is calculated as follows:

$$Z_{source} = \frac{1}{\frac{1}{Z_{antenna}} + \frac{1}{Z_A}} \tag{3.114}$$

The current noise temperature T_{CN} for the source impedance corresponding to each antenna is then calculated by:

$$T_{CN} = \frac{|IZ_{source}|^2}{4k(50\Omega)} \tag{3.115}$$

Below we see the plots of the LNA's current noise temperature T_{CN}, voltage noise temperature T_{VN}, and the total noise temperature T_{amp} for each antenna separately. Each noise components is given to within a $\pm 1\sigma$ standard deviation, which is indicated by the shaded region. Underneath each plot of the LNA's noise components for the given antenna, we show the source impedance corresponding to that antenna, since the source impedance greatly determines the current noise temperature T_{CN} of the LNA. In addition, for the extra small antenna (20cm), we provide additional, zoomed-in plots for each component of the LNA noise, in the frequency range 25Mhz-125Mhz. The zoomed-in plots allow us to see more clearly the values of each component of the LNA noise, and the errors associated with it, in the frequency range where we expect to see the cosmological signal.

Notice that in the plot of the noise components of the LNA corresponding to the Extra Small Antenna (20cm), the current noise of the LNA is approximately equal to the voltage noise of the LNA at 25Mhz. The current noise of the LNA, however, decreases steeply with frequency, such that by 50Mhz the current noise of the LNA is approximately 110K, at 75Mhz the current noise is 50K, and by 100Mhz the current noise is down to 30K. The error corresponding to the current noise also decreases with frequency, with a standard deviation of approximately 10K at 50Mhz, 3K at 75Mhz, and 1K at 100Mhz.

For all the antennas considered in our system, the current noise is highest toward the lower frequency regions. The current noise temperature contributes to a significant fraction of the total noise temperature of the LNA in the frequencies below 125Mhz for the 20cm antenna, below 110Mhz for the 25cm antenna, and below 75Mhz for the medium antenna. The current noise of the 20cm antenna contains the highest level of current noise overall, due to the larger impedance of the antenna. The value of the voltage noise does not vary with impedance, so it remains the same for all antennas.

The results obtained here for the total noise temperature of the LNA in the case of each antenna are very important to our calibration of the system, since they provide the correct total noise temperature T_{amp} that must be used in our main calibration equation (3.4) for each respective antenna.

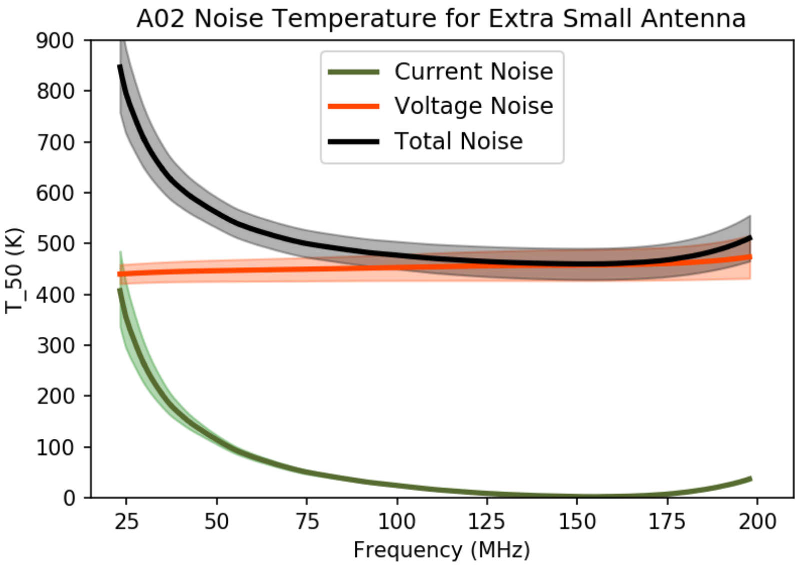

Figure 3.45: A02 Noise Temperature for 20cm Antenna with 1σ Errors

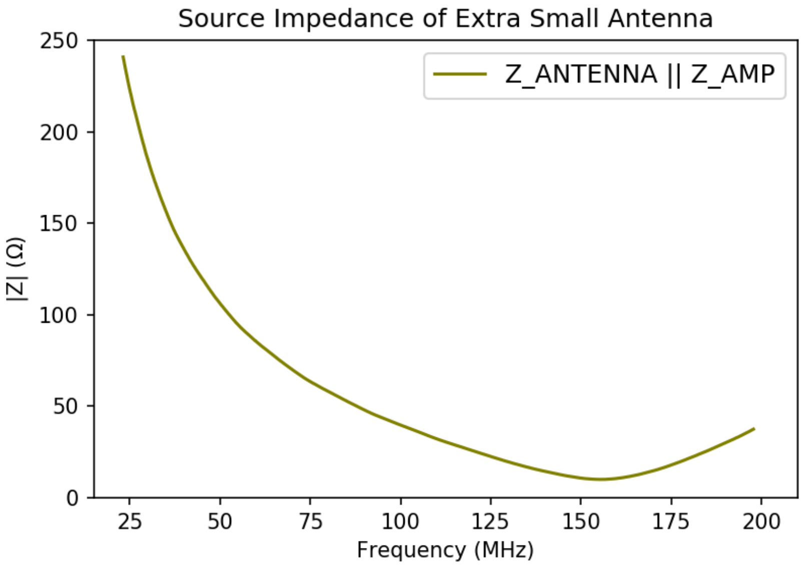

Figure 3.46: Source Impedance for the Extra Small Antenna

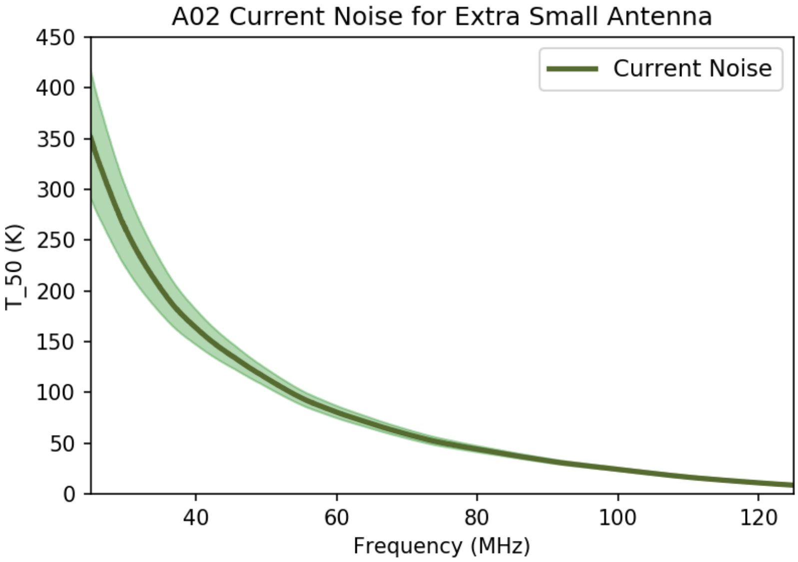

Figure 3.47: A02 Current Noise for 20cm Antenna in Range 25Mhz-125Mhz

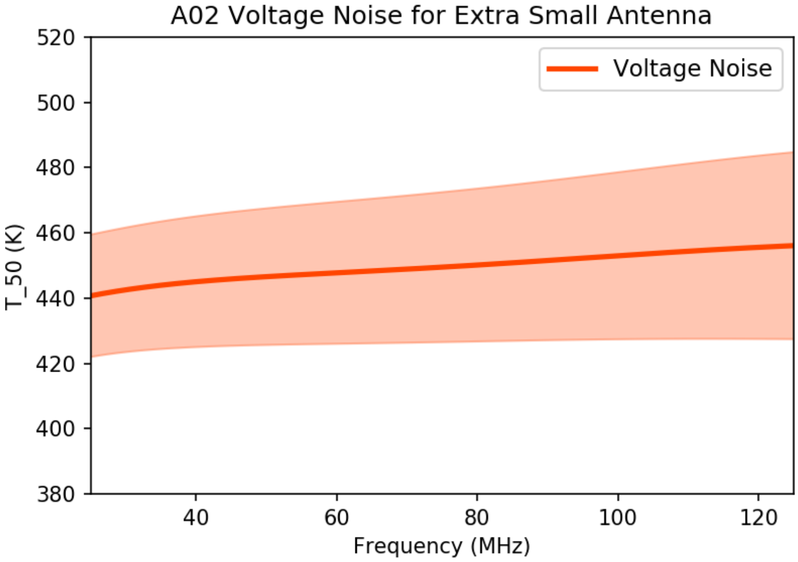

Figure 3.48: A02 Voltage Noise for 20cm Antenna in Range 25Mhz-125Mhz

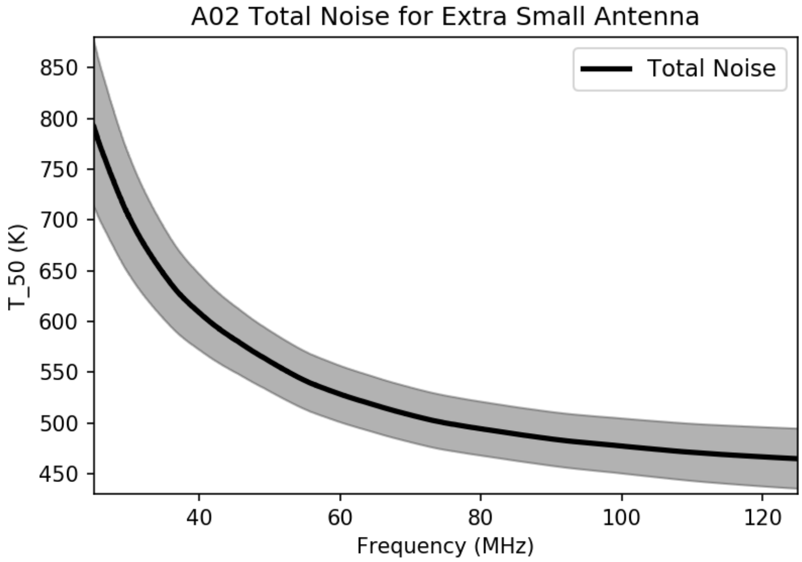

Figure 3.49: A02 Total Noise for 20cm Antenna in Range 25Mhz-125Mhz

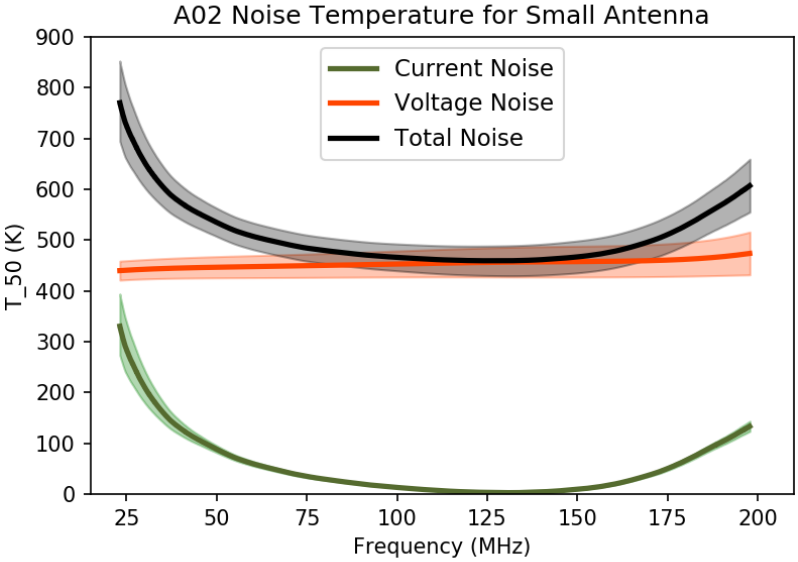

Figure 3.50: A02 Noise Temperature for 25cm Antenna with 1σ Errors

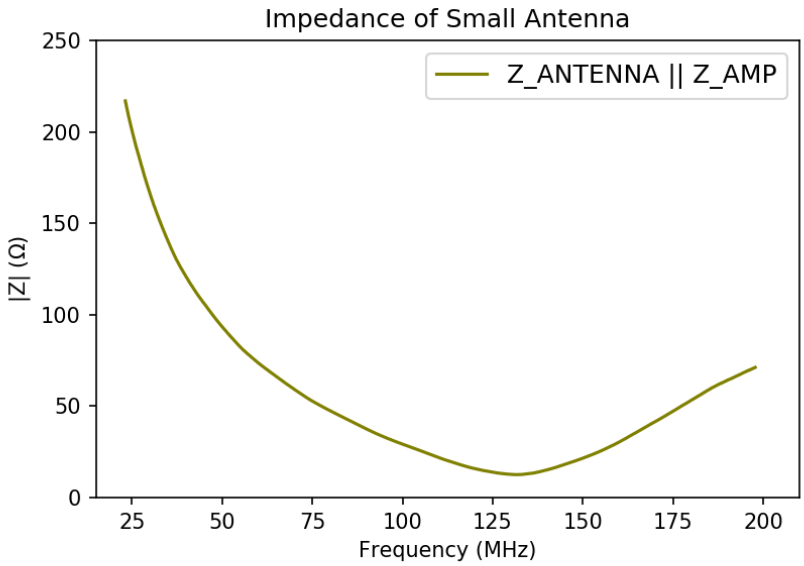

Figure 3.51: Source Impedance for the Small Antenna

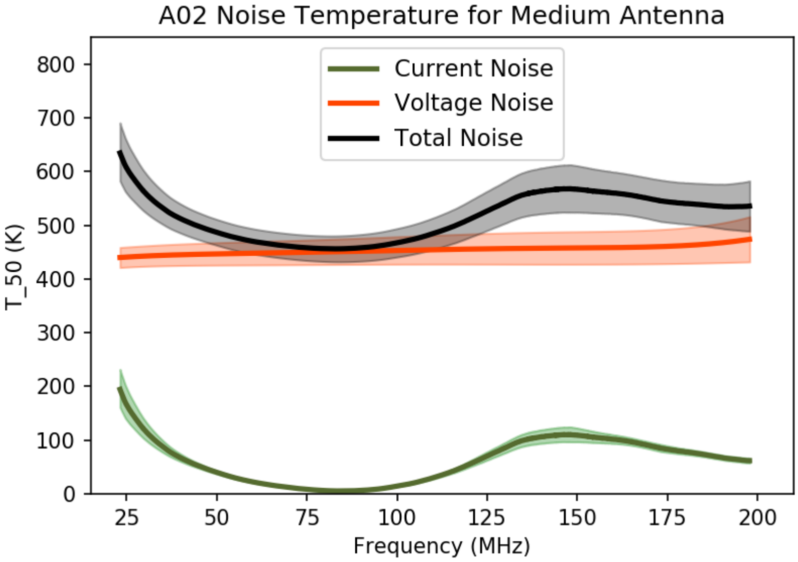

Figure 3.52: A02 Noise Temperature for 54cm Antenna with 1σ Errors

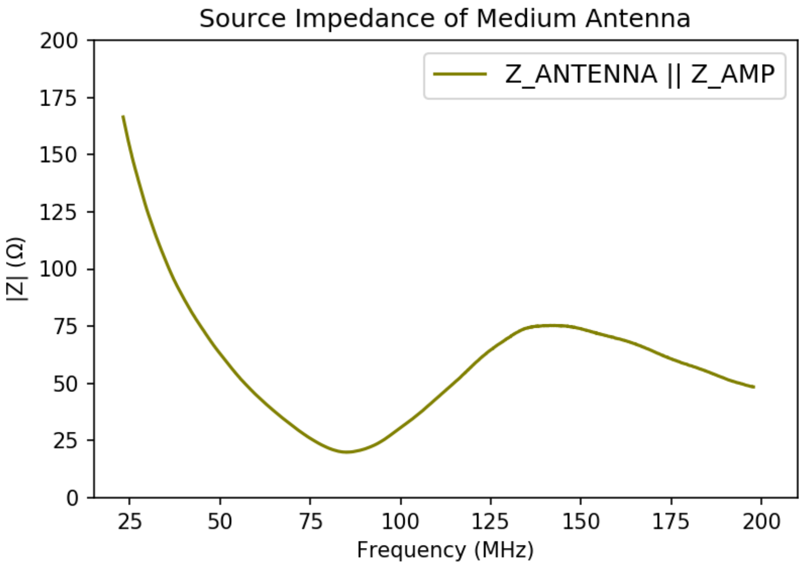

Figure 3.53: Source Impedance for the Medium Antenna

3.4 Field Calibration

When observing the sky in the field during deployments, the High-Z system is exposed to changing temperatures of the day and night. These variations in the ambient temperature will lead to variations in the system's total noise contribution T_{amp}. Recall that the system's noise contribution consists primarily of the noise of the first LNA. This is due to the fact that the noise of the first LNA is injected into the electronic chain at the earliest stage and therefore experiences the full gain of the system.

In the previous sections, we saw that the voltage noise of the LNA consists of the Johnson noise of the resistive components inside the LNA, including the feedback resistors. From equation (3.7) for the Johnson-Nyquist noise, we see that the magnitude square of the Johnson noise voltage is proportional to the physical temperature of the resistive component that is generating the noise. Therefore, we can expect the voltage noise of the first LNA to vary linearly with the ambient temperature T:

$$(T_{VN})_T = \left(\frac{T}{293}\right)(T_{VN})_{293} \tag{3.116}$$

If the LNA is positioned after the mechanical switch that takes input from the antenna and the internal calibration sources, then the variation of the voltage noise of the first LNA with the ambient temperature fluctuation in the field can be measured by using the internal calibration sources. we will describe the internal calibration sources below and explain how they are used to calibrate the system in the field.

The internal calibration sources used in the field consist of a 50Ω load and a noise source, which connect to one terminal of the mechanical switch while the other terminal of the switch is connected to the antenna side (see block diagrams of the system in Chapter 2). The noise source on the calibration side of the switch has an ON and OFF setting, with the OFF setting corresponding to the noise figure of a 50Ω load while the ON setting corresponds to a noise figure that is approximately 15dB brighter. The exact noise spectrum of the noise source is measured with a Spectrum Analyzer in the lab. We have used a different noise source for different versions of our system, with the noise source corresponding to version 3 having a model number XDM 1600.

The internal 50Ω load and noise source are used as sources of known noise temperature spectrum that allow us to obtain the system gain G and the amplifier noise temperature T_{amp} in the main calibration equation (3.4). The calibration procedure using the internal calibration sources is identical to the calibration procedure using the Johnson load at room and liquid nitrogen temperature, with the exception that the sources used are different. Therefore, the equations yielding the system gain G and the amplifier noise temperature T_{amp} using the internal calibration sources take on the form:

$$G = \frac{T_{m,50} - T_{m,NS}}{T_{s,50} - T_{s,NS}} \tag{3.117}$$

$$T_{amp} = \frac{T_{m,50}}{G} - T_{s,50} \tag{3.118}$$

For version 1 of the system, when the first LNA was downstream the mechanical switch in the RF box, the field calibration equations (3.117) and (3.118) allowed us to measure the variation of the LNA noise temperature T_{amp} in the field as a result of the fluctuation of the ambient temperature. However, for versions 2 and 3 of the system, with the first LNA located upstream of the mechanical switch, the noise signal from the internal calibration sources does not pass through the first LNA and equations (3.117) and (3.118) therefore excludes the effects of the first LNA. In addition, for versions 2 and 3 of the system, the quantities G and T_{amp} in equations (3.117) and (3.118) no longer refer to system gain and LNA noise temperature. Rather, they refer to the gain and the noise temperature of the electronic chain after the first LNA.

Since we cannot measure the variation of the LNA noise temperature T_{amp} using the internal calibration sources for versions 2 and 3 of the system, we need use another method for tracking the changes in the LNA noise temperature T_{amp} in the field. One method is recording the ambient temperature of the RF Box with a thermocron sensor and then using equation (3.116) to predict the LNA voltage noise temperature T_{VN} at the ambient temperature of the RF Box. Since the current noise of the LNA is independent of temperature, the change in the total noise of the LNA as a result of ambient temperature change in the field is contained fully in the voltage noise term T_{VN}. Therefore, combining equation (3.116) and (3.5), we get the total noise temperature of the LNA in the field:

$$T_{amp,f} = T_{CN} + \left(\frac{T}{293}\right)(T_{VN})_{293} \tag{3.119}$$

In equation (3.119), the voltage noise temperature of the LNA at 293K, given by $(T_{VN})_{293}$, is derived using the Elimination Method discussed earlier. The current noise temperature T_{CN} for the respective antenna used in the field is derived using the measured impedance of the antenna $Z_{antenna}$ and the noise current i derived using the Elimination Method. Temperature T represents the ambient temperature of the RF Box, as measured by the thermocron sensor in the RF Box.

The system gain G for versions 2 and 3 of the system can be obtained one of two ways. First, we can use the system gain G obtained from the absolute calibration, using the Johnson load at room and liquid nitrogen temperatures. Second, we can use the gain of the system after the first LNA, as measured by the internal calibration sources in the field using equation (3.117), and multiply this gain with the measured gain of the first LNA. As we showed in our lab tests, the gain of the first LNA does not vary with temperature and can therefore be assumed to stay constant with ambient temperature changes in the field.

Chapter 4

High Z Deployments and Sites

4.1 March 2019

Our deployment to Karoo Site 4 in South Africa in March 2019 was filled with many challenges and tribulations. However, we learned a lot from our experiences there, so it is worth to recount the challenges we faced and the solutions we devised in the field for dealing with those challenges.

Upon returning to Karoo and setting up at Site 4, we were greeted with an extremely heavy downpour from a thunderstorm that passed through the region. This downpour almost seemed heavenly, as we were very tired after setting up and thoroughly enjoyed relaxing and watching the rain come down after finishing our work. However, when we arrived the next day at the site and checked the status of our system, we found standing waves in the spectrum of the antenna and the internal calibration sources. Since the standing waves appeared in all three sources and we knew that heavy rains had passed the day before, we determined the most likely cause of this problem was a residue of water that seeped into the cable connections. We therefore disconnected the main cable connecting to the RF Box and the Spectrometer Box and thoroughly dried and clean the connection. After doing so, the standing waves in the spectra disappeared and the spectra in all three sources returned back to normal.

Figure 4.1: Thunderstorms at Karoo Site 4

We were very happy to have solved the problem of standing waves in our spectrum so easily. However, our happiness was again very short-lived, as we discovered upon the next day that our system has turned off for an unknown reason. Although there were a variety of reasons that could have caused the system to shut down, we guessed that the most likely reason was due to overheating of the system due to the extremely hot temperatures that persisted during the entire time of our deployment.

My advisor Jeffrey Peterson, the MacGyver of cosmology, was able to quickly devise a simple yet clever way of preventing the future overheating of our system. He took an oversized plastic water container and created a very small hole at the bottom that allowed the water to drip from beneath the container (in fact, he made two holes, one at the bottom of the container, and one at the top of the container that allowed the air to fill the container as the water was emptying out). However, dripping water onto the system is not something that is desirable, as demonstrated by the thunderstorms that left standing waves in our spectra. To prevent the water from going into the cables, and to cool off the system as a whole rather than just one part, Jeffrey Peterson took one of his shirts and spread it across the main part of the Spectrometer box before laying on it the water container with the hole at the bottom. This allowed the shirt to absorb the water in the container at a slow rate and to spread that moisture throughout the whole Spectrometer Box, cooling it off in the summer heat (Southern Hemisphere later summer).

Following these initial challenges, the High-Z system ran smoothly without any problems in the field. We were able to collect data with all three of our antennas, measure the S11 of all the antennas in the field in the environment of the site, conduct a two radial test to determine the reflection properties of our radials, collect soil samples underneath the radials, and test our new solar panels system for charging the batteries that run the system.

4.2 October 2020

The idea for a new, radio-quiet site in North America utilized for our October 2020 deployment was suggested to us by Professors Jon Sievers and Cynthia Chiang from McGill University. Uapishka station on the Manicouagan reservoir of Northern Quebec is both isolated and radio-quiet, offering accommodations and facilities to both wildlife scientists and nature-loving vacationers. With a majestic scenery and a nice set of cabins by a circular lake created by a meteor millions of years ago, one instantly senses that this is the right place to look for an ancient signal from the universe. However, we must not rely on beauty in radio astrophysics, but on scientific testing. Therefore, the first order of business we had to attend to upon arriving to the Manicouagan reservoir was measuring precisely how much man-made radio-frequency interference (RFI) we could detect in the various areas in the region. Although other radio astrophysicists have told us this was a potential radio-quiet site, we needed to verify this with our own measurements, especially because this was a new site for us and it was not actively used for radio-astrophysics purposes.

We measured the spectrum at three different locations, including beside the lake near the cabin area of Uapishka station, by kilometer marker 308 on the main route 389, and finally in the quarry about a mile across the road from the main Uapishka station. The picture below shows our site-testing equipment measuring the RFI on the beach beside the lake near the Uapishka station. Notice that we use a special net around our site-testing spectrometer as a Faraday cage to block the RFI originating from the spectrometer.

A sample of the site test spectrometer read-out is shown in the picture below for the quarry location across the Uapishka station. In the spectrum, we can see strong RFI below 20 Mhz and a multitude of faint RFI lines between 240 Mhz and 280 Mhz. In both cases, the RFI are outside our frequency band and will be blocked by our high-pass and low-pass filters. Inside our frequency band, we see one faint RFI line around 137 Mhz, which corresponds to the frequency of the Orbcomm satellite. As mentioned before, signals from the Orbcomm satellite show up every 90 minutes at most locations and are very difficult to avoid. However, the Orbcomm signal is narrow in frequency and only about 10dB above the noise floor. Therefore, the signal will not overload our amplifier and can be excised when cleaning and preparing the date for analysis. In addition to the Orbcomm line, two more transient lines are visible in the spectrum around 65 Mhz and 185 Mhz. These lines are both less than 5 dB above the noise floor and can be excised from the data set before analysis.

Other signals can appear in the spectrum at different times. These transient frequencies can range from relatively weak ($\sim 5 - 10dB$ above noise floor) to fairly strong ($\sim 30 - 40dB$ above noise floor). Most of these transient RFI signals are very narrow in frequency and do not overload our amplifier. Therefore, just like the Orbcomm satellite signal, they can be excised out of the data before analysis. The origin of the transient RFI signals include radio communications among truck drivers using route 389 (truck drivers can communicate long range using relay stations, which pass on their signals from one relay station to another), air traffic communication, meteor scattering events, and an occasional weak signal that makes it through from a far off FM radio station.

Figure 4.2: Manicouagan Reservoir, Measuring Radio Frequency Interference (RFI) in the Area.

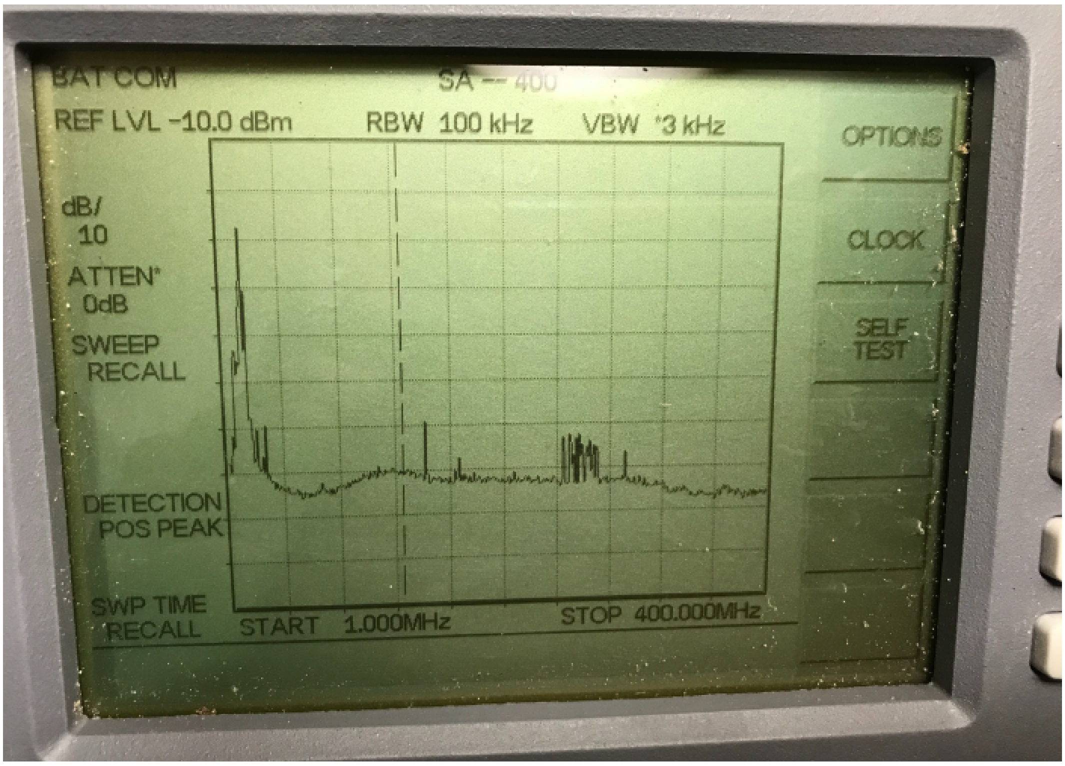

Figure 4.3: Site Test Spectrum at Quarry Site near Uapishka Station.

After verifying the radio quietness of the area around the Manicouagan Reservoir, our next task was to find potential sites for our High-Z experiment. No other astrophysics group had used a site in this region before, so there was no pre-determined site ready for us to use. Therefore, we had to invest some time and resources to find a suitable area for our observations. First, we surveyed various geographic regions on the map to find areas that showed large clearings, including large strips of beach area, quarries, and areas cleared by the logging industry. Second, we had to drive to those locations to determine the viability of those sites for our experiment. Finding a good area is not easy since the potential site must meet all the requirements of our experiment: 1) the site must be on a level surface and cleared of all structure and large vegetation in a circular area at least 60 meters in diameter 2) the site must be undisturbed for the entire duration of the observation period 3) the site must be radio-quiet 4) the site must be easily accessible by a car, truck, or small boat.

After scouting several areas in the region, we determined that the quarry about a mile across the road from the Uapishka station met all of our requirements. Although the quarry is still listed as active, we learned through conversations with the locals that in practice it was not being used. Another quarry further up route 389 was utilized by the road construction crew. We were told that occasionally a few people could be found camping on our quarry site, but otherwise it was largely undisturbed. The quarry was conveniently large and circular in area, with more than 60 meters of level ground to spread out our radials. The spectrum from the site testing kit showed the quarry site to be very radio quiet, with only a few weak and transient signals appearing from time to time. Being surrounded by low-level mountains on almost all sides, the location was shielded from nearby ground-based RFI signals. However, the mountains were distant and short enough to protrude only $10° - 20°$ from the horizon, allowing the antenna access to most of the sky. A small gravel road led to this site from the main route 389, which made the quarry easily accessible by a car or truck.

Given that the quarry site met all of our requirements, we decided upon this location for our observations. We set up our High-Z system on the quarry site on October 12, 2021. After setting up and starting the system, we checked the spectra of the antenna, noise source, and the internal 50Ω resistor with our Real Time Viewer. Instead of seeing the gently sloping spectra we were expecting, we saw ringing in all three spectra, indicating a problem. To diagnose the location of such a problem, we can use a portable Vector Network Analyzer (VNA) to measure the spectrum at various points in the system, using the internal Spectrum Analyzer of the VNA, until it is clear at which point the ringing develops in the spectrum.

We started by breaking the electrical connection between the High-Z spectrometer box and the RF box and connecting the portable VNA to the RF Box at the end of the very long cable usually used between the spectrometer box and the RF box. After seeing the same ringing, we eliminated the spectrometer box as the source of the problem since the ringing persisted after the spectrometer box was excluded from the spectrum. The problem had to come from one of the following: water residue inside the SMA connectors of the long cable, bad attenuators at either end of the long cable, or a faulty electrical component inside the RF box. In such situations, the best way to proceed is to tackle the scenarios easiest to test first. In our case, the easiest scenario to test was the bad attenuators at both ends of the long cable. After removing the attenuators at both ends of the long cable (10 dB on the end connecting to the RF Box and 3dB on the end connecting to the spectrometer box end), we remeasured the spectra with the VNA. The ringing in the spectra disappeared and all three spectra (antenna, noise source, and internal 50Ω resistor) looked normal and as expected.

After diagnosing the ringing problem in the spectra, we took S11 measurements of all the antennas, conducted our two radial test, and started collecting data with the 20cm antenna. Below is a diagram of the High-Z equipment set-up at the quarry site. Several pictures of the site are provided below the diagram.

The first picture shows the High-Z system set up on the quarry site. In this picture, the camera is pointing to geographical northwest. A white bucket covers the 20cm antenna and a clear tarp protects the RF box buried underneath the ground from excess water. One lesson we learned from the strong rain storms at the Karoo site in South Africa in March of 2019 was that heavy rain could cause water to enter the cable connections at the RF box and/or the spectrometer box, leading to reflections in the cable that create standing waves in our spectrum. To avoid getting water in our cable connections and in the either the RF Box or the Spectrometer Box, we decided to put a large circular plastic tarp over the ground where the RF Box was buried and to wrap the Spectrometer Box in a large plastic bag. Both succeeded in keeping water away from our equipment, allowing us to avoid reflections in the cable as well as water damage to our electronics.

The second picture shows the terrain inside and around the quarry site, before the High-Z system was installed, with the camera pointing in the geographical southwest direction. This picture was taken when we were exploring potential sites for our experiment in the region and reveals the large size of the quarry site, with our white Porsche Macan car used as a size reference in the background of the picture. The length of the car approximately 4.7 meters, viewed in the picture at about a 45 degree angle. Many thanks to Sebastian Gamboa, who lent us this car after mine was totaled on I-79 by a deer hit on the way up to the site. Also, many thanks to my advisor Jeffrey Peterson, who found a way for me to proceed forward on my journey to the site by finding another car for me and for joining me on this deployment after my car accident.

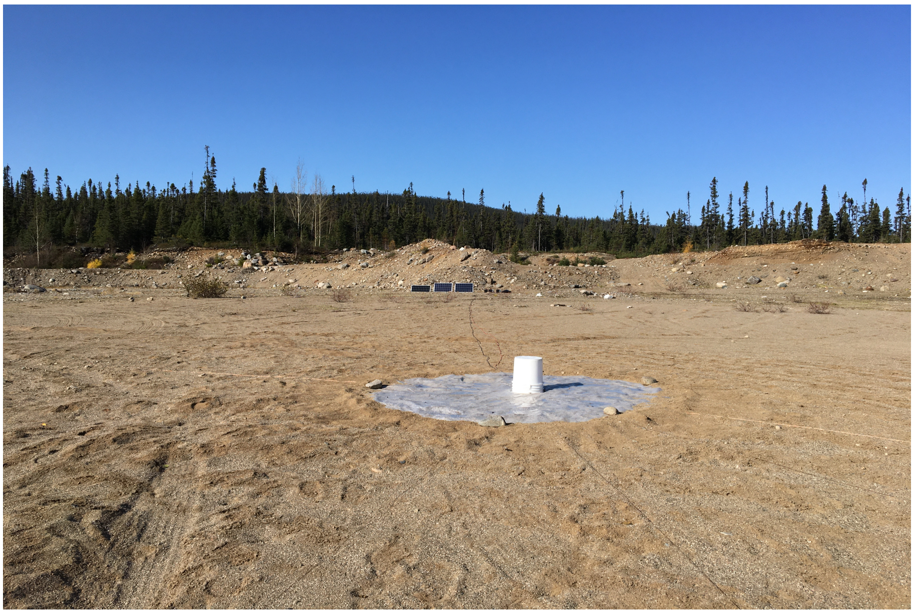

Figure 4.4: High-Z Experiment at Quarry Site in Northern Quebec

Figure 4.5: High-Z Experiment at Quarry Site in Northern Quebec

After helping me to set up at the quarry site, my advisor Jeffrey Peterson left to go back home while I remained to monitor the High-Z system for the remainder of the observation period. One mistake made at this point, which should be avoided in the future, concerns the portable VNA. The portable VNA can be a valuable tool to diagnose problems and should stay with the experiment for every deployment. Professor Peterson took the portable VNA back with him to Pittsburgh, not knowing that further problems could make the portable VNA very valuable for diagnostics. More explanation on this will be provided later in this section.

Monitoring the High-Z system after setting up involves downloading the data every day, checking the spectra on site using the Real Time Viewer, measuring the voltages of the batteries supplying power to the system, measuring the currents from the solar panels to the batteries, and producing a waterfall plot of the downloaded data in the hotel to check for quality of data from the previous day. However, since the quarry site was new and unfamiliar to us, one of the first things I noticed upon monitoring the system was the incorrect orientation of the solar panels relative to the direction of maximum sunlight. On the third day of observation, while visiting the site in the late afternoon, I noticed that the Sun was no longer hitting our solar panels with about 2 hours of daylight still left. Since all three batteries had full charge, I decided to leave all three batteries connected to the equipment for that night.

Upon checking the sun's angle relative to the solar panels around 10:30am on the fourth day of observation, I noticed the solar panels were facing 20° East of South instead of directly South. For northern latitudes during winter, solar panels should be facing directly South to maximize the Sun's total collecting time. Knowing that the incorrect orientation of the solar panels would cause the batteries to charge insufficiently during the day, I disconnected one of the three batteries to take back with me to the hotel for re-charging. I reconnected the solar panel and charger that charged the third battery before to one of the remaining batteries in the field, allowing one of the two remaining batteries to be charged by two solar panels instead of one. While the third battery was re-charging in the hotel, I went back to the quarry site to re-position all the solar panels to face directly South. This process takes a bit of time, as the solar panels must not only be re-positioned to the South but the stakes and the clamps that support the solar panels must be re-adjusted. After re-positioning all the solar panels, I went back to the hotel to retrieve the fully charged third battery and brought it back to the site to connect to our equipment for the night.

Despite not being correctly oriented to the South, the solar panels actually performed well in charging the batteries in the first four days of observation. The voltages measured on all three batteries were consistently above 12V every single day, even on cloudy and partially sunny days (all three batteries started out with full charge at the beginning of the observation). The current delivered from the solar panels to the batteries, however, varied greatly with the amount of sunlight the panels were receiving at any given time. In full sun, the panels would deliver a current in the range $2.5A - 4.8A$, depending on the angle of the sun relative to the panels, with the larger current corresponding to a more direct angle of the sun's rays. In cloudy weather, the panels would deliver only about $1A - 2A$, depending on the amount of cloud cover.

In addition to diagnosing and correcting the problem with the orientation of the solar panels, I downloaded the data for each day of observation and checked the spectrum both on site and in the hotel after creating a waterfall plot from the downloaded data. Two of the waterfall plots from the third day of observation can be found in the "High Z Data Analysis" chapter in section "October 2020." A sample of the on-site spectrum taken of the sky with a 20cm antenna is shown in the picture below, representing one, 11-second integration period of observation. Such spectra are displayed by the Real Time Viewer in the field and allow us to monitor the spectra of all three sources (antenna, noise source, and internal 50Ω) in real time. This Real Time Viewer spectrum of the sky is very smooth and mostly RFI-free. However, as mentioned before, transient RFI lines can appear in the spectrum at different times.

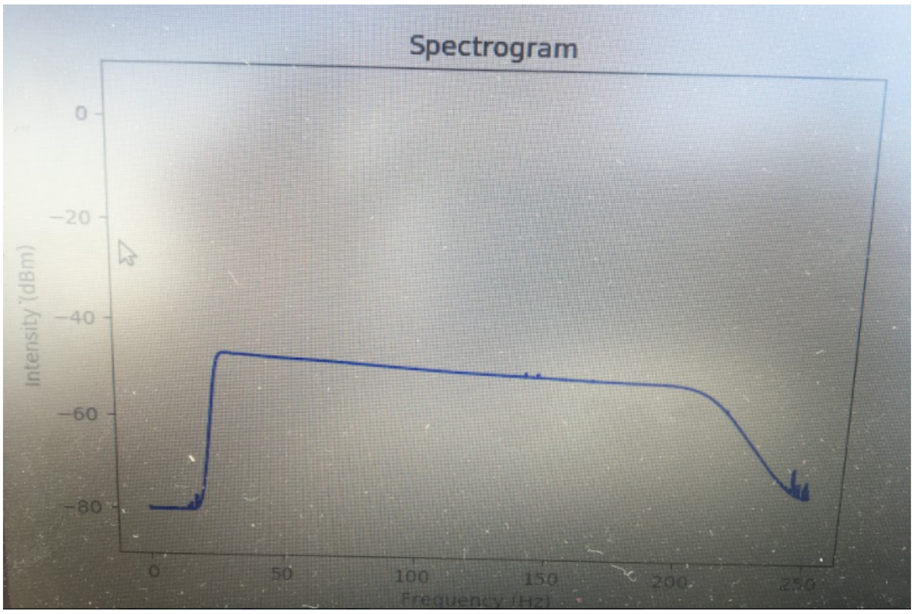

Figure 4.6: Real Time Viewer Spectrum of the Sky with 20cm Antenna at Quarry Site

The Real Time Viewer is an excellent and quick tool for checking if the system is working properly in the field. In fact, it was the Real Time Viewer that alerted me to a major problem with our system on the fifth day of observation at the quarry. After arriving to the site early morning on the fifth day of observation and downloading the data from the previous day, I checked the Real Time Viewer and found the spectra of all three sources (antenna, noise source, and 50Ω) to be very unusual. Below is a picture of the spectrum shown by the Real Time Viewer that morning for the 50Ω internal resistor from the calibration side of the switch. Like the spectrum from the sky in the picture above (Figure X), the spectrum from the 50Ω internal resistor on the calibration side should be nearly flat and very gently sloping downward, with an overall level about 15dB lower than the sky spectrum. However, what we see in the Real Time Viewer instead is a spectrum that contains oscillations. The spectra of all three sources showed similar oscillations in the Real Time Viewer.

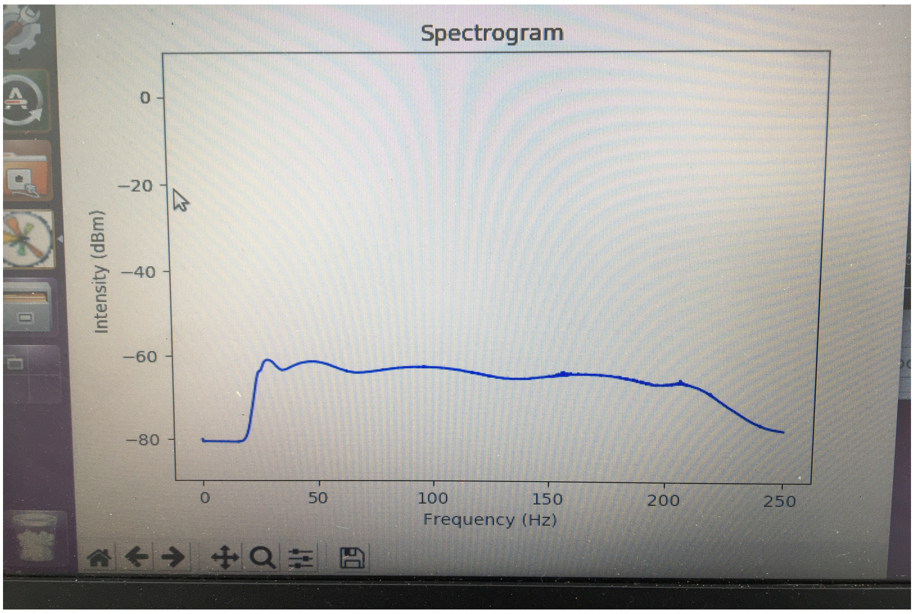

Figure 4.7: Real Time Viewer Shows Oscillations in the Spectra of the Internal 50Ω Calibration Resistor

The High-Z system did not appear to be disturbed or changed in any way from the previous day, so it was impossible to diagnose the problem immediately. In such situations, when there is a problem with the system but the source of the problem is not clear, a portable Vector Network Analyzer can be very useful to help locate the source of the problem. For example, when we encountered the ringing in the spectrum at the start of our observations, we used the VNA to eliminate the Spectrometer Box as the source of the problem by breaking the electronic circuit at the connection between the RF Box and the Spectrometer Box and measuring the spectrum with the VNA. If the VNA had stayed with the experiment instead of brought back to Pittsburgh, I would have used the VNA to measure the spectrum at various points in the system to narrow down the source of the problem. However, lacking the VNA to diagnose the problem on site, I decided to stop the data collection and retrieve both the RF Box and the Spectrometer Box for further testing at the hotel.

At the hotel, I devised a simple strategy to locate the source of the problem. Finding another 50Ω load in our spares kit, I decided to measure the spectrum of this 50Ω load at various points in the electronic chain, using the Real Time Viewer to check the spectrum. Since I needed the Real Time Viewer to show me the spectrum, I could not disconnect the Spectrometer Box and therefore had to start breaking the electronic chain starting upstream. First, I replaced the internal 50Ω resistor and the noise source on the calibration side of the switch with the 50Ω testing load. The spectrum still showed the same oscillations as before. This allowed me to eliminate the internal 50Ω load and the noise source as the cause of the problem. Going downstream to the next link in the electronic chain, I disconnected the mechanical switch from the first filter and connected the 50Ω testing load to the first filter. This time, the Real Time Viewer showed a flat, gently sloping spectrum at the correct level. Therefore, I immediately knew that the problem was located at the mechanical switch.

After taking all the screws out and opening up the mechanical switch, the exact source of the problem became clear. The strip of metal at the base of the switch that swings back and forth between the antenna terminal and the calibration terminal had broken off at the base, severing the electrical connection between the three sources and the rest of the system. The picture below shows how the mechanical switch looked inside after being opened. The oscillations in the spectrum from the Real Time Viewer then made sense - the oscillations resulted from the first filter seeing an output impedance other than 50Ω from the mechanical switch.

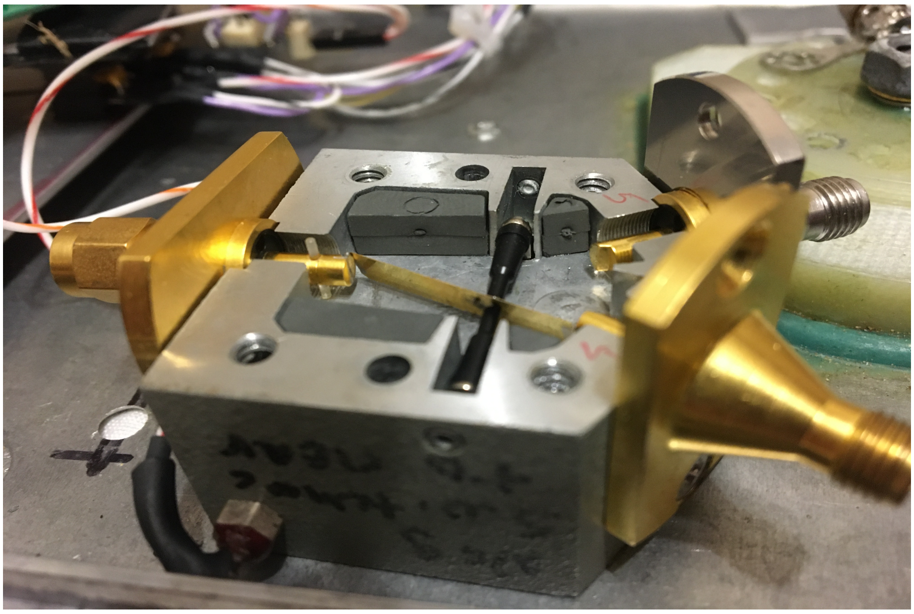

Figure 4.8: Broken Strip at the Base of the Mechanical Switch

Fixing the mechanical switch required soldering the metal strip back to the base of the switch. However, doing so proved to be very challenging because two magnetic pins were pushing on the metal strip from both sides, causing it to bend either toward the antenna terminal or the calibration terminal. Normally, these magnetic pins are controlled by the Raspberry Pi and switch the location of the strip between the antenna terminal and the calibration terminal at the correct time. To prevent these two magnetic pins from pushing the metal strip to either side, I inserted rolled up tissue paper in the spaces behind each pin to keep them from moving back and forth.

After getting the metal strip symmetrically positioned in the middle, I was able to solder the metal strip to the small golden cylinder at the base of the mechanical switch. It took many tries to achieve this because the strip had to be soldered at just the right location and angle. If the metal strip was soldered slightly below normal level, it would scrape the bottom floor of the switch. If the metal strip was soldered slightly above normal level, it would then scrape the top of the switch. If the metal strip was not soldered at the exact angle, it would not make a perfect connection to either the antenna terminal or the calibration terminal. Therefore, soldering the metal strip to the base was a delicate affair. However, after repeated efforts, I was able to succeed in soldering the metal strip at just the right location and correct angle at the base of the switch.

Below is a picture depicting the metal strip after being correctly soldered to the base. In the picture, you can see the two rolled up tissue papers at both ends of the switch used to prevent the pins from pushing the metal strip to either side during soldering. You can also see the exact vertical angle the metal strip had to be soldered at the base to make a proper connection to both terminals at the bottom.

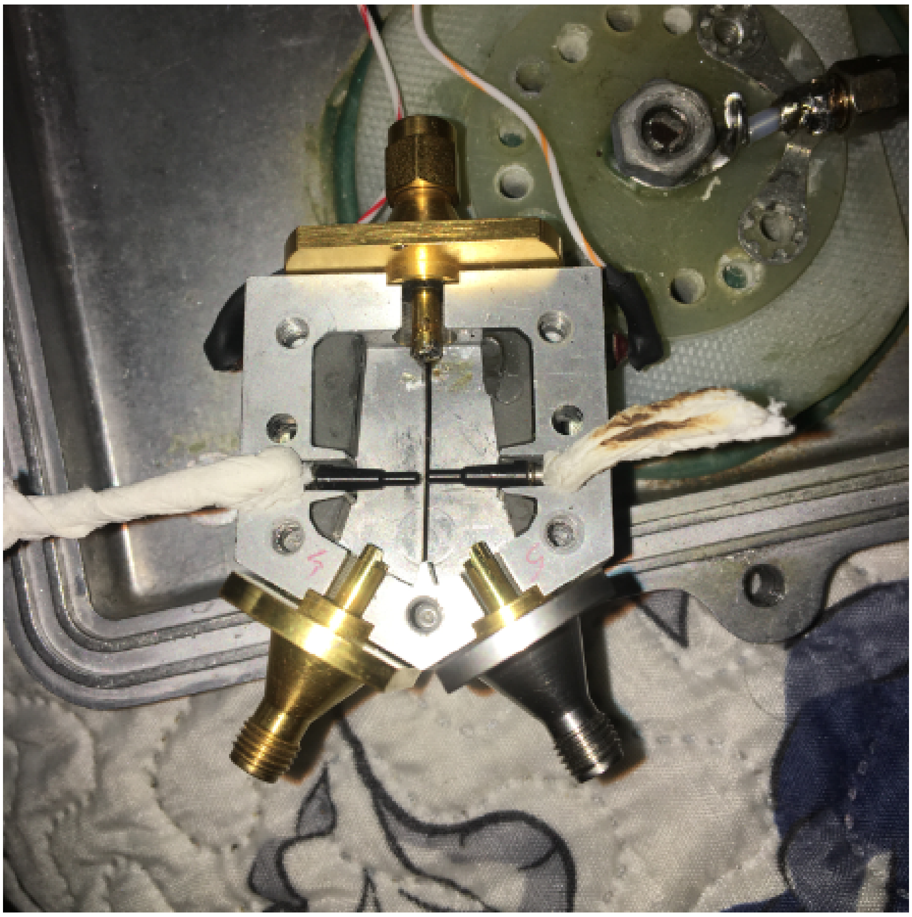

Figure 4.9: Metal Strip Soldered at the Base of the Mechanical Switch

After the metal strip was soldered successfully and the mechanical switch re-connected to the rest of the High-Z System, I tested the whole electronic chain of the system by attaching the 50Ω test load on both sides of the mechanical switch and looking at the spectrum in the Real Time Viewer. Below are two pictures: 1) shows the 50Ω test load providing a Johnson noise signal to the calibration side of the mechanical switch, which was re-connected to the whole system after repairs, and 2) depicts the spectrum on the Real Time Viewer for this test case. From the spectrum on the Real Time Viewer, we can see that the metal strip is making a good connection to the calibration side of the switch and producing the expected spectrum for the 50Ω test load. The connection to the antenna side of the mechanical switch was also tested with the 50Ω test load and showed good connection.

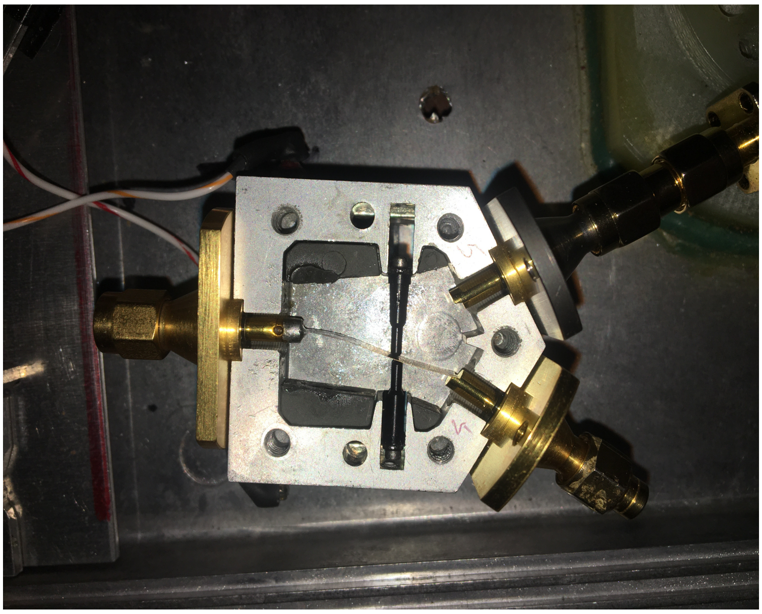

Figure 4.10: Testing the Mechanical Switch After Repairs

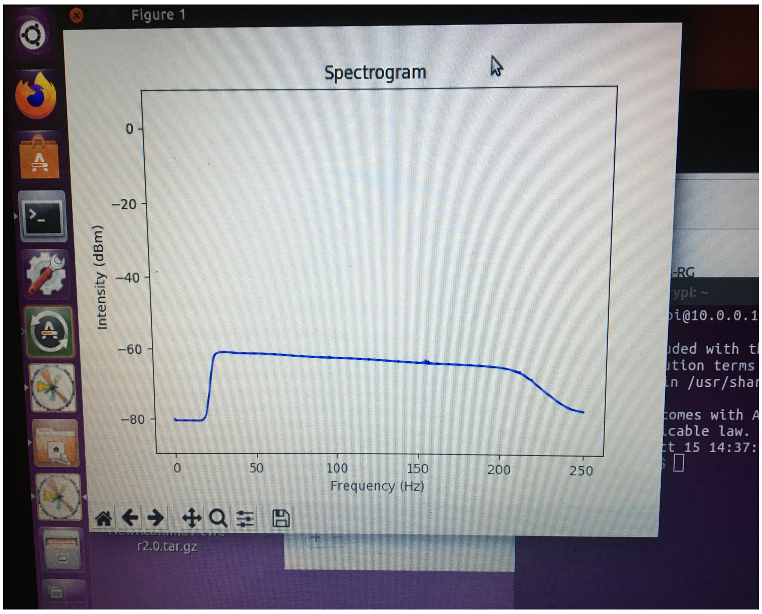

Figure 4.11: Real Time Viewer Showing the Expected Spectrum of a 50Ω Test Load

Spectra with the 50Ω test load indicated the mechanical switch was fully repaired, so I proceeded to re-connect the noise source with the internal 50Ω load to the calibration side of the mechanical switch and the first LNA to the antenna side of the mechanical switch. Then I connected the 50Ω test load to the input of the first LNA to make sure that the whole chain starting at the input terminals of the first LNA was working properly. The spectrum on the Real Time viewer showed good results, with a smooth, gently downward sloping spectrum for the 50Ω test load on the input of the first LNA (the spectrum was about 15dB higher with the 50Ω test load connected to the input of the LNA than directly to the antenna side of the mechanical switch, which was expected due to the gain of the LNA).

As the metal strip in the mechanical switch changed position from the antenna terminal to the calibration side terminal, the internal 50Ω load on the calibration side showed a good spectrum on the Real Time Viewer but the noise source showed a problematic spectrum. The spectrum of the noise source contained oscillations and exhibited a signal level lower than expected.

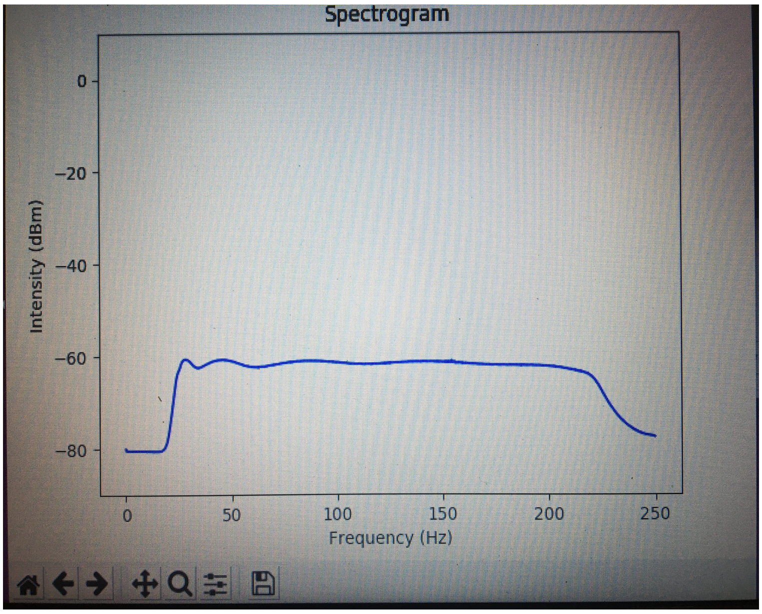

Figure 4.12: Noise Source Spectrum Indicates Noise Source Not Functioning Correctly

After doing further testing, I came to the conclusion that the noise source was damaged beyond repair, possible due to being exposed to electrostatic charge. Since we did not have a spare noise source at the time and shipping a new one would have taken over two weeks, our experimental observations unfortunately ended prematurely.

Chapter 5

High Z Data Analysis

Once the data from the field is obtained, it must go through a data analysis pipeline. This pipeline involves multiple steps, which I will summarize below. The main stages of this pipeline involve preparing the data for analysis, calibrating the data, performing a Singular Value Decomposition, modelling and subtracting the foreground of the galaxy, and finally evaluating the residuals of the final spectrum.

When the data is first collected from the field and plotted in a waterfall plot, it can contain regions of strong radio frequency interference (RFI). These sources of RFI can be astronomical, such as the synchrotron radiation of our Milky Way galaxy, which we will deal with separately at a later stage of our analysis. They can also originate from the atmosphere or come from man-made sources. RFI originating from the atmosphere include meteor scatter or shortwaves that bounces off the atmosphere. Man-made sources of RFI includes FM radio stations, communications between relay stations, TV stations, radio signals from satellites, and air traffic communications.

Before we can analyze the data for the cosmological signal, we must remove significant signatures of RFI from our dataset. We carry this out by excising any signal with a spike in the signal level of 3σ or higher above the average value in a given rectangular array of our data set. Excising three sigma RFI from the data set leads to areas of deleted data within our data set. To fill in the holes in the data, we apply a median filter to replace the deleted data.

After the data is prepared by removing the RFI, we calibrate the observational data using the field calibration described in the section "Field Calibration". The field calibration for version 1 is different from versions 2 and 3. In version 1, the field calibration is performed by the internal calibration sources, which include a 50Ω resistor and a noise source. In version 2 and 3 of the system, the field calibration also involves the temperature recorded by the thermocron sensor inside the RF box, which helps to determine the total noise temperature of the LNA as a function of the ambient temperature. In either case, the appropriate field calibration must be performed for the correct version of the system.

Below I show a waterfall plot of the data from Day 4 at the Karoo Site 4, taken with the medium size antenna (54cm). All RFI has been removed from the dataset and a field calibration using the internal calibration sources has been applied approximately every minute. In the plot, we see the quarter wave resonance of the antenna factor AF. This resonance increases in intensity at two particular time periods shown in the plot. The first increase in intensity of the brightness temperature happens between LST 14:00-19:00. The second increase in brightness temperature happens around 0:00. These increases in the temperature brightness as a function of LST correspond to the Milky Way galaxy passing through the range of our antenna beam pattern throughout the course of the data taken.

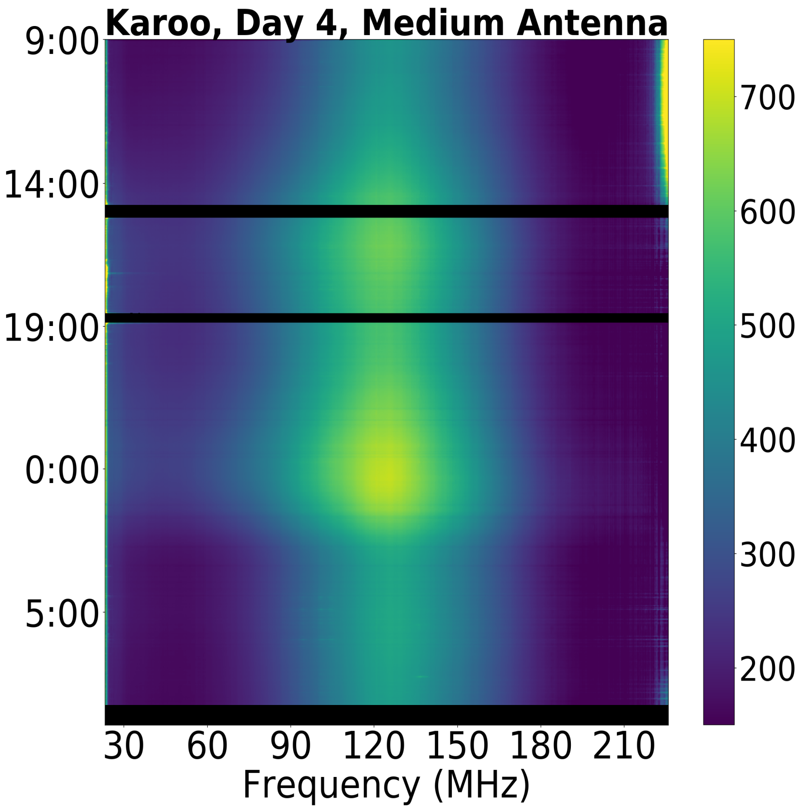

Figure 5.1: Karoo Site 4, Day 4, Medium Antenna

Once the data is properly calibrated for the appropriate version of the system, a Singular Value Decomposition (SVD) must be performed on the data set. The SVD separates the frequency dependence of the brightness temperature from the time dependence in our data set. This is necessary because the brightness temperature varies significantly with the time of day due to our Milky Way galaxy rising above the observational horizon of our telescopes and then setting. The cosmological signal, however, should not vary with time. Therefore, it is very helpful to separate the time variation of the brightness temperature from the frequency variation of the brightness temperature. The equation for the SVD that allows us to do that is the following:

$$M = U\Sigma V^* \tag{5.1}$$

In equation (5.1), the matrix M represents our dataset, U is the matrix that represents the variation of the brightness temperature with time, V^* is the matrix that represents the variation of the brightness temperature with frequency, and Σ represents the eigenvalue of the decomposition (the singular values). Below I show the plots of all three matrices, with U and V^* plotted for the value $\Sigma = 0$.

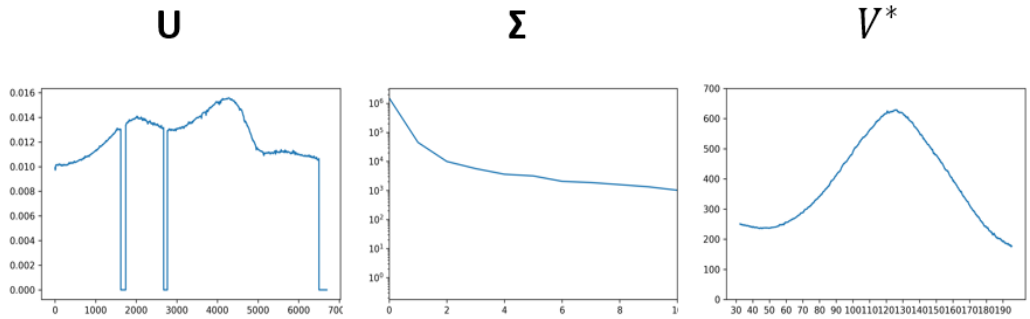

Figure 5.2: Singular Value Decomposition of our Data for Day 4 at Karoo Site 4, July 2018

After decomposing our data set as a function of frequency and time, we analyze the frequency component. The brightness temperature as a function of frequency will include the signal from our Milky Way Galaxy, as well as any resonances of the Antenna Factor AF present in the spectrum. The sky brightness temperature of the Milky Way galaxy decreases with frequency according to a polynomial function that is approximately $f^{-2.5}$. we can fit a polynomial function of similar form to our own data to find the exact sky brightness temperature of the Milky Way galaxy.

Correct modelling of the sky brightness temperature of the Milky Way galaxy is a delicate matter. Several maps of the galactic foreground have been made at particular frequencies, including the Haslam map at 408MHz and the WMAP maps at 23, 33, 41, 61, and 94GHz. Using these maps, a model of the galactic foreground has been created for the frequency range 10MHz-100GHz by Oliveira-Costa [7]. Some groups use this model to understand the foreground contribution from the galaxy and some groups even use it for calibration. However, this model is not used by all groups. Many groups attempt other means of modelling the galactic synchrotron radiation in their measured spectra, using polynomial functions with different number of terms. There is no one accepted and agreed-upon method for modelling the galactic foregrounds for all the groups. However, modelling the galactic foregrounds spectrum is important for any group attempting to measure the 21-cm cosmological signal because the synchrotron emission spectrum of the Galaxy dominates the foreground of the sky temperature signal. In fact, the brightness temperature of the Galaxy is approximately four to five orders of magnitude higher than the expected cosmological signal, and detecting such a small cosmological signal is a significant challenge in such experiments. Therefore, being able to properly and accurately model and subtract the galactic signal from the measured spectrum of the sky is an important and complex task for any experimental group measuring the global 21-cm signal.

In addition to the galactic foregrounds, there are also foreground contributions from the Earth's ionosphere. The amount and the spectral shape of the contribution to the foregrounds from the Earth's ionosphere will depend on the electron temperature and optical depth of the ionosphere. Like the galactic foreground contributions, many groups have different ways of modelling the foreground contributions from the ionosphere and it remains a challenge for all groups to model all astronomical and atmospheric foregrounds correctly.

Once we obtain the model of the sky brightness of the Milky Way galaxy, we factor it out of our dataset, leaving only resonances of the Antenna Factor and the residue spectrum. After factoring out the Antenna Factor, we are left with a residue spectrum that could contain the cosmological signal.

Below I show the residue spectrum I obtained for the data set from July 2018, using the Medium Antenna (54cm). The residue spectrum is included to illustrate the final product of the process of the data analysis pipeline developed for the system. However, for the particular residue spectrum shown here, the sensitivity of the system and the systematic errors have not been fully and rigorously determined from all aspects of the experiment, so we shouldn't interpret the residue spectrum shown with too much weight. In order for our experiment to reach the sensitivity required to confirm or deny the observational results of EDGES, testing of every part of our system must continue to be performed to a very accurate degree, which requires the sustained efforts of many other people in our group.

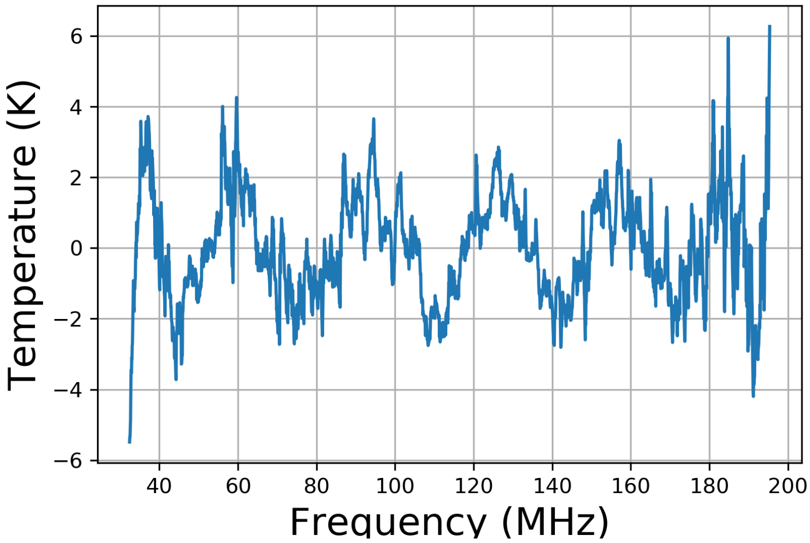

Figure 5.3: Residue Spectrum for Karoo Site 4, Day 4, Medium Antenna

Below is a table summarizing the data collected with the High-Z system for all deployments between 2018 and 2020.

Deployment	**Date**	**Antenna**
July 2018	July 23	84cm (Long)
	July 24	84cm (Long)
	July 25	84cm (Long)
	July 26	54cm (Medium)
	July 27	54cm (Medium)
	July 28	54cm (Medium)
March 2019	March 15	25cm (Short)
	March 16	25cm (Short)
	March 17	25cm (Short)
	March 18	25cm (Short)
	March 19	54cm (Medium)
October 2020	October 9-11	20cm (Extra Short)
	October 12	20cm (Extra Short)
	October 13	20cm (Extra Short)

Table 5.1: Summary of All Data Collected for 2018-2020 Deployments

Chapter 6

Conclusion

The fundamental design of the project High-Z is very unique and unlike any of the designs used by other experimental groups attempting to measure the global 21-cm signal. In the last few years, High-Z has gone through a series of improvements, including three phases of upgrades. Each new version has been better equipped to detect the cosmological signal. The fourth version of the High-Z system was deployed in July 2021 and is currently in the field collecting data. I am very excited about the fourth version of the experiment and believe it has a real possibility of detecting any significant cosmological features present in the 21-cm all-sky spectrum.

The work done in this dissertation has contributed significantly to the development of the fourth version of the experiment. The investigations of the absolute calibration using Johnson loads with co-axial cables have re-affirmed the importance of keeping the electrical path length as short as possible between the antenna output terminals and the first LNA. For an unmatched, high impedance network like High-Z, laboratory tests have revealed that using co-axial cables even beyond 15cm to connect a high impedance source to our high impedance LNA can lead to substantially large cable resonances in our experiment frequency range. We have developed a model for understanding and predicting the spectral contribution of such cable resonances to our system, and this model can be used to assess the contribution of cable resonances to calibration and field measurements in the future.

Our investigations of the noise properties of the LNA in the laboratory have also contributed significantly to the fourth version of the experiment. Using a variety of different techniques we developed and tested in the lab, we discovered that the current noise contribution of the LNA to the noise temperature of the system is quite substantial at lower frequencies for our smaller antennas. For the larger antennas, on the other hand, the current noise contribution grows with quarter-wave resonance. As a result of our extensive testing of the LNA noise properties in the lab, we have determined that an accurate measurement of the current noise of the LNA in the field is absolutely crucial for a proper calibration of our system. To that extent, we have modified the placement of the first LNA in the RF Box from the previous two versions, moving the LNA from the antenna side of the mechanical switch further down to the output of the mechanical switch. Placing the LNA at the output of the mechanical switch allows us to calibrate the LNA in the field more accurately using the noise source and 50Ω load on the calibration side of the mechanical switch.

To measure the current noise contribution of the LNA in the field more accurately than we did in the first version of the system, we have decided to incorporate reactive loads on the calibration side of the mechanical switch. In our lab tests using the noise figure meter, using reactive loads between the noise source and the amplifier allowed us to measure the current noise of the amplifier in a very simple and effective manner. The success of this technique has led us to consider using a similar strategy in the field. By choosing a reactive load with a capacitance similar to the antenna and placing it after the noise source on the calibration side of the mechanical switch, so that the reactive load is between the noise source and the LNA, we can perform a similar process for measuring the noise current contribution of the LNA in the field during deployments as we did in the lab using the noise figure meter.

While investigations with cable resonances through laboratory tests and models have strengthened our priority to keep the electrical path length between the antenna and the LNA to a minimum, our investigations of the noise properties of the LNA have motivated us to reconsider the placement of the LNA upstream of the mechanical switch. If the LNA is located upstream of the mechanical switch on the antenna side, the signal from the calibration sources on the other side of the switch does not pass through the LNA. This really limits how accurately and precisely the field calibration can track the changes in the noise performance of the LNA during deployments. However, moving the LNA further down to the output of the mechanical switch in order to take advantage of the field calibration sources can create an electrical path length long enough to lead to substantial cable resonances. Therefore, to solve both problems at once, we have decided to move the LNA to the output of the mechanical switch but shorten the electrical path length between the antenna and the mechanical switch as much as possible.

To create the shortest possible connection between the antenna and the switch, we fitted the antenna output terminal directly inside the mechanical switch on the antenna side. The metal strip inside the mechanical switch, which switches back and forth between the calibration and the antenna sides, now connects directly to the antenna output terminal when on the antenna side. The physical separation between the antenna output terminal and the LNA is now only the length of the metal strip inside the mechanical switch and an SMA connector at the output, no more than 6cm in total length. The electrical path length is therefore short enough to avoid significant cable resonances in our frequency band. Of course, there will be small level changes in the spectrum as a result of the non-zero electrical path length, but these will be smoothly varying and can be studied and assessed by the the Multiple Reflections Radiative Transfer (MRRT) model developed in this dissertation.

The next steps for the project in terms of calibration should include an updated calibration for the fourth version of the experiment, an analysis of the current noise of the LNA in the field, development of more sensitive methods for measuring the correlations between the current noise and voltage noise of the LNA, and testing of other LNAs to find candidates with quieter current noise. The technique for measuring the current noise and voltage noise of amplifiers using the Noise Figure Meter, which was developed in this dissertation, can be used to easily and effectively test new amplifiers to determine which would be better candidates for our experiment in the future.

Bibliography

[1] A. Auriol, S. Davidson, and G. Raffelt. Axion absorption and the spin temperature of primordial hydrogen. *arXiv: High Energy Physics - Phenomenology*, 2018.

[2] R. Barkana. Possible interaction between baryons and dark-matter particles revealed by the first stars. *Nature*, 555:71–74, 2018.

[3] P. Biermann, B. Nath, L. Caramete, B. Harms, T. Stanev, and J. Tjus. Cosmic backgrounds due to the formation of the first generation of supermassive black holes. *Monthly Notices of the Royal Astronomical Society*, 441:1147–1156, 2014.

[4] J. Bowman, A. Rogers, R. Monsalve, Thomas J. Mozdzen, and N. Mahesh. An absorption profile centred at 78 megahertz in the sky-averaged spectrum. *Nature*, 555:67–70, 2018.

[5] Judd D Bowman, Alan EE Rogers, and Jacqueline N Hewitt. Toward empirical constraints on the global redshifted 21 cm brightness temperature during the epoch of reionization. *The Astrophysical Journal*, 676(1):1, 2008.

[6] J. Cline and A. Vincent. Cosmological origin of anomalous radio background. *Journal of Cosmology and Astroparticle Physics*, 2013:011–011, 2013.

[7] Anglica de Oliveira-Costa, Max Tegmark, B. M. Gaensler, Justin Jonas, T. L. Landecker, and Patricia Reich. A model of diffuse galactic radio emission from 10 mhz to 100 ghz. *Monthly Notices of the Royal Astronomical Society*, 388(1):247–260, Jul 2008.

[8] George B. Field. Excitation of the Hydrogen 21-CM Line. *Proceedings of the IRE*, 46:240–250, January 1958.

[9] Steven R Furlanetto, S Peng Oh, and Frank H Briggs. Cosmology at low frequencies: The 21 cm transition and the high-redshift universe. *Physics reports*, 433(4-6):181–301, 2006.

[10] Lincoln J. Greenhill and LEDA Collaboration. Constraining the Thermal State of the IGM at z~20. In *American Astronomical Society Meeting Abstracts #225*,

volume 225 of *American Astronomical Society Meeting Abstracts*, page 403.07, January 2015.

[11] Eugene. Hecht. *Optics*. Addison-Wesley, Reading, Mass, 4th ed. edition, 2002.

[12] Richard Hills, Girish Kulkarni, P Daniel Meerburg, and Ewald Puchwein. Concerns about modelling of the edges data. *Nature*, 564(7736):E32–E34, 2018.

[13] E. Kovetz, V. Poulin, V. Gluscevic, K. Boddy, R. Barkana, and M. Kamionkowski. Tighter limits on dark matter explanations of the anomalous edges 21 cm signal. *Physical Review D*, 98:103529, 2018.

[14] Chun long Li, Xin Ren, M. Khurshudyan, and Yi-Fu Cai. Implications of the possible 21-cm line excess at cosmic dawn on dynamics of interacting dark energy. *Physics Letters B*, 801:135141, 2020.

[15] R. Monsalve, B. Greig, J. Bowman, A. Mesinger, A. Rogers, Thomas J. Mozdzen, N. Kern, and N. Mahesh. Results from edges high-band: Ii. constraints on parameters of early galaxies. *arXiv: Cosmology and Nongalactic Astrophysics*, 2018.

[16] Julian B. Muñoz, C. Dvorkin, and A. Loeb. 21-cm fluctuations from charged dark matter. *Physical review letters*, 121 12:121301, 2018.

[17] M. H. Namjoo, T. Slatyer, and Chih-Liang Wu. Enhanced n-body annihilation of dark matter and its indirect signatures. *Journal of High Energy Physics*, 2019:1–66, 2018.

[18] Jaehong Park, A. Mesinger, B. Greig, Nicolas Gillet Scuola Normale Superiore, A. C. O. E. F. A. A. S. Physics, and The University of Melbourne. Inferring the astrophysics of reionization and cosmic dawn from galaxy luminosity functions and the 21-cm signal. *Monthly Notices of the Royal Astronomical Society*, 484:933–949, 2018.

[19] Nipanjana Patra, R. Subrahmanyan, A. Raghunathan, and N. Udaya Shankar. Saras: a precision system for measurement of the cosmic radio background and signatures from the epoch of reionization. *Experimental Astronomy*, 36:319–370, 2013.

[20] L. Philip, Z. Abdurashidova, H. Chiang, N. Ghazi, A. Gumba, H. M. Heilgendorff, J. Hickish, J. M. J'auregui-Garc'ia, K. Malepe, C. Nunhokee, J. Peterson, J. Sievers, V. Simes, and R. Spann. Probing radio intensity at high-z from marion: 2017 instrument. 2018.

[21] David M. Pozar. *Microwave engineering*. J. Wiley, Hoboken, NJ, 3rd ed. edition, 2005.

[22] Jonathan R Pritchard and Abraham Loeb. 21 cm cosmology in the 21st century. *Reports on Progress in Physics*, 75(8):086901, Jul 2012.

[23] H. Rothe and W. Dahlke. Theory of noisy fourpoles. *Proceedings of the IRE*, 44(6):811–818, 1956.

[24] George B Rybicki and Alan P Lightman. *Radiative Processes in Astrophysics*. Wiley, New York, NY, 2004.

[25] Saurabh Singh, R. Subrahmanyan, N. Shankar, M. Rao, A. Fialkov, Aviad Cohen, R. Barkana, B. Girish, A. Raghunathan, R. Somashekar, and K. Srivani. First results on the epoch of reionization from first light with saras 2. *arXiv: Cosmology and Nongalactic Astrophysics*, 2017.

[26] Texas Instruments. *LMH6629 Ultra-Low Noise, High-Speed Operational Amplifier with Shutdown*, SNOSB18I, 2014. [Online].

[27] T. Voytek, A. Natarajan, J. Jáuregui-García, J. Peterson, and O. López-Cruz. Probing the dark ages at z   20: The sci-hi 21 cm all-sky spectrum experiment. *The Astrophysical Journal*, 782, 2014.

[28] Linfeng Xiao, R. An, Le Zhang, B. Yue, Yidong Xu, and B. Wang. Can conformal and disformal couplings between dark sectors explain the edges 21-cm anomaly? *Physical Review D*, 99:023528, 2019.

[29] S. Yoshiura, Keitaro Takahashi, and Tomo Takahashi. Impact of edges 21-cm global signal on the primordial power spectrum. *Physical Review D*, 98:063529, 2018.